The Pennsylvania State University

The Graduate School

College of Earth and Mineral Sciences

# INDOCYANINE GREEN-ENCAPSULATING CALCIUM PHOSPHOSILICATE NANOPARTICLES: BIFUNCTIONAL THERANOSTIC VECTORS FOR NEAR INFRARED DIAGNOSTIC IMAGING AND PHOTODYNAMIC THERAPY

A Dissertation in

Materials Science and Engineering

by

Erhan İ. Altınoğlu

© 2010 Erhan İ. Altınoğlu

Submitted in Partial Fulfillment
of the Requirements
for the Degree of

Doctor of Philosophy

August 2010

The dissertation of Erhan İ. Altınoğlu was reviewed and approved* by the following:

James H. Adair
Professor of Materials Science and Engineering
Dissertation Advisor
Chair of Committee

Mark Kester
G. Thomas Passananti Professor of Pharmacology
Professor of Cellular and Molecular Physiology

Carlo G. Pantano
Distinguished Professor of Materials Science and Engineering
Director of the Materials Research Institute

Gary L. Messing
Distinguished Professor of Ceramic Science and Engineering
Head of the Department of Materials Science and Engineering

*Signatures are on file in the Graduate School

# ABSTRACT

The American Cancer Society projected 1.5 million new cancer cases to be diagnosed in 2009. Of these diagnoses, a mere 20% were expected to be detected in their early, localized stage. With such advantageous early detection comes various low risk and highly effective treatment options, resulting in 5-year relative survival rates of over 90%. Unfortunately, the remaining diagnoses were expected in a later stage of the progressive disease, where treatment requires infusions of toxic pharmaceuticals and blasts of brutal radiation, and the prognosis is as miserable as the experience itself. Thus, the advantages associated with timely detection and treatment has generated interest in a simultaneous approach to early diagnosis and therapy, a combined modality termed theranostics.

Recently, the concept of multifunctional nanocarriers that can concurrently perform these distinct tasks has emerged and is attracting increased attention. The full potential of a theranostic strategy lies in the ability to engineer such a bifunctional vector with both of the optical and therapeutic properties necessary to complete the separate functions. Specifically, much interest has been initiated on fluorescent photosensitive agents that respond in the near infrared (NIR) by concurrently emitting intense and sustained fluorescence signals for deep tissue imaging, as well as generating a photodynamic response to trigger localized cell death for minimally invasive, molecular-scale therapy.

The synthesis, laundering, and properties of calcium phosphosilicate nanoparticles (CPSNPs) that encapsulate the NIR fluorophore indocyanine green (ICG) related to multifunctional fluorescent photosensitization is presented. Imaging with transmission electron microscopy (TEM) revealed the well dispersed state of the nanoparticles, the spherical morphology, and the log normal mean particle diameter of 16 nm. Electron energy loss spectroscopy (EELS) mapping identified a Ca:P:Si ratio of 1:1.72:0.41 and a homogeneous

composition without evidence of an element rich or deficient architecture. Zeta potential of the as-synthesized, citrate-functionalized CPSNPs was -29 ±3 mV. A theoretical solids loading of 1.9 x $10^{13}$ CPSNP/mL was calculated for a standard suspension. The mean ICG content per suspension is 2 x $10^{-6}$ M, which equates to approximately 63 fluorophore molecules encapsulated per CPSNP.

For imaging and diagnostic considerations, the doped CPSNPs exhibited significantly greater intensity at the maximum emission wavelength relative to the free constituent fluorophore. The quantum efficiency of the fluorescent agent is 200% greater at 0.053±0.003 over the free fluorophore in PBS. Also, photostability based on fluorescence half-life of encapsulated ICG in PBS is 500% longer under typical clinical imaging conditions relative to the free dye. These performance enhancements are attributed to the matrix shielding effect of the NP around the internalized fluorophore molecules.

The *in vivo* emission signal stability from ICG-CPSNPs was compared to the free fluorophore by whole animal NIR imaging. The duration of fluorescent signal from the ICG-CPSPNPs was extended to up to four days post-injection, highlighting the potential for long-term imaging and sensitive tracking applications using ICG when encapsulated within the protective matrix of CPSNPs. The surfaces of the ICG-CPSNPs were covalently bound with polyethylene glycol (PEG). The pharmacokinetic behavior of the PEGylated ICG-CPSNPs revealed that ICG-CPSNP-PEG passively localize within solid tumor xenografts within 24 hours of systemic administration via the enhanced permeation and retention (EPR) effect.

To impart tissue specificity, the ICG-CPSNP-PEGs were bioconjugated with gastrin-10 with the intention of targeting BxPC-3 pancreatic cancer cells by specifically binding the over expressed receptors for this hormone. *In vitro* assessment acknowledged the faculty of this functionalization to preferentially target the cells of interest; fluorescence microscopy visually revealed this targeting capacity, while flow cell cytometry explicitly characterized the preferential

cellular uptake of the ICG-CPSNP-PEG-Gastrin-10 by BxPC-3 cancer cells. An NIR whole animal imaging study further verified that gastrin functionalization provides a direct means for targeting orthotopic pancreatic tumors *in vivo*, with emission signal intensities from excised tumors measuring higher relative to the controls. This result highlights the ability of targeted ICG-CPSNPs to provide the high *in vivo* selectivity needed for the most effective diagnostics imaging.

Likewise, the therapeutic capacity of the ICG-CPSNP nanocomposites is greater when comparing the *ex situ* generation of singlet oxygen ($^1O_2$) to that from the unencapsulated sensitizer. The photoactivation of singlet oxygen in a hypoxic aqueous environment was found to be 60% higher from the ICG molecules upon encapsulation within the CPSNP matrix.

Initial *in vitro* toxicity trials were conducted in four distinct cell lines to identify an ICG-CPSNP-PEG dosing limit. It was revealed that acute toxicity is subject to the particle number concentration ($LD_{50}$ of 2 x$10^8$ CPSNP/cell) and not the dose of encapsulated ICG. Next, cell viability was examined as a function of photodynamic therapy (PDT) dose. An unmistakable drop in cell viability *in vitro* relative to the control was observed for all cell lines. The significance of these results rests in the drastically low applied fluence (1 J/cm$^2$), which suggests a plausibly greater efficacy in cell lethality at significantly higher, more customary laser powers.

This enhancement in photodynamic response was supplemented by the exceptional *in vivo* PDT effect on tumor growth. ICG-CPSNP-PEGs arrested human breast adenocarcinoma tumor growth over 36 days after only a single, low dose systemic administration (44 nM) and laser activation (12.5 J/cm$^2$). Such heightened photodynamic cell lethality with ICG-CPSNPs emphasizes the tremendous potential this composite nanovector has for low dose PDT applications, particularly considering the non-optimized nature of the preliminary experimentation.

Coupled with the demonstrated improvements in bioimaging performance, the efficient *in vivo* therapeutic execution of ICG-CPSNPs serves as a convincing validation of the apposite bifunctionality of these vectors. Together with the established biocompatibility and favorable pharmacokinetics of calcium phosphates, these composite nanoparticles possess the potential to serve as a model theranostic agent in the early stage diagnosis and treatment of disease.

# TABLE OF CONTENTS

List of Figures……. .....x

Acknowledgements…….....xvii

Chapter 1 Introduction .....1

1.1 Early-Stage Near Infrared Imaging .....2
1.2 Indocyanine Green .....4
1.3 Nanoparticle (NP)-Based NIR Imaging Agents .....6
1.3.1 Criteria for Exogenous Particulates for Imaging Applications .....7
1.3.2 Semiconductor Nanocrystals .....8
1.3.3 Resonant Nanoshells .....12
1.3.4 Dye-Encapsulating Nanoparticle Platforms .....16
1.3.5 Calcium Phosphate-Based Nanoparticulates .....19
1.4 Photodynamic Therapy .....20
1.5 Theranostics: Personalized Point of Care Medicine .....21
1.6 Chapter Summaries .....22
1.7 References .....24

Chapter 2 Synthesis and Laundering of Calcium Phosphosilicate Nanoparticles (CPSNPs) for Encapsulation of Indocyanine Green .....33

2.1 Calcium Phosphate Precipitation .....33
2.1.1 Microemulsion Templating .....34
2.2 Solubility and Controlled Dissolution of Calcium Phosphates .....37
2.3 Materials and Methods .....38
2.3.1 Materials .....38
2.3.2 Synthesis of Dye-Encapsulating Calcium Phosphosilicate Nanoparticles (CPSNPs) .....39
2.3.3 Laundering of CPSNP Suspensions .....41
2.3.4 Characterization of CPSNPs .....43
2.4 Results and Discussion .....45
2.4.1 Synthesis and Washing of NIR dye-doped CPSNPs .....45
2.4.2 Colloidal Characterization .....48
2.4.3 Particle Number Calculation .....52
2.4.4 Fluorophore Encapsulation Yield .....54
2.5 Summary .....54
2.6 Acknowledgements .....55
2.7 References .....56

Chapter 3 Optical Properties of Indocyanine Green-Encapsulating CPSNPs .....59

3.1 Photo-Excitation and Relaxation of a Fluorophore .....59
3.2 Fluorescence .....61
3.3 Non-Radiative Relaxations that Affect ICG .....64
3.3.1 Non-specific Static and Dynamic Quenching .....64
3.3.2 Internal Conversion and Photoisomerization .....65

3.3.3 Photodegradation....67
3.4 Enhancing ICG Optical Performance....68
3.5 Materials and Methods....69
3.5.1. Materials....69
3.5.2 Optical Measurements....70
3.5.3 Fluorescent Lifetime Measurements....71
3.5.4 Quantum Efficiency Determination....71
3.6 Results and Discussion....74
3.6.1 Emission Enhancement....74
3.6.2 Solvent Protection....76
3.6.3 Photostability....78
3.6.4 Quantum Efficiency....80
3.7 Summary....82
3.8 Acknowledgments....84
3.9 References....84

Chapter 4 Functionalization of ICG-CPSNPs for Passive Localization and Direct Targeting of Disease for Diagnostic *In Vivo* Imaging....88

4.1 Functionalization of ICG-CPSNPs to Improve *In Vivo* Pharmacokinetics....88
4.1.1 Physiological Limitations of ICG....89
4.1.2 Improving Circulation Lifetimes via Surface PEGylation for Passive Localization....90
4.1.3 Direct Targeting Approach....91
4.2 Materials and Methods....92
4.2.1 Materials....92
4.2.3 Attachment of PEGamine to carboxylic acid functionalized CPSNPs....93
4.2.4 Gastrin-10 Bioconjugation of CPSNPs....94
4.2.5 Cell Culture Work....94
4.2.6 Fluorescence Microscopy....94
4.2.7 Flow Cytometry....95
4.2.8 *In Vivo* Animal Studies....95
4.2.9. *In Vivo* Whole Animal Imaging....96
4.3 Results and Discussion....97
4.3.1 Verification of Surface Passivation with PEG....97
4.3.2 *In Vivo* Pharmacokinetic Distribution and Tumor Localization in Nude Mice....98
4.3.3 Evaluation of BxPC-3 Pancreatic Cell Targeting by Gastrin Receptor-Targeted CPSNPs....102
4.3.4 Evaluation of Pancreatic Cancer-Targeted CPSNPs *In Vivo*....103
4.4 Summary....105
4.5 Acknowledgements....107
4.6 References....107

Chapter 5 Singlet Oxygen Generation from ICG Encapsulating CPSNPs: Evaluating the Prospect of Photosensitization for Photodynamic Therapy....110

5.1 The Photodynamic Process....110
5.1.1 Singlet Oxygen....114

5.1.2 Components of PDT....117
5.1.3 Photosensitizers....119
5.1.4 Current Limitation of ICG as an Effective Photosensitizer....121
5.2 Materials and Methods....122
5.2.1 Materials....122
5.2.2 SOSG Signal Optimization and Lifetime....122
5.2.3 SOSG Intensity as a function of Photosensitizer Concentration....124
5.2.4 ICG-CPSNP - Induced SOSG Intensity as function of Irradiation Fluence....125
5.3 Results and Discussion....126
5.3.1 Singlet Oxygen Sensor Green (SOSG) Singlet Oxygen Detection....126
5.3.2 Encapsulation Effect on ICG $^1O_2$ Generation....127
5.3.3. Therapeutic Capacity of ICG-CPSNPs Photosensitizers....128
5.4 Summary....131
5.5 Acknowledgements....132
5.6 References....132

Chapter 6 Photodynamic Therapy Using ICG-CPSNPs as the Photosensitizing Agent....136

6.1 Control of the Cell Death Pathway and Ultimate Physiological Response to PDT....136
6.2 Low Dose PDT for Indirect Immuno-Initiation of Cell Death....137
6.3 Materials and Methods....138
6.3.1 Materials....138
6.3.2 Cell Culture Work....139
6.3.3 Cell Viability Assay....139
6.3.4 *In Vivo* Animal Studies....140
6.4 Results and Discussion....141
6.4.1 ICG-CPSNP Dark Toxicity....141
6.4.2 *In Vitro* PDT Performance of ICG-CPSNPs....143
6.4.3 *In Vivo* PDT Improvements from ICG-CPSNPs....146
6.5 Summary....148
6.6 Acknowledgements....149
6.7 References....149

Chapter 7 Summary and Suggestions for Future Work....151

7.1 Summary of Work....151
7.1.1 Colloidal Properties....152
7.1.2 Optical Properties....152
7.1.3 *In vivo* Imaging Performance....153
7.1.4 Therapeutic Capacity....155
7.2 Suggested Future Work....156
7.2.1 Colloidal Properties....157
7.2.2 *In vivo* Therapeutic Performance....159
7.2.3 Scale Up....160

# LIST OF FIGURES

**Figure 1-1.** An illustrative example of the Overall Stage Grouping of cancer in presented for prostate carcinoma. General classifications define stage I cancers are localized to within the tissue of origin, while state II is considered locally advanced, and stage III has spread to proximal tissues. Stage IV cancers are categorized as having metastasized and spread to other organs of the body. The percentage of each stage at time of clinical presentation is plotted (blue bars) in relation to the projected 5-year survival rate associated with each stage (black points).[4] It is clear that the later the stage of the disease at diagnosis, the significantly poorer the prognosis. The staging illustration has been modified from Ref. 10.....2

**Figure 1-2.** NIR absorption spectrum of water and main tissue absorbing components, oxy- and deoxyhemoglobin. The highest optical transmission, the "imaging window", between 800 and 1000 nm, is highlighted.[21].....4

**Figure 1-3.** The structure of the carbocyanine dye indocyanine green (ICG) is illustrated. This NIR active fluorophore exhibits absorption and emission maxima around 785 and 820 nm, respectively.....5

**Figure 1-4.** Illustration of band gap structures for Type-I and Type-II semiconductor heterostructures. Type-II structures have a staggered bang gap as a result of the valence and conduction bands of the material used in the core being lower (or higher) than those in the shell. This results in a spatial separations of carriers, as one carrier is mostly confined to the core, while the other is mostly confined to the shell. This in turn allows emission at energies that are smaller than the band gap of either material, which permit access to higher wavelengths in the NIR.[65].....10

**Figure 1-5.**Optical tunability demonstrated for nanoshells with a 60 nm silica core radius and gold shells 5, 7, 10, and 20 nm thick. The plasmon resonance (extinction) of the particles red shifts with decreasing thickness of the gold shell (or an increasing core:shell ratio). Nanoshells are easily fabricated with resonance in the NIR.[14] .....13

**Figure 1-6.**Ratios of gold concentrations by neutron activation analysis (NAA) in each organ to that in tumor (solid black line) at 24 hours post-systemic administration of PEGylated gold nanoshells. Data reveals unfavorable accumulation of nanoshells in untargeted organs.[97].....15

**Figure 2-1.**The partial phase diagram established for the system of cyclohexane-(NP-5 + NP-9)-aqueous solution of 1.0 M $CaCl_2$ at room temperature. The microemulsion region is marked as shaded area. The composition at point A is a microemulsion and that at point B is an emulsion. Taken from Ref. [148].....35

**Figure 2-2.**The solubility phase diagram for the ternary system, Ca(OH)2-H3PO4-H2O at 37$^{o}$C. The concentrations of calcium as a function of pH in saturated salt solutions. HAP= Hydroxyapatite [Ca5(PO4)3OH], OCP=Octacalcium phosphate [Ca8H2(PO4)6•5H2O], TCP=Tricalcium phosphate [Ca3(PO4)2], DCPD=dicalcium phosphate dihydrate (Brushite) [CaHPO4•2H2O]. ACP = amorphous calcium phosphate [variable]. Redrawn from Ref. [131]. .....38

**Figure 2-3.** Illustration of the stages of the CPSNP synthesis and ICG encapsulation. Particles are templated within reverse micelles, within which precipitation occurs upon micellar exchange of the calcium and phosphate constituents during dynamic fusion and fragmentation. A fraction of ICG molecules are indirectly sequestered within each forming particle during precipitation. Individual CPSNPs are functionalized while still encased in their respective template, providing the necessary electrosteric surface charging to remain dispersed in suspension upon micellar disruption. .....40

**Figure 2-4.**Synthesis flow chart for the precipitation of calcium phosphosilicate nanoparticles (CPSNPs). The synthesis uses a template formed by the self-assembly of the reverse microemulsion in a water-in-oil cyclohexane/ polyoxyethylene(5) nonylphenyl ether/water ternary system. .....42

**Figure 2-5.** Illustration of the van der Waals-HPLC laundering method. The sample suspension is loaded onto a packed column of 20 μm diameter silica microspheres in the as-synthesized, low dielectric solution of 25 v/o cyclohexane in ethyl alcohol. The column is then washed with an ethanol mobile phase that flushes synthesis precursors and unencapsulated dye out, while the CPSNPs are reversibly bound to the stationary phase. The CPSNPs are finally swept off the column by introducing a 30 v/o water in ethanol eluent that promotes electrostatic charging, causing a repulsion between the nanoparticles and the $SiO_2$ media. .....43

**Figure 2-6.** Chromatograms collected from the in-line UV-Vis detector during sample laundering are presented for both the characteristic absorption wavelength of the fluorophore (785 nm - red), and a non-absorbing, short wavelength for particle scattering (400 nm - blue). The top chromatogram presents the raw spectra (solid lines) and the background of particle-free solutions (dotted lines). The bottom spectra are adjusted by subtracting the background such that the optical response is directly attributed to the CPSNPs. The yellow bands in each chromatogram indicate the point of collection. .....47

**Figure 2-7.** A TEM micrograph of a dye-encapsulating ICG-CPSNP dispersion with a magnified inset showing the particles in detail. The imaged CPSNPs are clearly spherical in morphology, aconsequence of templating with reverse micelles. The particles are also well dispersed, as individual particles are visibly isolated with no signs of aggregate structures present across the carbon film of the sample grid. .....48

**Figure 2-8.**The log normal mean and standard deviation of the particle number distribution is 16 nm (n = 932) with a $\sigma_z$ equal to 0.23, respectively. The log normal standard deviation of 0.23 gives a value of 9 nm for -1 standard deviation and 27 nm for +1 standard deviation from the mean value. A second peak centered at 63 nm comprising 1 percent by area with a log normal standard deviation equal to 0.01 is also evident, and is attributed to the coalescence of multiple micelles at the moment of disruption. .....49

**Figure 2-9.** EELS map of elements Ca, P, and Si across a single particle. The pseudocoloring reveals a homogenous distribution of elements throughout the

particle volume with no discernible morphological characteristics, such as a Si rich shell or organic rich core (C map not shown). ..... 51

**Figure 2-10.** EDS spectra collected on a dried suspension of CPSNPs. The probe size relative to primary particle diameters renders this technique a bulk analysis. The quantification of the bulk particles (32% Ca, 55% P, 13% Si) matches nicely with the elemental analysis collected for an individual particle by EELS. The presence of a Na peak in the spectra is attributed to free ions in solution that crystallize upon drying and are present in the analyte area. ..... 51

**Figure 2-11.** Zeta potential distributions of CPSNP suspensions in 7:3 EtOH:$H_2O$ (pH 7). The zeta potential of an as-synthesized suspension of citrate-functionalized CPSNPs is -29 ± 3 mV, consistent with the carboxylate ($COO^-$)-termination. The surface passivation with polyethylene glycol (PEG) shifts the distribution of charge to a net zero charge (3 ± 2 mV). ..... 52

**Figure 3-1.** A simplified Jablonski diagram illustrating the photoexcitation process (absorption [$10^{-15}$ s] to the singlet first and second excited energy states, $S_1$ and $S_2$ respectively, and the various energy deactivation channels (internal conversion [$10^{-12}$ s], fluorescence [$10^{-8}$ s], and non-radiative decay (variable)) that return the molecule to its original ground state ($S_0$). The intersystem crossing process to the excited triplet state ($T_1$), and its associated radiative relaxation channel (phosphorescence [$10^{-2}$ s]), are also illustrated and will be discussed further in Chapter 5. ..... 61

**Figure 3-2.**The molecular orbital (MO) diagram of an ethene molecule ($C_2H_4$) is used to illustrate the spin-opposite paring of the electron elevated to an excited state upon photoexcitation with its associate electron in the highest occupied orbital of the ground state. The return to the ground state is spin allowed and therefore may occur through a variety of relaxation pathways. ..... 62

**Figure 3-3.**The *cis*/*trans* isomerization of indocyanine green is illustrated. The planar *cis* conformation structurally converts to the *trans*-configured isomer, for which the substituent groups orient in opposite directions, via a rotation about a double bond (C=C) of the polymethine chain. ..... 66

**Figure 3-4.**The [2+2]-cycloaddition photodegradation process in ICG is illustrated. (A) Reactive species such as $O_2$ molecules react with the alkenes of the polymethine chain of the fluorophore to (B) form dioxetanes ($C_2O_2H_4$) which, in turn, (C) thermally fragment to yield two non-fluorescent carbonyl leucoforms. ..... 67

**Figure 3-5.** A schematic illustration of the change in the solid angle of emitted light as it travels towards a detector from the source (S). This change is due to differences in refraction ($\Theta$) caused by the different solvent refractive indices ($n_i$, $n_g$, $n_o$) through which the light propagates. Reproduced from Lakowicz (2006).[37] ..... 72

**Figure 3-6.** (A) Optical Density of $10^{-6}$ M ICG in 7:3 EtOH:$H_2O$ solution. The line at 785 nm shows the OD for this solution concentration used in the determination of the optical density-emission behavior as part of the calculation of $\Phi$. (B) Emitted intensity of the $10^{-6}$ M ICG solution at 785 nm excitation. The area under the curve

is the integrated intensity *I*, and is the second component of the optical density-emission plot needed for Eqn. 3-11 for the calculation of $\Phi_F$. The missing points around 785 nm are the saturation due to the laser line. Here, the integrated intensity is ~70000. (C) Plot and linear fit of integrated emitted intensity vs. optical density for a range of solution concentrations. The circled data point represents the values obtained for the $10^{-6}$ M ICG concentration in panels (A) and (B). The slope of the fit, *I/OD*, is used for the calculation of $\Phi_F$ in Eqn. 3-11.....73

**Figure 3-7.** Absorption (inset) and fluorescence spectra of free ICG (red) and ICG-CPSNPs (black) in aqueous solution. The CPSNP suspension ($10^{13}$ particles/mL) had an apparent fluorophore content of roughly $10^{-5}$ M based on absorption standards; a matching concentration of free dye was used for the comparison. The shape and position of both the absorption and emission spectra are similar, indicating the absence of either chemical modification or dimerization upon encapsulating the dye in the calcium phosphosilicate matrix. Emission from the ICG-CPSNPs is significantly brighter than the matching free dye solution, which suffers from quenching interactions due, in part, to free dye self-aggregation.....75

**Figure 3-8.** A map of the emission peak position and intensity of free ICG as function of concentration and solvent illustrates that ICG is prone to dimerizations that alter the absorption behavior (thus shifts in corresponding peak emission wavelength) and self-quenching effects on fluorescence intensity, that cap the emissive properties of the free fluorophore. The intensity values reported are normalized to the energy of the excitation beam. .....77

**Figure 3-9.** The comparative spectral effect of four bio-relevant solvents on the emission response of (A) free ICG dye and (B) dye-doped ICG-CPSNPs. The normalized peaks spread across 18 nm for the free fluorophore (standard deviation of 7.8 nm), while encapsulation in CPSNPs has an order of magnitude smaller 1.6 nm spread (0.68 nm standard deviation). This data confirms the largely impermeable nature of the CPS matrix to the surrounding environment, shielding the encapsulated dye from solvent interaction. .....78

**Figure 3-10.** Fluorescent half-life for a free ICG fluorophore (red) and ICG-CPSNP (blue) suspension of matching absorption ($10^{-6}$ M) in PBS under 785 nm excitation at two power densities. Encapsulation provides an average of 470 percent increase in half-life at an excitation power commonly used in clinical settings (~100 mW/cm$^2$), and a 240 percent increase under even extremely high laser power density (1000 mW/cm$^2$). .....79

**Figure 3-11.** Plots of integrated emitted intensity vs. optical density for HITC (reference dye in MeOH, $\Phi_F = 0.28$) and (A) free ICG in 7:3 EtOH:$H_2O$ and phosphate buffered saline ($\Phi_F = 0.084$ and $\Phi_F = 0.027$, respectively) and (B) ICG-doped CPS particles in 7:3 EtOH:$H_2O$ and phosphate buffered saline ($\Phi_F = 0.055 \pm 0.003$ and $\Phi_F = 0.053 \pm 0.003$, respectively). The $\Phi_F$ for ICG-CPSNPs in both solvents is identical to within the 95% confidence interval, verifying that the encapsulated ICG is shielded from the particle's external environment. .....81

**Figure 4-1.**The schematic illustration represents the two modes of tumor targeting. (A) Passive localization occurs by combined effects of the extravasation of agents through increased permeability of the tumor vasculature and retention due to ineffective lymphatic drainage (EPR effect). (B) A possible mode of active targeting achieved by functionalizing the surface of nanoparticles with ligands that promote cell-specific recognition and binding. The agent can (i) attach to the membrane before (ii) being internalize into the cell. The illustration modified from Peer et al.[212] ...91

**Figure 4-2**. Zeta potential distributions of CPSNP suspensions of various functionalities in 7:3 EtOH:$H_2O$ (pH 7). The zeta potential of an as-synthesized suspension of citrate-functionalized CPSNPs is -29 ± 3 mV (blue), consistent with the carboxylate ($COO^-$)-termination. Upon PEGylation of the surface, the distribution of charges clearly shifts away from the net negative charge of the original surfaces towards a net zero charge (3 ± 2 mV; red) characteristic of the PEG molecules. The broadened distribution is characteristic of measurements of zero charge. The surface charge of gastrin-10 conjugated CPSNPs was also examined, which showed an additional shift in distribution towards a more net positive surface charges (+6 ± 3.2 mV; violet). .....98

**Figure 4-3.** NIR transillumination images (Ex. 755 nm, Em. 830 nm) taken at various times (A – 3 hours, B – 24 hours, and C – 96 hours) track fluorescence signals and pharmacokinetic distributions for the ICG-CPSNPs and controls delivered systemically via tail vein injections in nude mice implanted with subcutaneous human breast adenocarcinoma tumors. Hash marks next to each mouse indicate the position of the 5 mm tumors. Two control samples (i) carboxylate-terminated CPSNPs without ICG encapsulant and (ii) free ICG, match the particle concentration and fluorophore content ($10^{13}$ particles/mL and $10^{-5}$ M, respectively) of a (iii) PEGylated ICG-CPSNP sample. (Bii) No fluorescence signal is detected from the free ICG at 24 hours post injection while the ICG-CPSNP-PEG sample (Ciii) retains significant signal even after 96 hours. (Biii) The fluorescence signal is unmistakably localized in tumors 24 hours after administration with PEGylated ICG-CPSNPs. The excised organs in panel (D) illustrate the biliary clearance route 24 hours post-injection of ICG-CPSNP-PEG. Fluorescence signal is not seen from the stomach with minimal renal involvement. .....100

**Figure 4-4.** Gastrin receptor-targeted CPSNPs effectively targeted human BxPC-3 pancreatic cancer cells. BxPC-3 cells were exposed to fluorescein-loaded untargeted PEG-CPSNPs, or Gastrin-10-PEG-CPSNPs, for 5 minutes followed by exchange to fresh media for 55 minutes, or exposure for 60 minutes. (A) Cells were fixed and visualized by microscopy. (B) Cells were fixed and analyzed by flow cytometry with graphs representing 10,000 collected events per sample. .....103

**Figure 4-5.** Targeting gastrin receptors in an *in vivo* orthotopic-tumor model of pancreatic cancer. Human BxPC-3 pancreatic cancer cells were xenografted orthotopically into athymic nude mice. (A) One week following engraftment, ICG-loaded CPSNPs were administered systemically via tail vein injection and near-infrared images were taken 24 hours post-injection. From left to right, mice receiving: (i) untargeted ICG-CPSNP-PEG, (ii) targeted CPSNP-PEG-Gastrin-10. Series (iii) is a third conjugation system not pertinent to the discussion of this work.

(B) Excised, tumor-bearing, pancreases from each mouse and excised brain (mouse ii). All images are representative of at least four independent experiments. .....104

**Figure 5-1.** A simple Jablonski diagram highlighting (yellow) the processes involved in the photoexcitation of molecular ground state oxygen to a biologically active singlet state ($^1O_2$) that serves as the initiating element of photodynamic therapy. The excited singlet state of the photosensitizer is transferred to an excited triplet via an intersystem crossing pathway, from which energy is relaxed back to the ground state through a collisional energy transfer with a proximal oxygen molecule. .....111

**Figure 5-2.** Schematic illustration of the two possible photochemical reactions for the relaxation of an excited triplet state photosensitizer ($S_3$); Type 1 sensitizers initiate radical reactions through either electron or hydrogen atom abstraction and can proceed in the absence of molecular oxygen. In Type 2 reactions, molecular oxygen is involved and can react with the $S_3$ in a spin-conserved reaction to regenerate the ground-state sensitizer and form $^1O_2$. .....113

**Figure 5-3.** Molecular orbital diagrams for the three electronic configurations of molecular oxygen. The top is the triplet ground state, whereas the bottom right is the singlet oxygen $^1\Delta_g$ excited state, and left is the singlet oxygen $^1\Sigma_g^+$ excited state. Note that the states only differ in the spin and the occupancy of the two degenerate antibonding $\pi_g$-orbitals. .....115

**Figure 5-4.** The 530 nm SOSG emission intensity quenches over time, corresponding to both the excited lifetime of singlet oxygen as well as associated excited state quenching of the fluorescence probe itself. A 5% decrease in the emission is observed within 2 minutes after irradiation. .....126

**Figure 5-5**. A comparison of the SOSG intensity as a function of photosensitizer concentration reveals a 60% greater response from ICG molecules encapsulated within CPSNPs compared to the free fluorophore. The SOSG intensity correlates to the level of photoactivated singlet oxygen. Experiments were conducted in a hypoxic (8.3 mg/L dissolved $O_2$) aqueous solution in $D_2O$ at 37$^o$C. Each data point is the mean of five separate runs normalized to energy density (J/cm$^2$). The green lines correspond to the 95% confidence interval of the linear fits. .....128

**Figure 5-6.** The SOSG signal intensity as a function of laser fluence reveals a non-linear response indicative of the finite therapeutic capacity of a single encapsulated ICG photosensitizer molecule. The linear region of the fitted red curve will be used to model dosing response. The green curves correspond to the 95% confidence bands of the polynomial fit. SOSG intensity qualitatively represents the level of generated singlet oxygen for therapeutic function. .....129

**Figure 5-7.** An encapsulated ICG and laser fluence dosing map for SOSG intensity is constructed from the linear region of the ICG therapeutic capacity relationship depicted in Figure 5-6. The map visually relates the SOSG signal intensities as a function of photosensitizer-laser energy density combinations. .....130

**Figure 6-1.** The dark toxicity of ICG-CPSNPs is determined by examining the cell viability in multiple cell lines as a function of encapsulated fluorophores. For the colorectal cancer lines HT29 and HTC116, the median lethal dose ($LD_{50}$) is not reached until an encapsulated ICG concentration between 50 and 60 nM. The MDA-MB-231 and BxPC-3 lines did not exhibited significant acute dark toxicity within the concentration ranges examined. .....142

**Figure 6-2.** The acute toxicity of CPSNPs is determined by examining the cell viability in multiple cell lines as a function of Ghost-CPSNP-PEG particle concentration. For the colorectal cancer lines HT29 and HTC116, the median lethal dose ($LD_{50}$) is found to be $1 \times 10^{12}$ particles. This amounts to approximately $2 \times 10^{8}$ CPSNPs per cell. The MDA-MB-231 and BxPC-3 lines exhibited an approximate $LD_{50}$ towards the limit of the examined particle concentration range around $1.5 \times 10^{12}$. .....142

**Figure 6-3**. Cell viability in response to PDT from ICG-CPSNP-PEG relative to a control (dark) group are presented. The photosensitizer concentration ranged from 11 – 44 nM, three orders of magnitude lower than concentrations reported in the literature. The fluence rate was also significantly reduced (1 J/cm$^2$) compared to conventional irradiation energy densities. A marked decrease in cell viability is observed even under this low dose PDT regime for three of the four cell lines examined, suggesting remarkable therapeutic promise under clinical conditions.....144

**Figure 6-4.** The cell viability of MDA-MB-231 human breast carcinoma cells is seen to decrease with an increase in laser fluence for a set photosensitizer concentration (22 nM). This behavior serves to highlight the remarkable potential of ICG-CPSNP mediated PDT in clinical settings, which presently exhibits notable photocytotoxicity under significantly low PDT parameters.....145

**Figure 6-5.** A first-generation dosing map charts the *in vitro* cell death count of MDA-MB-231 human breast adenocarcinoma cells as a function of the combination of ICG-CPSNP photosensitizer dosage and 785 nm fluence rate. .....146

**Figure 6-6.** A relative tumor volume as a function of time post therapy plot for an *in vivo* PDT trial on MDA-MB-231 human breast cancer xenografts in nude mice. Each animal received a single systemic injection of sample or control and one irradiation dose (12.5 J/cm$^2$) per tumor. The ICG-CPSNP-PEG clearly arrest tumor growth over the 36 day period, while all other control groups grew to 10-fold their initial size. .....147

# ACKNOWLEDGEMENTS

First and foremost, I would like to thank my thesis advisor, Dr. James H. Adair, for providing me with the opportunity to work on and contribute to this project. His support and confidence in my abilities, particularly early on, were paramount in my development and growth as a scientist.

I would also like to thank the collaborative team that has helped shape this project into a truly multidisciplinary cooperation. The indispensable direction of the late Dr. Peter Eklund of the Physics Department must be acknowledged and is greatly appreciated. His unmatched insight of photophysical processes and optics, especially in the early stages of the project, underlines the work presented. Also, I specifically thank Dr. Tim Russin for his partnership in the optical evaluation of these composite particles, without whom the original fluorescent assessments would have been considerably more arduous. The invaluable efforts of the Dr. Mark Kester research group of the Penn State Hershey College of Medicine's Department of Pharmacology are also graciously acknowledged. In particular, the original efforts of James Kaiser involving the initial whole animal imaging experiments are recognized. In addition, I thank Dr. Brian Barth for his enormous collaboration in designing and implementing the medical facet of this work. I must also thank my committee members for their guidance over the course of this dissertation.

I would like to thank the support and assistance of the members of the Adair research group, both past and present. The collective gratitude to this group of individuals for the contributions to the development of these particulate systems is beyond measure. The cooperative dynamics and support among all members has made my experience in graduate school that much better.

Finally, I would like to thank my family for the emotional support they have provided over these many years. In particular, I would like to thank my father, to whom this work is

dedicated, for his devotion to providing for both my brother and I all we have ever needed, both educationally and privately. I must also thank him for encouraging us to remain strong and focused, and for the countless sacrifices he has made to ensure the three of us are all the more close after our mutual loss.

***Babam***

*Bana gerçek yolu gösteren babam*
*Beni okutan babam*
*Beni seven babam*
*Benim canım babam*

*Bana herşeyi alan babam*
*Bana herşeyi kazandıran babam*
*Beni seven babam*
*Canım babam*

*Seni seviyorum babam*
*Kalbimdesin babam*
*Saçın beyazlandı babam*
*Seni seviyorum babam*

*Dünyalar benimdir babam*
*Bana herşeyi alan babam*
*Senin oğlunum babam*
*Seni seviyorum babam*

- *Evran Gund*

Şimdi sıra bende baba. Teşekkür ederim.

# Chapter 1

## Introduction

An increasing awareness of rising treatment costs and the improved efficacy associated with earlier detection of disease[1] continue to shift clinical research into the realm of predictive medicine and facile, non-invasive therapeutic strategies, particularly in the realm of oncology. The ability of physicians to effectively treat and cure cancer is directly dependent on their ability to detect the disease at its earliest stages (Figure 1-1).[2, 3] The American Cancer Society estimated 1.5 million new cancer cases diagnosed in the past year alone.[4] Unfortunately, limitations of current detection schemes impede diagnosis until cancer cells have already invaded surrounding tissues (stage III) and metastasized throughout the body (stage IV), resulting in an exponentially more difficult condition to treat and thus necessitating more austere treatment strategies; approximately 80% of last year's diagnoses were in such later stages at the time of presentation, requiring treatments involving infusions of toxic pharmaceuticals and blasts of brutal radiation, for which the prognosis is as miserable as the experience itself. The projected mean 5-year survival rate from a disseminated disease (stage III or IV) for all cancer types drops drastically to less than 20%,[4] due principally to the limited success most conventional therapeutics offer once a tumor has spread beyond the tissue of origin.[2]

Detecting at early, even premalignant, states of the progressive disease means that various low risk and highly effective treatment strategies will have a higher probability of truly eradicating the cancer,[2, 5] resulting in estimated 5-year survival rates of over 90%,[4] with minimal, if any, adjuvant therapies.[6] Thus, the advantages associated with the timely detection and treatment has generated interest in a simultaneous approach to early diagnosis and therapy far in

advance of changes on the gross anatomic level,[7-916] initiating improvements to clinical imaging modalities and the development of low dose, low risk treatment strategies for early stage diseases.

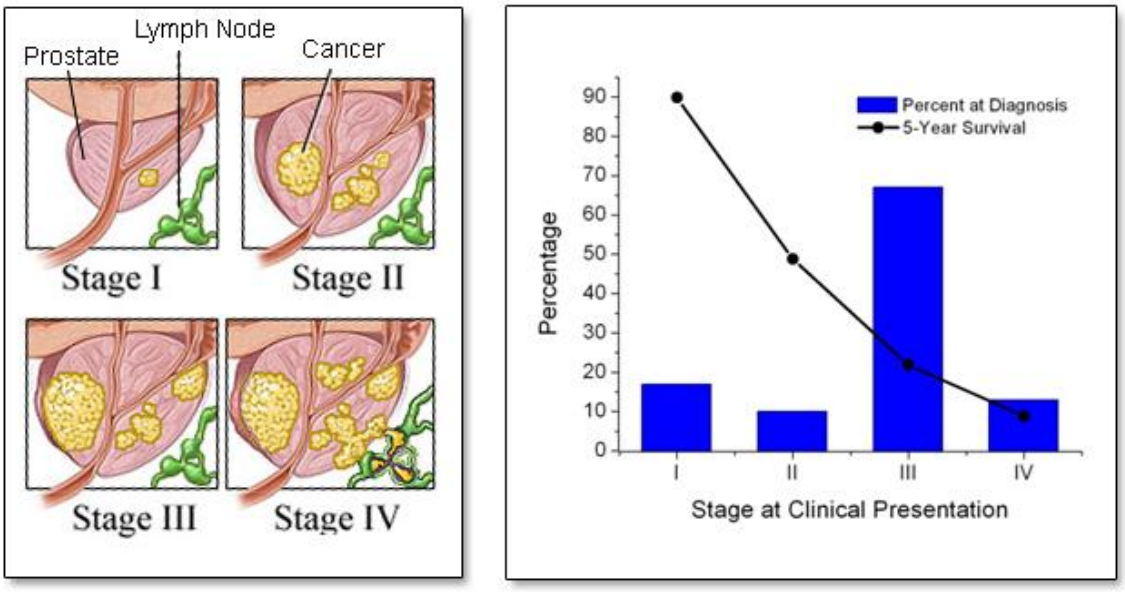


**Figure 1-1.** An illustrative example of the Overall Stage Grouping of cancer in presented for prostate carcinoma. General classifications define stage I cancers are localized to within the tissue of origin, while state II is considered locally advanced, and stage III has spread to proximal tissues. Stage IV cancers are categorized as having metastasized and spread to other organs of the body. The percentage of each stage at time of clinical presentation is plotted (blue bars) in relation to the projected 5-year survival rate associated with each stage (black points).[4] It is clear that the later the stage of the disease at diagnosis, the significantly poorer the prognosis. The staging illustration has been modified from Ref. 10.

### 1.1 Early-Stage Near Infrared Imaging

Imaging in biological systems has become one of the most relied upon tools used by health care professionals in the diagnosis and treatment of human disease.[11] Due to their potential as a noninvasive and non-ionizing technique, optical imaging methods are regarded as some of the most attractive of clinical imaging modalities, though they are currently hampered by the present limitations of penetration depth and achievable resolution, which severely hinders the detection of early-stage, small volume lesions.[2] Conventional imaging methods, such as

mammography and optical tomography, are based on visualizing morphological alterations, and are thus limited to a minimal lateral resolution of 0.5-1 cm.[12] This makes observation of regional and distant metastasis, and the sensitivity for detecting early-stage lesions, particularly difficult and inadequate. Furthermore, present contrast enhanced approaches, such as that applied to transillumination imaging, suffer from the high absorption and autofluorescence that occur in biological tissues across most of the electromagnetic spectrum, further limiting precision and resolution.[13, 14]

Fortunately, the full potential of optical imaging can be achieved with the use of contrast agents that emit in the near infrared (NIR) region (700–1100 nm) of the spectrum,[15] where the influence of the main tissue absorbing components, oxy- and deoxyhemoglobin ($\lambda_{max}$<600 nm) as well as water ($\lambda_{max}$>1150 nm), are minimal (Figure 1-2).[16, 17] As a result, NIR light penetrates deeper into and out of tissues, extending the resolvable tissue depth limit of conventional light emitting modalities to several centimeters of tissue.[8, 14, 18] Furthermore, endogenous cellular components produce little autofluorescence across this region, diminishing background interference and enhancing signal-to-noise ratios, providing very low detection limits with NIR fluorescence.[19, 20] Also, since it is the discrete, molecular-scale exogenous agents that produce the NIR signals that are imaged, diagnostic observations are no longer dependent on macroscopic morphological variations, providing improved resolutions, and thus enhanced diagnostic sensitivity.

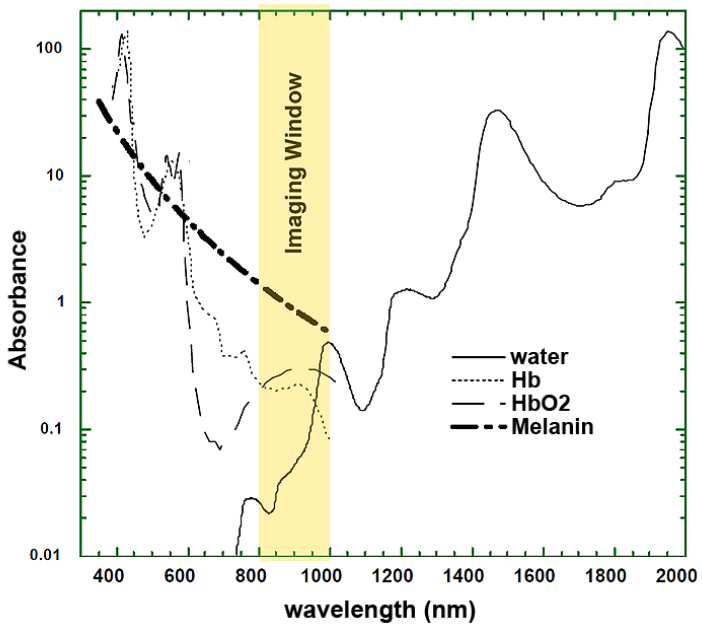


**Figure 1-2.** NIR absorption spectrum of water and main tissue absorbing components, oxy- and deoxyhemoglobin. The highest optical transmission, the "imaging window", between 800 and 1000 nm, is highlighted.[21]

## 1.2 Indocyanine Green

Indocyanine green (ICG) is a NIR contrast agent which has been widely investigated for use in deep tissue imaging, and is the only NIR organic dye approved by the U.S. Food and Drug Administration (FDA) for human use.[22] ICG is an amphiphilic carbocyanine dye that exhibits absorption and emission maxima around 785 and 820 nm, respectively.[23-25] Figure 1-3 presents the structure of ICG. Due to its low toxicity ($LD_{50}$ of 50-80 mg/kg for animal subjects[26]), ICG is used clinically as a contrast agent for optical imaging in angiography[27] and guiding biopsies,[28] as well as for evaluating blood flow[29, 30] and hepatic function.[31, 32] It is one of the least toxic contrast agents administered to humans,[33] with the only known adverse reaction being rare anaphylaxis.[34]

However, as with many organic dye molecules, ICG has a low fluorescence quantum yield due to internal conversion,[35, 36] and is prone to photobleaching, solvatochromic effects, and

nonspecific quenching, all of which limit its utility in sensitive and prolonged *in vivo* imaging applications.[18, 24, 35, 37, 38] Numerous efforts have reported the optical instability of ICG in physiologically relevant solutions such as water,[25, 39, 40] salt solutions,[25, 41] plasma,[25, 40, 41] and blood.[40, 42-44] In such environments, oxidation and dimerization degrade the original molecule, resulting in decreased absorption, reduced fluorescence, and variability in the maximum absorption wavelength.[45, 46] Furthermore, ICG often binds to proteins[47] leading to rapid agglomeration and subsequent elimination from the body with an initial plasma half-life of two to four minutes, and a secondary clearance time for lower concentrations ranging close to 60 minutes.[39, 43] This is particularly problematic for applications where a high concentration of ICG is needed in circulation for extended periods of time, on the order of several minutes, such as real-time tracking and diagnostic screening. Thus, despite possessing the intrinsic capacity to serve an exceptional function in deep tissue imaging applications, ICG, like its other organic fluorophore counterparts, suffers from practical setbacks that impede the full potential of NIR imaging. As a consequence, recent interest has turned to developing alternate, inorganic emitters as surrogates to impart the fundamental advantages of NIR optical schemes.

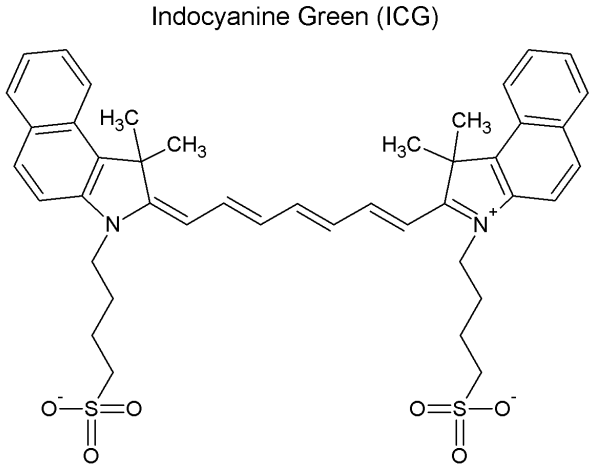


**Figure 1-3.** The structure of the carbocyanine dye indocyanine green (ICG) is illustrated. This NIR active fluorophore exhibits absorption and emission maxima around 785 and 820 nm, respectively.

### 1.3 Nanoparticle (NP)-Based NIR Imaging Agents

Most sensitive imaging protocols employ exogenous contrast agents to exaggerate signals and boost detection and sensitivity. The primary criterion for an effective agent is that it is non-toxic and prompts no adverse immunogenic responses. Unfortunately, most non-toxic organic NIR contrast agents, such as ICG, suffer from rapid photobleaching,[19] non-specific adsorption of proteins and biological and chemical degradation[48] as introduced above. As a result, NIR signals swiftly decrease once exposed to the excitation light source, limiting detection sensitivity of the target. Furthermore, organic agents tend to aggregate, causing spectral shifts and reduced emission signals, and often prematurely sequester in untargeted tissues. These restrictive properties of organic NIR emitting fluorophores have encouraged the development of numerous alternate NIR emitting probes such as nanoparticle (NP)-based contrast agents. The development of nanoprobes with high sensitivity and specificity for NIR *in vivo* imaging and high-throughput analysis is now of considerable interest in a number of research areas including molecular biology, molecular imaging, drug screening, and biomedical diagnosis.[3, 49] The last decade alone has attracted immense interest in the field of NP-based imaging technologies, particularly since nanoprobes provide several common advantages over traditional organic contrast agents.[48] Unlike organic fluorophores, NP contrast agents are not prone to the same rapid photobleaching, allowing long-term, sensitive tracking of signals with heightened specificity and resolution.[50] Furthermore, NP agents possess unique features that can be exploited for improved imaging protocols to detect early stage cancers.[3] Among these are the ability to manipulate surface structures for enhancement of uptake and targeting by selected cells, engineer function-specific responses for diagnostic purposes, and to alter pharmacokinetics permitting extended imaging time courses in physiological environments. Thus, NP-based NIR probes present a new class of

contrast agents that provide improved optical properties and imaging potentials for sensitive, early stage detection schemes.

### 1.3.1 Criteria for Exogenous Particulates for Imaging Applications

Nanoparticulate-based approaches to NIR optical imaging serve to overcome the limitations plaguing traditional NIR emitting contrast agents. The improved performance NIR nanoparticulate contrast agents rely strongly on several factors, and a robust particle design is the key to effective utility in imaging applications. The NP-based agents should have a strong detectable signal in the NIR region, specifically in the range of 800 - 850 nm, because of the low tissue absorptivity in this wavelength region (Figure 1-2). The detectable signal should be stable and exhibit an extended lifetime for long term imaging protocols. The NPs themselves should have limited susceptibility to photo-, biological-, or thermal-degradation, as well as minimal solvatochromic effects, permitting consistent imaging in a variety of physiological environments. These platforms should also be colloidally stable in the complex aqueous physiological environments, remaining completely dispersed without agglomeration. This in turn permits long-term circulation of the NPs without sequesteration in organs or membranes, events that may cause local cytotoxic effects. Additionally, the NP-contrast agents should be biocompatible and systemically non-toxic for safe administration, including rapid and complete clearance from biological systems after completion of their tasks to avert any long-term exposure effects. Unfortunately, no single platform currently satisfies all these criteria to the full extent. However, semiconductor nanocrystals, resonant nanoshells, and dye-encapsulating nanoparticle platforms each satisfy a unique set of these criteria to different degrees, and present themselves as the best options available to date for the future direction of NIR imaging.

### 1.3.2 Semiconductor Nanocrystals

Semiconductor nanocrystals, or quantum dots (QDs), have been the subject of great scientific and technological interest, particularly for their utility in long-term, multi-target and highly sensitive bioimaging applications.[48] This interest is due to their substantial advantages over conventional fluorophores. QDs exhibit many desirable properties for improved imaging, including high quantum yield (>50%),[51] high molar extinction coefficients (~600,000 $M^{-1}cm^{-1}$, roughly an order of magnitude higher than even the strongly absorbing Rhodamine 6G),[52, 53] and intense fluorescence (most QDs are approximately 10-20x brighter than organic dyes).[54, 55] Unlike organic dyes, the excitation and emission spectra of QDs are well separated; since the absorption probability of QD nanocrystals increases at shorter wavelengths (higher energy), QDs exhibit an almost continuous, broadband absorption and a narrow emission spectrum (typically 20–30 nm full width at half maximum),[56] resulting in a large effective Stokes shift.[57] Although the luminescence properties of QDs have historically been sensitive to their local environment, recent core-shell geometries for which the nanocrystal is encased in a shell of a wider band gap semiconductor, have resulted in increased fluorescence quantum efficiencies and greatly improved resistance to photobleaching and improved photochemical stability,[51] resulting in relatively long fluorescence lifetimes (>10 ns) compared to fluorophore molecules.[48]

Quantum dots have unique size- and composition- dependent optical and electrical properties. The absorption is associated with the promotion of electrons from the conduction band to the valence band when the excitation energy exceeds the band gap energy between two electronic bands (semiconductor band gap), resulting in the formation of an electron-hole pair, called an exciton. When the QD is smaller than the Bohr exciton radius (which is typically a few nanometers), the quantum confinement effect is observed in such nanocrystals. In this situation, QD energy levels are quantized, with values directly related to the QD size. QD fluorescence is

due to a radiative recombination of an exciton, leading to the emission of a photon in a narrow and symmetric energy band, typically in the visible to NIR spectral range.[57] Of particular interest are type-II QDs, first reported by Hatami *et al*.[58] and Youn *et al.*[59], which consist of materials for which both the valence and conduction bands in the core are lower (or higher) than in the shell. The staggered band lineup of type-II compared to type-I heterostructures are illustrated in Figure 1-4. As a result, one carrier is mostly confined to the core, while the other is mostly confined to the shell, a novel property known as *spatial separations of carriers*. Since fluorescence emission originates from the radiative recombination of the electron-hole pair across the core-shell interface,[60] the energy of the emission depends on the band offsets of the two materials making up the core and the shell. Thus, type-II QDs can emit at energies that are less than the band gap of either material, which allow access to higher wavelengths that would otherwise not be available with a single material.[60] The first report of such NIR emitting type-II QDs was the synthesis of CdTe/CdSe and CdSe/ZnTe (core/shell) colloidal heterostructures by Kim *et al.*[60] These NIR-probes are rendered soluble in aqueous buffers with an oligomeric phosphine coating. Recently, a new class of alloyed semiconductor QDs (ternary CdSeTe) were reported that also boast emission in the NIR spectrum by tuning both alloy composition (the Se:Te molar ratio) and internal structure.[61] These alloyed QDs are also coated to promote greater biocompatibility by using the same surface-modification and cross-linking procedures reported for CdSe [62, 63] and CdTe binary quantum dots.[64]

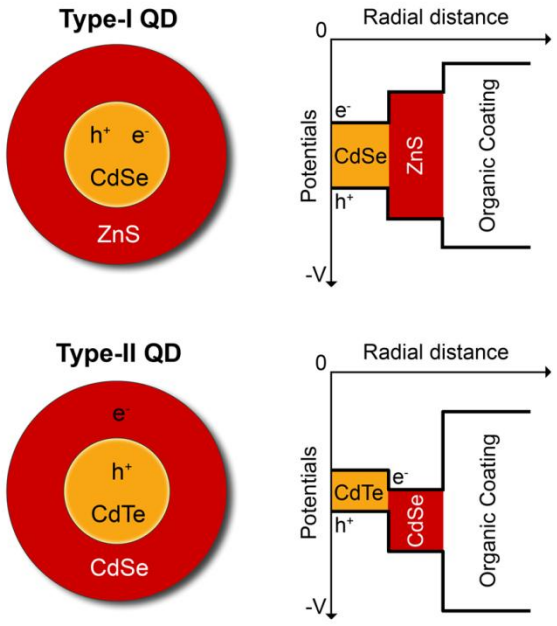


**Figure 1-4.** Illustration of band gap structures for Type-I and Type-II semiconductor heterostructures. Type-II structures have a staggered bang gap as a result of the valence and conduction bands of the material used in the core being lower (or higher) than those in the shell. This results in a spatial separations of carriers, as one carrier is mostly confined to the core, while the other is mostly confined to the shell. This in turn allows emission at energies that are smaller than the band gap of either material, which permit access to higher wavelengths in the NIR.[65]

Unfortunately, several issues related to the health risks of QD use, including cytotoxicity to organelles and membranes, induced apoptosis, and peroxidative stress, may limit their potential future in clinical settings.[66-75]. Gerion *et al.*, among others, assert that the surface treatment of nanocrystals specify the biological behavior of whole nanocrystalline QDs. Specifically, it is the stability of these QD core-bioactive complexes that may render QDs potentially harmful.[76] The CdTe(CdSe) type-II NIR QDs use an oligomeric phosphine coating to render them dispersable in aqueous buffers.[65] While the initial mapping application with these QDs showed no signs of toxicity within 15 minutes, Cho *et al.*[77] maintain that prolonged contact of hydrophilic QDs with biological fluids can cause partial desorption of the coating layer, exposing the bare semiconductor surface to the biological milieu, with possible detrimental consequences of these

heavy metalloids on the in vivo environment. Furthermore, recent work by Smith *et al.*[78] has shown that these surface coatings are ineffective in protecting QDs against proton etching in strongly acidic environments, such as those in endolysosomes during cell uptake[79, 80] or around solid tumors.[81] It is believed that small molecules or ions such as hypochlorous acid and protons are able to diffuse across the surface coating layer, causing the etching of chalcogenide atoms on the QD surface.[82] This etching has detrimental implications on the emissive properties of the QDs. The fluorescence emission spectra of lipid-PEG coated CdSe/CdS/ZnS core-shell QDs was shown to both blueshift in wavelength and drop dramatically in intensity after only one hour of exposure to acidic environments.[83] This possibility of shell deterioration and leakage of metal ions was further supported through the observations of a decrease of photoluminescence intensity and a blueshift of luminescence spectra of QDs inside living cells.[84] This is especially plausible for the phosphine ligands used with NIR QDs since, in principle, at low pH, the phosphine lone electron pair will protonate and detach from the nanocrystal surface. Such a displacement reaction is promoted in intracellular environments,[85] Additional studies further attribute the cytotoxicity of QDs to intracellular degradation.[67, 69, 73] Since the intracellular environment has been shown to degrade both surface-coatings and ultimately the QD itself,[73, 83] the implication is that the nanocrystal degradation into toxic, metalloid constituents affects cell viability.[69] Recent work [73] has demonstrated that all surface-modified QDs are equally cytotoxic when intracellular-exposure levels are compared.[73] This has been attributed to the breakdown of endocytosed QDs by cellular degradation mechanisms.[67] Of note, those studies that observed no QD cytotoxicity generally employed protocols that used short-term acute exposures, where cells were in contact with QDs for 15 min to eight hours.[65, 76] In particular, sentinel lymph node (SLN) mapping studies with QDs take place in under an hour. In contrast, QD-induced cytotoxicity is generally found in studies that tend to be longer in nature, with exposure times from 2 hours to several days.[86-89] While many *in vivo* imaging applications take relatively short amounts of time (approximately 15

minutes),[65] tracer particles not bound to the positive-site or that may otherwise remain *in vivo* after the procedure could potentially linger in the body until degradation or eventual secretion occurs. Kim *et al.*[65] determined that only 2-4% of the injected NIR-QD dose in their mapping study actually accumulated in and was subsequently removed from the SLN. The remaining material could bioaccumulate and potentially present problems of heavy metal toxicity, as QD metalloid constituents have been shown to reside in cells for weeks[76] to years.[90] While such concerns limit its *in vivo* potential, QDs are successfully used for *in vitro* diagnostic or biological assay applications, where issues of long term toxicity is less of a concern. Nevertheless, despite these probable toxicity-based limitations in long-term *in vivo* imaging applications, the improved performance in optical tracking and heightened sensitivity underscores the potential for nanoparticle mediated NIR imaging to provide enhanced properties for superior bioimaging.

### 1.3.3 Resonant Nanoshells

Metal nanoshells are a relatively new class of nanoparticles with highly tunable optical properties. Although nanoscale metals like gold and silver do not fluoresce, they effectively scatter light due to the collective oscillation of their conduction electrons induced by the absorption of photons from an incident electric field. This is known as surface plasmon resonance (SPR).[48] Nanoshells offer the ability to manipulate the relative scattering and absorption efficiencies by altering the size and composition of the structure; absorption is enhanced with smaller plasmonic nanoparticles, while scattering cross sections increase as particles get larger.[91-94] Oldenburg *et al.*[92] were the first to develop a new class of nanoshells that overcame many of the synthetic limitations of earlier formulations, particularly independent control over core and shell sizes. These particulate contrast agents consist of a nanoscale dielectric core, such as silica, surrounded by an ultrathin metal shell, often composed of gold. By adjusting the size of the

nanoparticle core relative to the thickness of the gold shell, the optical SPR wavelength of nanoshells can be precisely and systematically tuned over a broad range of wavelengths, including the NIR region.[95] For example, Halas *et al.*[92] reported that gold nanoshells can be designed such that the plasmon peak can be tuned to cover a designed spectral response anywhere from 600 to 1200 nm, encompassing the visible-red to infrared range. This tunability is demonstrated for nanoshells with a 60 nm silica core radius and gold shells 5, 7, 10, and 20 nm thick in Figure 1-5.[14] Compared with NIR molecular contrast agents, such as indocyanine green (ICG), nanoshells have far larger absorption cross-sections, $1.66 \times 10^{-20}$ $m^2$ compared to $3.8 \times 10^{-14}$ $m^2$ at 800 nm, respectively.[14, 94] Furthermore, in contrast to NIR absorbing dyes, the absorption properties of nanoshells are dependent upon a rigid metallic structure rather than on molecular orbital electronic transitions. Because of this, nanoshells are not susceptible to photobleaching and have limited susceptibility to chemical and thermal denaturation.[95]

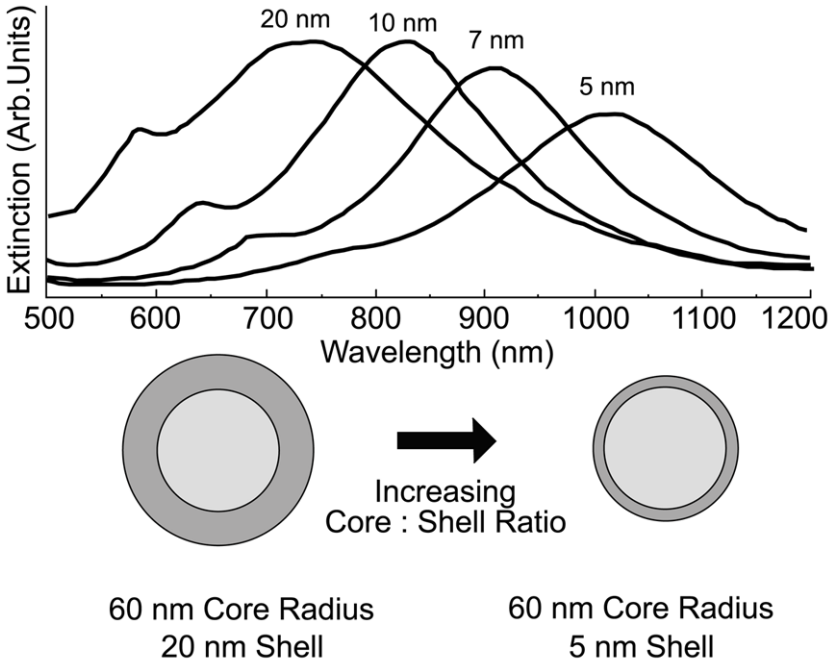


**Figure 1-5.**Optical tunability demonstrated for nanoshells with a 60 nm silica core radius and gold shells 5, 7, 10, and 20 nm thick. The plasmon resonance (extinction) of the particles red shifts with decreasing thickness of the gold shell (or an increasing core:shell ratio). Nanoshells are easily fabricated with resonance in the NIR.[14]

Employing gold nanoshell-based NIR contrast agents has several advantages over NIR QDs including the absence of toxic heavy metals, a biocompatible surface, and facile aqueous dispersability. However, clearance of these nanoshells from the physiological system is still a matter of concern. Retention and accumulation of any exogenous particle, even the most benign of materials, has the potential to interfere with biological functions.[96] Thus, when considering the injection of particulates for imaging purposes, it is imperative to understand where the contrast agents might accumulate in tissue, in addition to the target sites, and in what quantities and over what time course these accumulations occur. James *et al.*[97] undertook a comprehensive biodistribution study using neutron activation analysis (NAA) to precisely determine gold (and thus nanoshell) localization and quantity in complex tissue matrices. The nanoshells used in their study were silica-gold core-shell nanoparticles with nominal particle diameters of 110 nm cores and 10 nm thick shells stabilized by coating with polyethylene glycol (PEG).[97] Their findings indicated that the highest accumulation of the nanoshells occurs in the organs associated with macrophages from the reticuloendothelial system (RES), notably including muscles, brain, and bone. Figure 1-6 shows the 24 hour post-injection ratio of gold concentrations in various organs to the concentration within the tumor. Their findings revealed that tumor uptake is low and inefficient, with significantly elevated levels in almost all other tissues, most notably of which is the brain, which measured 200 times greater content of the nanoshells than the tumor tissue (Figure 1-6). Unfortunately this is non-ideal pharmacokinetic behavior; results found that clearances from RES associated organs were slower than expected, with only slight reductions in concentration even after 28 days in the study. In fact, elevated levels of gold were still present within the liver at the end of the study period.[97] Likewise, after the 28 days, between 1–10 ppm gold was detected in bone, muscle, kidney and lung tissues (three orders of magnitude higher than pre-treatment levels). A similar study was undertaken by De Jong *et al.*[98] assessing gold nanoparticle organ distributions in rats after intravenous administration as a function of particle

sizes ranging from 10 to 250 nm via inductively coupled plasma mass spectrometry (ICP-MS). It was determined that the majority of the administered gold sequestered in the liver and spleen for all particle sizes after 24 hours. Interestingly, the smaller particles (10 nm) demonstrated the most widespread organ distribution, being found in various organ systems including the liver, spleen, kidneys, thymus, heart, lung and brain.[98] These findings present the possibility for prolonged-exposure related toxicity, organ failure, or membrane damage[97]

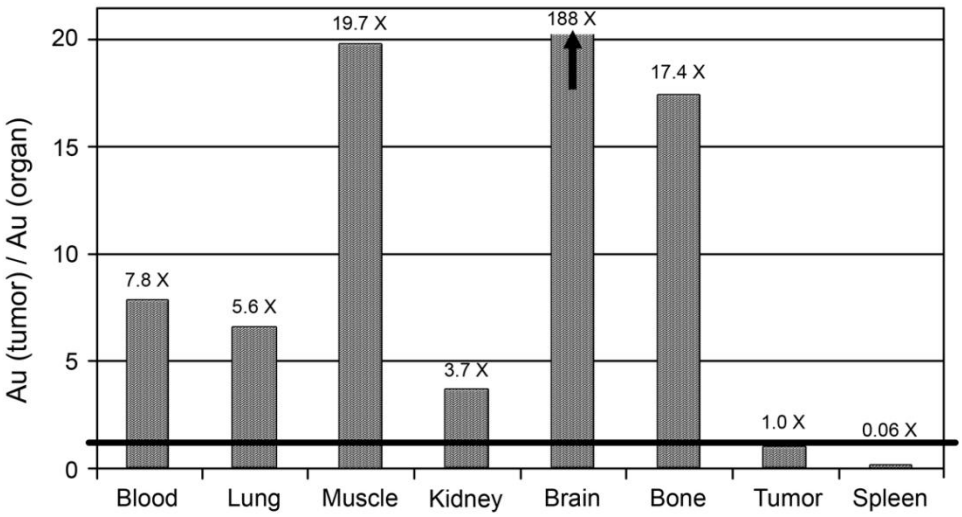


**Figure 1-6.**Ratios of gold concentrations by neutron activation analysis (NAA) in each organ to that in tumor (solid black line) at 24 hours post-systemic administration of PEGylated gold nanoshells. Data reveals unfavorable accumulation of nanoshells in untargeted organs.[97]

Another possible concern of resonant nanoshells is their capacity to generate and dissipate heat to the surrounding environment when illuminated with light of energy close to a surface plasmon resonance of the metal, an effect called a photothermal response.[99] Gold-based nanoparticles have been shown raise local temperatures to, and even beyond, 41-46$^{o}$C, when irradiated with even low irradiation dosages, 10- to 25-fold lower than those used in studies employing photoabsorbing dyes for thermal ablation therapy.[100] This moderate temperature range is termed hyperthermia and causes irreversible cell damage by loosening cell membranes and

denaturing proteins. Moreover, sustaining even a slight rise in temperature (~39$^{o}$C) over a period of a few minutes may lead to the acceleration of biological reactions accompanied by the production of shock heating proteins.[101] While this is a very promising phenomenon presently being exploited for therapeutic applications (termed plasmonic photothermal therapy, PPTT), any derivative heating during solely imaging applications could induce local toxicity. Thus, despite their excellent optical performance, the full potential of this unique technology for *in vivo* imaging applications is presently limited by their unpredictable clearance and photothermal response, which must be fully understood in order to manage any eventual toxicities before success in clinical applications.

### 1.3.4 Dye-Encapsulating Nanoparticle Platforms

The newest class of particulate-based NIR contrast agents is dye-doped nanoparticle carriers. These nanoparticle platforms are engineered to internally encapsulate one or more fluorescent molecules within an optically transparent matrix, rendering the composite a single fluorescent nanoparticle unit. It has been long established that the use of nanoparticles can overcome many of the traditional limitations of *in vivo* conjugation and delivery of bioactive agents,[102] but the concept of encapsulating fluorescent fluorophores within a matrix of material for enhanced optical performance stems from the work of Avnir *et al.*[103] The most promising characteristic of fluorophore-doped nanoparticles is the improved photostability of the encapsulate afforded by its isolation from unfavorable influences of the environment, referred to as a matrix shielding effect.[104, 105] Specifically, it has been observed that this photostability is a result of the inhibition of unfavorable conformational reorganizations[36] and reduced interactions with solvent molecules, limiting the encounter with dynamic processes that result in non-radiative energy losses.[103] However, the primary advantage offered by encapsulation for *in vivo* imaging is

the increase of circulation half-life and *in vivo* signal stability relative to the free constituent fluorophore.[24, 104, 106] To date, numerous nanoparticulate systems have been used to encapsulate fluorescent molecules as composite fluorescent particles to exploit these promising properties for imaging applications.[107]

While the radiative processes of dye-doped nanoparticles are phenomenologically identical to traditional organic fluorophores, the dye-nanoparticulate composite agent has been reported to yield fluorescence intensities of one to two orders of magnitude brighter than corresponding free fluorophores.[102, 104, 105, 108-111] The principal rationale for this heightened intensity is that a single particle can be loaded with several dye molecules, resulting in an overall improvement of absorptivity and emission characteristics of these systems when compared to those of a single isolated molecule.

Originating from the initial properties of caged fluorophores in bulk matrices, efforts for NP-based imaging agents first expanded into the development of sub-100 nm, dye-doped silica nanoparticles. A review of the literature will find a vast body of work with fluorescent silica NPs due to well established synthesis and doping schemes. Silica is an ideal matrix for optical agents because it is photochemically inert, such that the spectral characteristics of the dye molecules remain mostly unaltered; it is optically transparent, allowing excitation and emission light to pass through effectively. Additionally, silica has a rigid structure that efficiently cages the encapsulate without concerns of swelling, porosity changes or leakage across numerous solvent conditions. Furthermore, the surface of silica particles can be readily functionalized for biological applications through well established silane-based chemistry.[48]

Unfortunately, like gold nanoshells, despite their material biocompatibility and facile surface bioconjugation, the low solubility of silica means that dye-doped silica nanoparticles are prone to the same clearance issues and toxicity concerns as their gold nanoshell counterparts. Specifically, silica NPs have been shown to initiate the release of oxidants and free radicals not

only at the particle surface, but also by phagocytic cells attempting to digest the silica particle. Such biological responses have been attributed in the initiation of various diseases including systemic sclerosis and chronic renal disease.[112] This matter has initiated the development of alternate, bioresorbable nanoparticulates that completely dissipate by the completion of the imaging function or innocuously circulate until resorption or clearance from the system.

Polymer-based carriers are one of the most common types of particulate systems employed for *in vivo* applications[113] due to high biocompatibility and the facility with which resorbability is achieved.[114] Recent years have witnessed numerous polymeric modalities to address the intrinsic issues of ICG degradation and rapid blood clearance.[24, 115-117] However, these efforts fall short in improving the optical performance for deep tissue imaging schemes.[24] Polymeric carriers tend to suffer significant leakage, losing considerable payload content during circulation.[118] This reveals that polymer matrices, which are susceptible to swelling and other morphological changes in various solvent environments,[119] are poor at providing the matrix shielding effect that grants improved optical performance over traditional fluorophores; dimerization or photo-isomerisation are apparent in these systems from the red shift in the peak absorbance wavelength[24, 117, 120] and a significant decrease in peak fluorescence intensity,[118] respectively. Furthermore, these carriers would not be suitable for real time imaging and tracking applications since signal stability cannot be controlled. Subsequently, a silica-polymer composite microcapsule was developed to improve fluorophore,[24] but the addition of the nanoparticulate shell increased the particle size to 1 micron. Recent work has improved embedded dye molecule performance in organically modified silicates,[121] but the 100 nm silicate carriers lie on the upper limit of the preferred size range for *in vivo* applications.[122,123]

### 1.3.5 Calcium Phosphate-Based Nanoparticulates

An exceptional alternative to biocompatible and resorbable polymeric systems are calcium phosphate-based nanoparticles. Calcium phosphate (CP) is a primary biomineral that is ubiquitously present in the body[124] and whose functions have long been exploited in biocompatible[125-127] bone substitutes and biodegradable adjuvants.[128] As mentioned, several issues arise when employing exogenous agents for *in vivo* use, particularly the cytotoxicity to organelles and induction of apoptosis,[129] as well as the deposition and clearance from the body.[130] Calcium phosphate is a stable bioceramic that is relatively insoluble at physiological pH but has increasing solubility in the acidic intracellular[79, 80] and clearance route environments.[131] This pH-dependent solubility provides an advantage unique to this particular NP-based contrast system; once the function is complete and targets of interest are imaged, the calcium phosphate-based NPs ultimately dissolve upon eventual uptake into cells or low pH environments during clearance. Fortunately, as a biomineral, CP safely biodistributes and its constituent ions, $Ca^{2+}$ and $PO_4^{3-}$, are species found ubiquitously in millimolar concentrations in the bloodstream.[132] Thus, the bioceramic matrix of calcium phosphate-based contrast agents can not only serve to enhance optical signals for bioimaging applications, but undergo a complete and nontoxic dissolution and clearance from the system at the end of its function, mitigating any of the cytotoxic or long-term accumulation concerns associated with QDs and metal nanoshells. Therefore, though the optical performance has yet to be evaluated, the non-toxic composition and facility by which they are ultimately dissolved and resorbed, indicate calcium phosphate-based NPs a promising option for safe, *in vivo* NIR imaging.

## 1.4 Photodynamic Therapy

A succeeding benefit to early-stage detection of disease is the availability of more moderate therapeutic options for its prompt and total eradication. While in many present cases the best treatment option for complete elimination of the carcinoma is a radical resection of the tumor or source tissue, the potential for equally effective yet minimally-invasive therapeutic approaches, such as photodynamic therapy (PDT), become available when dealing with small, contained lesions. PDT is a developing treatment alternative involving the activation of a photosensitizer by an appropriate light source in the presence of molecular oxygen that locally produces highly reactive singlet oxygen ($^1O_2$) and prompts contained and lethal cell damage.[133] At present, a large number of photosensitizers are in various stages of trials. A relatively recent candidate introduced for photomedicinal practice is ICG, which has demonstrated a potent singlet oxygen-mediated antineoplastic activity, and has the potential to initiate such photodynamic responses at great tissue depths.[134, 135]

The precise and localized effect of PDT not only removes the need for invasive resections, but also improves on conventional non-surgical therapies, such as chemotherapy and radiation treatments. The systemic nature of conventional chemotherapeutic dosing, for example, and its indiscriminate circulation into both diseased and healthy cells, besets upon this current strategy harmful side effects and treatment-associated conditions. Unfortunately, measures to counter-balance the limited pharmacological efficiency and mitigate the pervasive physiological harm associated with such systemic delivery are, at present, addressed by disproportionately high dosing and secondary management of associated side effects. These countermeasures, however, are often insufficient and inadequate. The key to evading a majority of the deleterious consequences of conventional chemotherapy is in circumventing the systemic dosing all together. Employing a methodology that does so would transform the present side effect-laced protocols

into safer and more efficient therapeutic strategies. Thus, by replacing the systemic dosing approach of conventional adjuvant therapy with a localized, site-specific therapy such as PDT, a majority of the deleterious consequences are evaded and therapeutic efficacy is enhanced even at lower, targeted doses.

### 1.5 Theranostics: Personalized Point of Care Medicine

Under the supposition that early treatment drastically upgrades prognosis, the momentum of future treatment protocols is shifting towards commencing therapy directly behind detection. Feasibly, the earliest a therapeutic protocol can be initiated is on the moment of diagnosis, which is only practicable if the means by which the detection was accomplished doubled as the channel for therapy. This pairing of diagnostics with therapy is termed theranostics, and has emerged as an important concept in the contemporary design of nanotechnology-based medicine.[136, 137]

The objective of an ideal theranostic protocol is the ability to routinely administer the bifunctional agent and readily perform the diagnostic screening element such that, if desired, the therapeutic component could be concurrently initiated in a point of care-type therapeutic protocol. The full potential of such an effective joint diagnosis/treatment strategy lies in the ability to engineer a single bifunctional vector with both of the optical and therapeutic properties necessary to complete the separate functions. Such an approach is not only most effective, but would replace multiple physician appointments, from detection through to the treatment series, with a single out-patient, all-encompassing visit, alleviating the patient's overall experience. Thus, the added benefits of such a bifunctional device include the reduction in prolonged treatment regimens, the diminution of adverse systemic reactions, an increase in patient compliance, and a shift of the emphasis in medicine from reaction to prevention.

For a successful bifunctional performance, the criteria for a theranostic agent is twofold: function as a sensitive, deep tissue imaging agent for early stage detection, and execute a localized, highly effective yet moderate therapeutic response adequate to manage the early state disease which poses no systemic risks in the event of a false positive. However, fulfillment of such criteria is presently limited by the sensitivity and efficacy of conventional protocols.[2] Thus there exists a prevalent need for the development of a new methodology to satisfy the dual criteria. The work presented herein concentrates on exploiting the favorable properties of calcium phosphate-based nanoparticulate systems, in combination with the bifunctionality of indocyanine green, to render an effective composite theranostic modality for the simultaneous NIR diagnostic imaging and localized photodynamic therapy of early stage cancers.

## 1.6 Chapter Summaries

A calcium phosphate-based nanoparticulate vector is proposed to effectively serve as a model theranostic agent for the simultaneous detection and treatment of early stage disease. Encapsulating the NIR fluorophore ICG within the nanoparticle is anticipated to overcome the present limitations of deep tissue diagnostic imaging. Analogous to the optical enhancements afforded by encapsulation schemes involving silica and polymeric nanoparticles, the composite fluorescent unit is expected to have a strong detectable signal that is stable over an extended lifetime for long term imaging protocols. The matrix shielding will impart a defense against susceptibility to photo- and biological-degradation, as well as mitigate against solvatochromic influences, permitting consistent imaging in a variety of physiological environments. Additionally, the calcium phosphate-based NP would be biocompatible and systemically non-toxic for safe administration, including rapid and complete clearance from biological systems after completion of their tasks to avert any long-term exposure effects.

Likewise, the composite ICG-calcium phosphate nanoparticle has the potential to serve as a therapeutic agent in a photodynamic modality for a localized and moderate therapy ideal for early stage cancer. This function is imparted by the photoactivation of the component ICG molecule, which doubles as a photosensitizer. It is proposed that encapsulation of the ICG will render the composite unit photoactive, initiating a controlled photodynamic reaction for therapeutic manipulation.

Thus, by exploiting the distinct characteristics of the two component system, the biocompatibility of the calcium phosphate-based nano-carrier, and the dual capacity of ICG for NIR imaging and generating a therapeutic response, the dye-doped nanoparticle is projected to function as bifunctional theranostic agent for simultaneous detection and treatment schemes.

Chapter Two will outline the templated synthesis of calcium phosphosilicate nanoparticles (CPSNP). The reverse micelle approach provides the means for surface functionalization and encapsulation of the fluorescent photosensitizer, unique features of this work that have not been realized by other calcium phosphate precipitation and delivery efforts to date. The chapter will also discuss colloidal characteristics of the composite agents, including size, dispersion, chemical composition, and encapsulation yield.

Chapter Three evaluates these composite fluorescent probes as the imaging element in the diagnostic imaging portion of the proposed theranostic modality. Specifically, the optical performance is compared to the constituent free fluorophore, with particular emphasis on fluorescence intensity, stability, and yield, factors of particular interest to long time diagnostic screening applications.

Chapter Four addresses the primary physical shortcomings of ICG in physiological environments, particularly the rapid protein binding and premature clearance from circulation, as well as the absence of target selectivity. Comparative evaluation of the ICG-CPSNPs will be

conducted through *in vivo* distribution and imaging experiments, in an effort to highlight to improvements afforded by the encapsulation.

Chapter Five evaluates the capacity of ICG-CPSNPs to generate reactive singlet oxygen through a photodynamic process. A qualitative *ex situ* evaluation will compare the therapeutic capacity of these composite nanoparticles to the free photosensitizer, in an appraisal of their utility as a photosensitizer for therapeutic applications.

Chapter Six presents *in vitro* and *in vivo* evaluation of the therapeutic faculty of ICG-CPSNPs via photodynamic experiments as the final validation of the bifunctionality of these vectors.

Chapter Seven concludes the discussion and evaluates the overall performance of these composite ICG-CPSNPs as an effective theranostic agent to simultaneously function as a sensitive, deep tissue diagnostic imaging agent, as well as a controlled, therapeutic photosensitizer. Suggestions are offered for improvement of the composite nanoplatform based on observations from the current work.

## 1.7 References


1. Bornhop, D. J.; Contag, C. H.; Licha, K.; Murphy, C. J. Advances in Contrast Agents, Reporters, and Detection. *J. Biomed. Opt.* **2001,** *6*, 106-110.
2. Wulfkuhle, J. D.; Liotta, L. A.; Petricoin, E. F. Proteomic Applications for the Early Detection of Cancer. *Nature Reviews Cancer* **2003,** *3*, 267-275.
3. He, X.; Wang, K.; Cheng, Z. In Vivo near-Infrared Fluorescence Imaging of Cancer with Nanoparticle-Based Probes. *Wiley Interdisciplinary Reviews: Nanomedicine and Nanobiotechnology* **2010,** *published on-line*.
4. *Cancer Facts & Figures 2009*; American Cancer Society: Atlanta, 2009.
5. Albert, U.-S.; Altland, H.; Duda, V. F.; Engel, J.; Geraedts, M.; Heywang-Köbrunner, S. H.; Hölzel, D.; Kalbheim, E.; Koller, M.; König, K., *et al.* Early Detection of Breast Cancer in Germany. Guideline 2008. *Der Onkologe* **2008,** *14*, 461-477.
6. Fishman, D. A.; Cohen, L.; Blank, S. V.; Shulman, L.; Singh, D.; Bozorgi, K.; Tamura, R.; Timor-Tritsch, I.; Schwartz, P. E. The Role of Ultrasound Evauation in the Detection of Early-Stage Epithelial Ovarian Cancer. *American Journal of Obstetrics and Gynecology* **2005,** *192*, 1214-1222.

7. Morawski, A. M.; Lanza, G. A.; Wickline, S. A. Targeted Contrast Agents for Magnetic Resonance Imaging and Ultrasound. *Curr. Opin. Biotech.* **2005,** *16*, 89-92.
8. Loo, C.; Lowery, A.; Halas, N.; West, J.; Drezek, R. Immunotargeted Nanoshells for Integrated Cancer Imaging and Therapy. *Nano Lett.* **2005,** *5*, (4), 709-711.
9. Lin, A. W. H.; Lewinski, N. A.; West, J. L.; Halas, N. J.; Drezek, R. A. Optically Tunable Nanoparticle Contrast Agents for Early Cancer Detection: Model-Based Analysis of Gold Nanoshells. *J. Biomed. Opt.* **2005,** *10*, (6).
10. Healthwise; Incorporated, Stages of Prostate Cacer. In http://www.healthwise.com/, Ed. Boise, ID, 2009.
11. Holm, B. A.; Bergey, E. J.; De, T.; Rodman, D. J.; Kapor, R.; Levy, L.; Friend, C. S.; Prasad, P. N. Nanotechnology in Biomedical Applications *Molecular Crystal and Liquid Crystals* **2002,** *374*, 589-598.
12. von Burstin, J.; Eser, S.; Seidler, B.; Meining, A.; Bajbouj, M.; Mages, J.; Lang, R.; Kind, A. J.; Schieke, A. E.; Schmid, R. M., *et al.* Highly Sensitive Detection of Early-Stage Pancreatic Cancer by Multimodal near-Infrared Molecular Imaging in Living Mice. *International Journal of Cancer* **2008,** *123*, 2138-2147.
13. Moin, K.; McIntyre, O. J.; Matrisian, L. M.; Sloane, B. F., Fluorescent Imaging of Tumors. In *Cancer Drug Discovery and Development: In Vivo Imaging of Cancer Therapy*, Shields, A. F.; Price, P., Eds. Humana Press Inc.: Totowa, NJ, pp 281-302.
14. Hirsch, L. R.; Gobin, A. M.; Lowery, A. R.; Tam, F.; Drezek, R. A.; Halas, N. J.; West, J. L. Metal Nanoshells. *Annals of Biomedical Engineering* **2006,** *34*, (1), 15-22.
15. Sun, C.; Yang, J.; Li, L.; Wu, X.; Liu, Y.; Liu, S. Advances in the Study of Luminescence Probes for Proteins. *Journal of Chromatography B* **2004,** *803*, 173-190.
16. Stefflova, K.; Chen, J.; Zheng, G. Using Molecular Beacons for Cancer Imaging and Treatment. *Frontiers in Bioscience* **2007,** *12*, 4709-4721.
17. Weissleder, R. A Clearer Vision for in Vivo Imaging. *Nat. Biotechnol.* **2001,** *19*, 316-317.
18. Sevick-Muraca, E. M.; Houston, J. P.; Gurfinkel, M. Fluorescence-Enhanced, near Infrared Diagnostic Imaging with Contrast Agents. *Curr. Opin. Chem. Biol.* **2002,** *6*, (5), 642-650.
19. Prasad, P. N., *Introduction to Biophotonics*. John Wiley & Sons, Inc.: Hoboken, NJ, 2003.
20. Patonay, G.; Strekowski, L.; Raszkiewicz, A.; Kim, J. S. Near-Infrared Probes: Design and Applications. *Proceedings of SPIE* **2008,** *6097*, 6097091-6097099.
21. Hamblin, M. R.; Demidova, T. N., Mechanisms of Low Level Light Therapy. In *Mechanisms for Low-Light Therapy*, Hamblin, M. R.; Waynant, R. W.; Anders, J., Eds. SPIE: Bellingham, WA, 2006; Vol. 6140, pp 614001-614013.
22. Malicka, J.; Gryczynski, I.; Geddes, C. D.; Lakowicz, J. R. Metal-Enhanced Emission from Indocyanine Green: A New Approach to in Vivo Imaging. *J. Biomed. Opt.* **2003,** *8*, (3), 472-478.
23. Benson, R. C.; Kues, H. A. Fluorescence Properties of Indocyanine Green as Related to Angiography. *Phys. Med. Biol.* **1978,** *23*, (1), 159.
24. Yu, J.; Yaseen, M. A.; Anvari, B.; Wong, M. S. Synthesis of near-Infrared-Absorbing Nanoparticle-Assembled Capsules. *Chem. Mater.* **2007,** *19*, (6), 1277-1284.
25. Landsman, M. L. J.; Kwant, G.; Mook, G. A.; Zijlstra, W. G. Light-Absorbing Properties, Stability, and Spectral Stabilization of Indocyanine Green. *J. Appl. Physiol.* **1976,** *40*, (4), 575-583.

26. Taichamn, G. C.; Hendry, P. J.; Wilbert, J. K. The Use of Cardio-Green for Intraoperative Vizualization of the Coronary Circulation: Evaluation of Myocardial Toxicity. *Tex. Heart I. J.* **1987,** *14*, 133-138.
27. Schutt, F.; Fischer, J.; Kopitz, J.; Holz, F. G. Indocyanine Green Angiography in the Presence of Subretinal or Intraretinal Haemorrhages: Clinical and Experimental Investigations. *Clin. Exp. Ophthalmol.* **2002,** *30*, (2), 110-114.
28. Motomura, K.; Inaji, H.; Komoike, Y.; Kasugai, I.; Noguchi, S.; Koyama, H. Sentinel Node Biopsy Guided by Indocyanine Green Dye in Breast Cancer Patients. *Jpn. J. Clin. Oncol.* **1999,** *29*, (12), 604-607.
29. Ishihara, H.; Okawa, H.; Iwakawa, T.; Umegaki, N.; Tsubo, T.; Matsuki, A. Does Indocyanine Green Accurately Measure Plasma Volume Early after Cardiac Surgery? *Anesth. Analg.* **2002,** *94*, (4), 781-786.
30. Ott, P. Hepatic Elimination of Indocyanine Green with Special Reference to Distribution Kinetics and the Influence of Plasma Protein Binding. *Pharmacol. Toxicol.* **1998,** *82*, 1-48.
31. Paumgartner, G.; Probst, P.; Kraines, R.; Leevy, C. M. Kinetics of Indocyanine Green Removal from the Blood. *Ann. NY Acad. Sci.* **1970,** *170*, 134-147.
32. Caesar, J.; Shaldon, S.; Chiandussi, L.; Guevara, L.; Sherlock, S. The Use of Indocyanine Green in the Measurement of Hepatic Blood Flow and as a Test of Hepatic Function. *Clin. Sci.* **1961,** *21*, 43-57.
33. Frangioni, J. V. In Vivo near-Infrared Fluorescence Imaging. *Curr. Opin. Chem. Biol.* **2003,** *7*, (5), 626-634.
34. Olsen, T. W.; Lim, J. I.; Capone, A.; Myles, R. A.; Gilman, J. P. Anaphylactic Shock Following Indocyanine Green Angiography. *Arch. Ophthalmol.-Chic.* **1996,** *114*, 97.
35. Philip, R.; Penzkofer, A.; Baumler, W.; Szeimies, R. M.; Abels, C. Absorption and Fluorescence Spectroscopic Investigation of Indocyanine Green. *J. Photoch. Photobio. A* **1996,** *96*, 137-148.
36. Soper, S. A.; Mattingly, Q. L. Steady-State and Picosecond Laser Fluorescence Studies of Nonradiative Pathways in Tricarbocyanine Dyes: Implications to the Design of near-Ir Fluorochromes with High Fluorescence Efficiencies. *J. Am. Ceram. Soc.* **1994,** *116*, 3744-3752.
37. Lakowicz, J. R., *Principles of Fluorescence Spectroscopy*. 3rd ed.; Springer: Baltimore, MD, 2006.
38. Yan, J.; Estevez, C.; Smith, J.; Wang, K.; He, X.; Wang, L.; Tan, W. Dye-Doped Nanoparticles for Bioanalysis. *Nano Today* **2007,** *2*, (3), 44-50.
39. Desmettre, T.; Devoisselle, J. M.; Mordon, S. Fluorescence Properties and Metabolic Features of Indocyanine Green (Icg) as Related to Angiography. *Surv. Ophthalmol.* **2000,** *45*, (1), 15-27.
40. Simmons, R.; Shephard, R. J. Does Indocyanine Green Obey Beer's Law? *J. Appl. Physiol.* **1971,** *30*, (4), 502-507.
41. Gathje, J.; Steuer, R. R.; Nicholes, K. R. K. Stability Studies on Indocyanine Green Dye. *J. Appl. Physiol.* **1970,** *29*, (2), 181-185.
42. Holzer, W.; Mauerer, M.; Penzkofer, A.; Szeimies, R. M.; Abels, C.; Landthaler, M.; Baumler, W. Photostability and Thermal Stability of Indocyanine Green. *J. Photoch. Photobio. B* **1998,** *47*, (2-3), 155-164.
43. Mordon, S.; Devoisselle, J. M.; Soulie-Begu, S.; Desmettre, T. Indocyanine Green: Physicochemical Factors Affecting Its Fluorescence in Vivo. *Microvasc. Res.* **1998,** *55*, (2), 146-152.

44. Maarek, J. M. I.; Holschneider, D. P.; Harimoto, J. Fluorescence of Indocyanine Green in Blood: Intensity Dependence on Concentration and Stabilization with Sodium Polyaspartate. *J. Photoch. Photobio. B* **2001,** *65*, (2-3), 157-164.
45. Zhang, Y.; Wang, M. The Luminescent Properties and Photo-Decay of Sulfosalicylic Acid Doped Ormosils. *Mater. Lett.* **2000,** *42*, 86-91.
46. Saxena, V.; Sadoqi, M.; Shao, J. Degradation Kinetics of Indocyanine Green in Aqueous Solution. *J. Pharm. Sci.* **2003,** *92*, (10), 2090-2097.
47. Muckle, T. J. Plasma Proteins Binding of Indocyanine Green. *Biochem. Med.* **1976,** *15*, (1), 17-21.
48. Santra, S.; Dutta, D., *Nanomaterials for Cancer Diagnosis*. Wiley-VCH Verlag GmbH &Co.: Weinheim, 2007; Vol. 7.
49. Lee, H.; Lee, K.; Kim, I. K.; Park, T. G. Synthesis, Characterization, and in Vivo Diagnostic Applications of Hyaluronic Acid Immobilized Gold Nanoparticles. *Biomaterials* **2008,** *29*, 4709-4718.
50. Bulte, J. W. M.; Modo, M. M. J., Cancer Drug Discovery and Development: In Vivo Imaging of Cancer Therapy. In Shields, A. F.; Price, P., Eds. Humana Press Inc.: Totowa, NJ.
51. West, J. L.; Halas, N. J. Engineered Nanomaterials for Biophotonics Applications: Improving Sensing, Imaging, and Therapeutics. *Annual Review of Biomedical Engineering* **2003,** *5*, (1), 285-292.
52. Leatherdale, C. A.; Woo, W.-K.; Mikulec, F. V.; Bawendi, M. G. On the Absorption Cross Section of Cdse Nanocrystal Quantum Dots. *J. Phys. Chem. B* **2002,** *106*, (31), 7619-7622.
53. Smithpeter, C.; Dunn, A. K.; Drezek, R.; Collier, T.; Richards-Kortum, R. Near Real Time Confocal Microscopy of Cultured Amelanotic Cells: Sources of Signal, Contrast Agents and Limits of Contrast. *Journal of Biomedical Optics* **1998,** *3*, (4), 429-436.
54. Dabbousi, B. O.; Rodriguez-Viejo, J.; Mikulec, F. V.; Heine, J. R.; Mattoussi, H.; Ober, R.; Jensen, K. F.; Bawendi, M. G. (Cdse)Zns Core-Shell Quantum Dots: Synthesis and Characterization of a Size Series of Highly Luminescent Nanocrystallites. *J. Phys. Chem. B* **1997,** *101*, (46), 9463-9475.
55. Chan, W. C. W.; Nie, S. M. Quantum Dot Bioconjugates for Ultrasensitive Nonisotopic Detection. *Science* **1998,** *281*, (5385), 2016-2018.
56. Cai, W.; Hsu, A. R.; Li, Z.; Chen, X. Are Quantum Dots Ready for in Vivo Imaging in Human Subjects? *Nanoscale Research Letters* **2007,** *2*, 265-281.
57. Michalet, X.; Pinaud, F.; Lacoste, T. D.; Dahan, M.; Bruchez, M.; Alivisatos, A. P.; Weiss, S. Properties of Fluorescent Semiconductor Nanocrystals and Their Application to Biological Labeling. *Single Molecules* **2001,** *2*, (4), 261-276.
58. Hatami, F.; Grundmann, M.; Ledentsov, N. N.; Heinrichsdorff, F.; Heitz, R.; Bo¨hrer, J.; Bimberg, D. Carrier Dynamics in Type-Ii Gasb/Gaas Quantum Dots. *Physical Review B* **1998,** *57*, (8), 4635-4641.
59. Youn, H. C.; Baral, S.; Fendler, J. H. Dihexadecyl Phosphate, Vesicle-Stabilized and in Situ Generated Mixed Cadmium Sulfide and Zinc Sulfide Semiconductor Particles: Preparation and Utilization for Photosensitized Charge Separation and Hydrogen Generation. *J. Phys. Chem.-US* **1998,** *92*, (22), 6320-6327.
60. Kim, S.; Fisher, B.; Eisler, H. J.; Bawendi, M. Type-Ii Quantum Dots: Cdte/Cdse(Core/Shell) and Cdse/Znte(Core/Shell) Heterostructures. *J. Am. Chem. Soc.* **2003,** *125*, (38), 11466-11467.
61. Bailey, R. E.; Smith, A. M.; Nie, S. M. Quantum Dots in Biology and Medicine. *Physica E-Low-Dimensional Systems & Nanostructures* **2004,** *25*, (1), 1-12.

62. Guo, G.; Liu, W.; Liang, J.; He, Z.; Xu, H.; Yang, X. Probing the Cytotoxicity of Cdse Quantum Dots with Surface Modification. *Mater. Lett.* **2007,** *61*, 1641-1644.
63. Kloepfer, J. A.; Bradforth, S. E.; Nadeau, J. L. Photophysical Properties of Biologically Compatible Cdse Quantum Dot Structures. *J. Phys. Chem. B* **2005,** *109*, (20), 9996-10003.
64. Zhang, Y.; Zhang, H.; Ma, M.; Guo, X.; Wang, H. The Influence of Ligands on the Preparation and Optical Properties of Water-Soluble Cdte Quantum Dots. *Applied Surface Science* **2009,** *255*, 4747-4753.
65. Kim, S.; Lim, Y. T.; Soltesz, E. G.; De Grand, A. M.; Lee, J.; Nakayama, A.; Parker, J. A.; Mihaljevic, T.; Laurence, R. G.; Dor, D. M., *et al.* Near-Infrared Fluorescent Type Ii Quantum Dots for Sentinel Lymph Node Mapping. *Nat. Biotechnol.* **2004,** *22*, (1), 93-97.
66. Jaiswal, J. K.; Simon, S. M. Potentials and Pitfalls of Fluorescent Quantum Dots for Biological Imaging. *trends in Cell Biology* **2004,** *14*, (9), 497-504.
67. Lovrić, J.; Bazzi, H. S.; Cuie, Y.; Fortin, G. R. A.; Winnik, F. M.; Maysinger, D. Differences in Subcellular Distribution and Toxicity of Green and Red Emitting Cdte Quantum Dots. *J. Mol. Med.* **2005,** *83*, 377-385.
68. Lovrić, J.; Cho, S. J.; Winnik, F. M.; Maysinger, D. Unmodified Cadmium Telluride Quantum Dots Induce Reactive Oxygen Species Formation Leading to Multiple Organelle Damage and Cell Death. *Chemistry & Biology* **2005,** *12*, (11), 1227-1234.
69. Hoshino, A.; Fujioka, K.; Oku, T.; Suga, M.; Sasaki, Y. F.; Ohta, T.; Yasuhara, M.; Suzuki, K.; Yamamoto, K. Physicochemical Properties and Cellular Toxicity of Nanocrystal Quantum Dots Depend on Their Surface Modification. *Nano Lett.* **2004,** *4*, (11), 2163-2169.
70. Ballou, B.; Lagerholm, B. C.; Ernst, L. A.; Bruchez, M. P.; Waggoner, A. S. Noninvasive Imaging of Quantum Dots in Mice. *Bioconjugate Chem.* **2004,** *15*, (1), 79-86.
71. Dubertret, B.; Skourides, P.; Norris, D. J.; Noireaux, V.; Brivanlou, A. H.; Libchaber, A. In Vivo Imaging of Quantum Dots Encapsulated in Phospholipid Micelles. *Science* **2002,** *298*, 1759- 1762.
72. Derfus, A. M.; Chan, W. C. W.; Bhatia, S. N. Probing the Cytotoxicity of Semiconductor Quantum Dots. *Nano Lett.* **2004,** *4*, (1), 11-18.
73. Chang, E.; Thekkek, N.; Yu, W. W.; Colvin, V. L.; Drezek, R. Evaluation of Quantum Dot Cytotoxicity Based on Intracellular Uptake. *Small* **2006,** *2*, (12), 1412-1417.
74. Kirchner, C.; Liedl, T.; Kudera, S.; Pellegrino, T.; Javier, A. M.; Guab, H. E.; Stölze, S.; Fertig, N.; Parak, W. J. Cytotoxicity of Colloidal Cdse and Cdse/Zns Nanoparticles. *Nano Lett.* **2005,** *5*, (2), 331-338.
75. Ryman-Rasmussen, J. P.; Riviere, J. E.; Monteiro-Riviere, N. A. Surface Coatings Determine Cytotoxicity and Irritation Potential of Quantum Dot Nanoparticles in Epidermal Keratinocytes. *Journal of Investigative Dermatology* **2007,** *127*, (1), 143-153.
76. Hardman, R. A Toxicologic Review of Quantum Dots: Toxicity Depends on Physiochemical and Environmental Factos. *Environ. Health Persp.* **2006,** *114*, (2), 165-172.
77. Cho, S. J.; Maysinger, D.; Jain, M.; Roder, B.; Hackbarth, S.; Winnik, F. M. Long-Term Exposure to Cdte Quantum Dots Causes Functional Impairments in Live Cells. *Langmuir* **2007**.
78. Smith, A. M.; Duan, H.; Rhyner, M. N.; Ruan, G.; Nie, S. M. A Systematic Examination of Surface Coatings on the Optical and Chemical Properties of Semiconductor Quantum Dots. *Physical Chemistry Chemical Physics* **2006,** *8*, 3895-3903.
79. Panyam, J.; Labhasetwar, V. Biodegradable Nanoparticles for Drug and Gene Delivery to Cells and Tissue. *Advanced Drug Delivery Reviews* **2003,** *55*, (3), 329-347.

80. Tycko, B.; Maxfield, F. R. Rapid Acidification of Endocytic Vesicles Containing A2-Macroglobulin. *Cell* **1982,** *28*, 643-651.
81. Stubbs, M.; McSheehy, P. M. J.; Griffiths, J. R.; Bashford, C. L. Causes and Consequences of Tumor Acidity and Implications for Treatment. *Molecular Medicine Today* **2000,** *6*, 15-19.
82. Mancini, M. C.; Kairdolf, B. A.; Smith, A. M.; Nie, S. M. Oxidative Quenching and Degradation of Polymer-Encapsulated Quantum Dots: New Insights into the Long-Term Fate and Toxicity of Nanocrystals in Vivo. *Journal of the American Ceramic Society* **2008,** *130*, 10836-10837.
83. Mohs, A. M.; Duan, H.; Kairdolf, B. A.; Smith, A. M.; Nie, S. M. Proton-Resitstant Quantum Dots: Stability Is Gastrointestinal Fluids and Implications for Oral Delivery of Nanoparticle Agents. *Nano Research* **2009,** *2*, 500-508.
84. Zhang, Y.; He, J.; Wang, P.; Chen, J.; Lu, Z.; Lu, D.; Guo, J.; Wang, C.; Yang, W. Time-Dependent Photoluminescence Blue Shift of the Quantum Dots in Living Cells: Effect of Oxidation by Singlet Oxygen. *J. Am. Ceram. Soc.* **2006,** *128*, (41), 13396-13401.
85. Aldana, J.; Lavelle, N.; Wang, Y.; Peng, X. Size-Dependent Dissociation Ph of Thiolate Ligands from Cadmium Chalcogenide Nanocrystals. *J. Am. Ceram. Soc.* **2005,** *127*, 2496-2504.
86. Hanaki, K.-i.; Momo, A.; Oku, T.; Komoto, A.; Maenosono, S.; Yamaguchi, Y.; Yamamoto, K. Semiconductor Quantum Dot/Albumin Complex Is a Long-Life and Highly Photostable Endosome Marker. *Biochemical and Biophysical Research Communications* **2003,** *302*, (3), 496-501.
87. Jaiswal, J. K.; Mattoussi, H.; Mauro, J. M.; Simon, S. M. Long-Term Multiple Color Imaging of Live Cells Using Quantum Dot Bioconjugates. *Nat. Biotechnol.* **2003,** *21*, 47-51.
88. Voura, E. B.; Jaiswal, J. K.; Mattoussi, H.; Simon, S. M. Tracking Metastatic Tumor Cell Extravasation with Quantum Dot Nanocrystals and Fluorescence Emission Scanning Microscopy. *Nature Medicine* **2004,** *10*, 993-998.
89. Shiohara, A.; Hoshino, A.; Hanaki, K.-i.; Suzuki, K.; Yamamoto, K. On the Cyto-Toxicity Caused by Quantum Dots. *Microbiology and Immunology* **2004,** *48*, (9), 669-675.
90. Biju, V.; Itoh, T.; Anas, A.; Sujith, A.; Ishikawa, M. Semiconductor Quantum Dots and Metal Nanoparticles: Synthesis, Optical Properties, and Biological Applications. *Anal Bioanal Chem* **2008,** *391*, 2467-2495.
91. Averitt, R. D.; Westcott, S. L.; Halas, N. J. Linear Optical Properties of Gold Nanoshells. *Journal of the Optical Society of America B* **1999,** *16*, 1824-1832.
92. Oldenburg, S. J.; Averitt, R. D.; Westcott, S. L.; Halas, N. J. Nanoengineering of Optical Resonances. *Chemical Physics Letters* **1998,** *188*, 243-247.
93. Oldenburg, S. J.; Jackson, J. B.; Westcott, S. L.; Halas, N. J. Infrared Extinction Properties of Gold Nanoshells. *Applied Physics Letters* **1999,** *75*, (19), 2897-2899.
94. Lal, S.; Clare, S. E.; Halas, N. J. Nanoshell-Enabled Photothermal Cancer Therpay: Impending Clinical Impact. *Accounts of Chemical Research* **2008,** *41*, (12), 1842-1851.
95. Wang, Y.; Xia, X.; Wang, X.; Ku, G.; Gill, K. L.; O'Neal, D. P.; Stoica, G.; Wang, L. V. Photoacoustic Tomography of a Nanoshell Contrast Agent in the in Vivo Rat Brain. *Nano Lett.* **2004,** *4*, (9), 1689-1692.
96. Murphy, C. J.; Gole, A. M.; Stone, J. W.; Sisco, P. N.; Alkilany, A. M.; Goldsmith, E. C.; Baxter, S. C. Gold Nanoparticles in Biology: Beyond Toxicity to Cellular Imaging. *Accounts of Chemical Research* **2008,** *41*, (12), 1721-1730.

97. James, W. D.; Hirsch, L. R.; West, J. L.; O'Neal, P. D.; Payne, J. D. Application of Inaa to the Build-up and Clearance of Gold Nanoshells in Clinical Studies in Mice. *J. Radioanal. Nucl. Ch.* **2007,** *271*, (2), 455-459.
98. De Jong, W. H.; Hagens, W. I.; Krystek, P.; Burger, M. C.; Sips, A. J. A. M.; Geertsma, R. E. Particle Size-Dependent Organ Distribution of Gold Nanoparticles after Intravenous Administration. *Biomaterials* **2008,** *29*, 1912-1919.
99. Hasan, W.; Stender, C. L.; Lee, M. H.; Nehl, C. L.; Lee, J.; Odom, T. W. Tailoring the Structure of Nanopyramids for Optimal Heat Generation. *Nano Letters* **2009,** *9*, (4), 1555-1558.
100. Huang, X.; Jain, P. K.; El-Sayed, I. H.; El-Sayed, M. A. Plasmonic Photothermal Therapy (Pptt) Using Gold Nanoparticles. *Lasers in Medical Science* **2008,** *23*, 217-228.
101. Yang, W.-L.; Nair, D. G.; Makizumi, R.; Gallons, G.; Ye, X.; Sharma, R. R.; Ravikumar, T. S. Heat Shock Protein 70 Is Induced in Mouse Human Colon Xenografts after Sublethal Radiofrequency Ablation. *Annals of Surgical Oncology* **2004,** *11*, (4), 399-406.
102. Ow, H.; Larson, D. R.; Srivastava, M.; Baird, B. A.; Webb, W. W.; Wiesner, U. Bright and Stable Core-Shell Fluorescent Silica Nanoparticles. *Nano Lett.* **2005,** *5*, (1), 113-117.
103. Avnir, D.; Levy, D.; Reisfeld, R. The Nature of the Silica Cage as Reflected by Spectral Changes and Enhanced Photostability of Trapped Rhodamine 6g. *J. Phys. Chem.-US* **1984,** *88*, (24), 5956-5959.
104. Altınoğlu, E. İ.; Russin, J. T.; Kaiser, J. M.; Barth, B. M.; Eklund, P. C.; Kester, M.; Adair, J. H. Near-Infrared Emitting Fluorophore-Doped Calcium Phosphate Nanoparticles for in Vivo Imaging of Human Breast Cancer. *ACS Nano* **2008,** *2*, (10), 2075-2084.
105. Muddana, H. S.; Morgan, T. T.; Adair, J. H.; Butler, P. J. Photophysics of Cy3-Encapsulated Calcium Phosphate Nanoparticles. *Nano Lett.* **2009,** *9*, (4), 1559-1566.
106. Devoisselle, J. M.; Soulie-Begu, S.; Mordon, S.; Desmettre, T.; Maillols, H. A Preliminary Study of the in Vivo Behaviour of an Emulsion Formulation of Indocyanine Green. *Laser. Med. Sci.* **1998,** *13*, (4), 279-282.
107. Rao, J.; Dragulescu-Andrasi, A.; Yao, H. Fluorescence Imaging in Vivo: Recent Advances. *Curr. Opin. Biotech.* **2007,** *18*, 17-25.
108. Zhao, X.; Bagwe, R. P.; Tan, W. Development of Organic-Dye-Doped Silica Nanoparticles in a Reverse Microemulsion. *Adv. Mater.* **2004,** *16*, (2), 173-176.
109. Zhou, X.; Zhou, J. Improving the Signal Sensitivity and Photostability of DNA Hybridizations on Microarrays by Using Dye-Doped Core-Shell Silica Nanoparticles. *Anal. Chem.* **2004,** *76*, 5302-5312.
110. Bele, M.; Siiman, O.; Matijevic, E. Preparation and Flow Cytometry of Uniform Silica-Fluorescent Dye Microspheres. *J. Colloid Interf. Sci.* **2002,** *254*, 274–282.
111. Morgan, T. T.; Muddana, H. S.; Altınoğlu, E. İ.; Rouse, S. M.; Tabaković, A.; Tabouillot, T.; Russin, T. J.; Shanmugavelandy, S. S.; Butler, P. J.; Eklund, P. C., *et al.* Encapsulation of Organic Molecules in Calcium Phosphate Nanocomposite Particles for Intracellular Imaging and Drug Delivery. *Nano Lett.* **2008,** *8*, (12), 4108-4115.
112. Fubini, B.; Hubbard, A. Reactive Oxygen Species (Ros) and Reactive Nitrogen Species (Rns) Generation by Silica in Inflammation and Fibrosis. *Free Radical Biology and Medicine* **2003,** *34*, (12), 1507-1516.
113. Burns, A.; Sengupta, P.; Zedayko, T.; Baird, B.; Wiesner, U. Core/Shell Fluorescent Silica Nanoparticles for Chemical Sensing: Towards Single-Particle Laboratories. *Small* **2006,** *6*, 723-726.
114. Soppimath, K. S.; Aminabhavi, T. M.; Kulkarni, A. R.; Rudzinski, W. E. Biodegradable Polymeric Nanoparticles as Drug Delivery Devices. *J. Control Release* **2001,** *70*, 1-20.

115. Saxena, V.; Sadoqi, M.; Shao, J. Indocyanine Green-Loaded Biodegradable Nanoparticles: Preparation, Physicochemical Characterization and in Vitro Release. *Int. J. Pharm.* **2004,** *278*, (2), 293-301.
116. Yaseen, M. A.; Yu, J.; Wong, S. M.; Anvari, B. Laser-Induced Heating of Dextran-Coated Mesocapsules Containing Indocyanine Green. *Biotechnol. Progr.* **2007,** *23*, (6), 1431-1440.
117. Gomes, A. J.; Lunardi, L. O.; Marchetti, J. M.; Lunardi, C. N.; Tedesco, A. C. Indocyanine Green Nanoparticles Useful for Photomedicine. *Photomed. Laser Surg.* **2006,** *24*, (4), 514-521.
118. Saxena, V.; Sadoqi, M.; Shao, J. Enhanced Photo-Stability, Thermal-Stability and Aqueous-Stability of Indocyanine Green in Polymeric Nanoparticulate Systems. *J. Photoch. Photobio. B* **2004,** *74*, (1), 29-38.
119. Singh, A.; Mukherjee, M. Effect of Polymer-Particle Interaction in Swelling Dynamics of Ultrathink Nanocomposite Films. *Macromoecules* **2005,** *38*, (21), 8795-8802.
120. Rodriguez, V. B.; Henry, S. M.; Hoffman, A. S.; Stayton, P. S.; Li, X.; Pun, S. H. Encapsulation and Stabilization of Indocyanine Green within Poly(Styrene-Alt-Maleic Anhydride) Block-Poly(Styrene) Micelles for near-Infrared Imaging. *J. Biomed. Opt.* **2008,** *13*, (1), 14025-1 - 14025-10.
121. Kim, G.; Huang, S.; Day, K. C.; O'Donnell, M.; Agayan, R. R.; Day, M. A.; Kopelman, R.; Ashkenazi, S. Indocyanine-Green-Embedded Pebbles as a Contrast Agent for Photoacoustic Imaging. *J. Biomed. Opt.* **2007,** *12*, (4).
122. Goldberg, M.; Langer, R.; Jia, X. Nanostructured Materials for Applications in Drug Delivery and Tissue Engineering. *J. Biomat. Sco.-Polym. E.* **2007,** *18*, (3), 241-268.
123. Gao, H.; Shi, W.; Freund, L. B. Mechanics of Receptor-Mediated Endocytosis. *Proc. Natl. Acad. Sci. USA* **2005,** *102*, (27), 9469-9474.
124. Dorozhkin, S. V.; Epple, M. Biological and Medical Significance of Calcium Phosphates. *Angew. Chem. Int. Edit.* **2002,** *41*, (17), 3130-3146.
125. Weber, J. N.; White, E. W.; Lebiedzik, J. New Porous Biomaterials Replication of Echinoderm Skeletal Microstructures. *Nature* **1971,** *233*, (5318), 337-339.
126. Dubok, V. A. Bioceramics - Yesterday, Today, Tomorrow. *Powder Metall. Met. C.* **2000,** *39*, (7-8), 381-394.
127. Chiroff, R. T.; White, R. A.; White, E. W.; Weber, J. N.; Roy, D. M. The Restoration of Articular Surfaces Overlying Porous Biomaterials. *J. Biomed. Mater. Res.* **1977,** *11*, (2), 165-178.
128. He, Q.; Mitchell, A. R.; Johnson, S. L.; Wagner-Bartak, C.; Morcol, T.; Bell, S. J. D. Calcium Phosphate Nanoparticle Adjuvant. *Clin. Diagn. Lab. Immunol.* **2000,** *7*, (6), 899-903.
129. Jeng, H. A.; Swanson, J. Toxicity of Metal Oxide Nanoparticles in Mammalian Cells. *J. Environ. Sci. Heal. A* **2006,** *41*, (12), 2699-2711.
130. Jin, S.; Ye, K. Nanoparticle-Mediated Drug Delivery and Gene Therapy. *Biotechnol. Progr.* **2006,** *23*, (1), 32-41.
131. Tung, M. S., Calcium Phosphates: Structure, Composition, Solubility and Stability. In *Calcium Phosphates in Biological and Industrial Systems*, Amjad, Z., Ed. Kluwer Academic Publishers: Boston, 1998; pp 1-19.
132. Oyane, A.; Kim, H.; Furuya, T.; Kobuko, T.; Miyazaki, T.; Nakamura, T. Preparation and Assessment of Revised Simulated Body Fluids. *J. Biomed. Mater. Res. A* **2002,** *65A*, (2), 188-195.

133. Tseng, W. W.; Saxton, R. E.; Deganutti, A.; Liu, C. D. Infrared Laser Activation of Indocyanine Green Inhibits Growth in Human Pancreatic Cancer. *Pancreas* **2003,** *27*, (3), e42-e45.
134. Delaey, E.; van Laar, F.; De Vos, D.; Kamuhabwa, A.; Jacobs, P.; de Witte, P. A. M. A Comparative Study of the Photosensitizinf Characteristics of Some Cyanine Dyes. *Journal of Photochemistry and Photobiology B: Biology* **2000,** *55*, 27-36.
135. Bäumler, W.; Abels, C.; Karrer, S.; Weiß, T.; Messmann, H.; Landthaler, M.; Szeimies, R.-M. Photo-Oxidative Killing of Human Colonic Cancer Cells Using Indocyanine Green and Infrared Light. *British Journal of Cancer* **1999,** *80*, 360-363.
136. Agdeppa, E. D.; Spilker, M. E. A Review of Imaging Agent Development. *American Association of Pharmaceutical Scientists Journal* **2009,** *11*, 286-299.
137. Cheng, S.-H.; Lee, C.-H.; Yang, C.-S.; Tseng, F.-G.; Mou, C.-Y.; Lo, L.-W. Mesoporous Silica Nanoparticles Functionalized with an Oxygen-Sensing Probe for Cell Photodynamic Therapy: Potential Cancer Theranostics. *Journal of Materials Chemistry* **2009,** *19*, 1252-1257.

# Chapter 2

## Synthesis and Laundering of Calcium Phosphosilicate Nanoparticles (CPSNPs) for Encapsulation of Indocyanine Green

Due to the advantages associated with the biocompatibility[1-3] and low immune response[4, 5] of calcium phosphates (CP), many efforts have reported preparations of this bioceramic as particulates for nontoxic and efficient transport of bioactive agents.[6-11] A wide variety of calcium phosphate precipitation schemes exist,[6, 10, 12-17] varying from the controlled addition of phosphate and calcium solutions,[10, 12, 17] to the use of double microemulsions as templates for controlled particle size.[13-16] However, there are no schemes reported to date that yield colloidally stable particles with diameters under 100 nm, a significant limitation for effective physiological administration and cellular uptake. Additionally, most current delivery techniques rely on the adsorption of molecules to the particle surface, normally resulting in the premature degradation of the deliverable prior to its intended targeted release. This chapter presents a templated precipitation and laundering protocol developed for the formation of and encapsulation by calcium phosphosilicate nanoparticles (CPSNPs) with the specific objectives of internalizing the fluorophore indocyanine green (ICG) and preserving long term dispersion of sub-20 nm particulates for effective biological administration.

### 2.1 Calcium Phosphate Precipitation

The synthesis of calcium phosphate nanoparticles are conventionally performed by numerous methods including co-precipitation,[18, 19] sol-gel processing schemes,[20] pyrolysis of aerosols,[21] and hydrothermal processing routes.[22] However, the degree of success of these

techniques in preparing nanoscale and colloidally stable particle suspensions varies considerably, with the majority yielding particles of diameters well above 100 nm and suffering from rapid agglomeration.[19] Alternatively, a relatively new microemulsion approach[15, 20] has been shown to consistently and expediently deliver particle sizes in the sub-100 nm range together with a minimized degree of particle agglomeration and controlled morphology.[23, 24] This microemulsion processing technique was adopted from the successful preparation of various other nanoparticulate systems[25] including metal oxides,[26, 27] metal carbonates,[28] and silver bromides,[29] and exploits the restricting presence of an encasing nano domain as a template for ultimate size and morphology control of the precipitating particle.

### 2.1.1 Microemulsion Templating

Inverse microemulsions have attracted considerable attention as templates for the formation of nanoparticulates in view of their small, uniform water domains (5- 20 nm in diameter)[30-32] which are ideal media for the preparation of extremely fine structures.[28, 33, 34] A microemulsion is a thermodynamically stable, isotropic dispersion of two immiscible liquids stabilized by the presence of a surfactant.[35, 36] The microstructure of a microemulsion can vary depending on the composition of the system, though the self assembled water-in-oil (w/o) droplets formed at low water content are the most successfully used for preparing nanoparticles.[27, 37] Such inverse micelles serve to confine the dispersed aqueous phase within the spherical, nanometer core droplets.[38] These surfactant-stabilized cavities provide a cage like effect that can control nucleation and growth of the forming particles.

The inverse microemulsions exhibit a dynamic structure of nano-droplets which are in constant coalescence, breakdown and deformation, As such, the chemical reactions for the formation of particulates take place when individual micelles containing the desirable reactants

collide with each other, exchanging the contents of their aqueous cores. Thus, each of these reverse micelles becomes a nanosized reactor for templating nanosized solid particles.

Various efforts have precipitated calcium phosphate nanoparticles (CPNPs) in such water-in-oil microemulsions.[15, 16, 39] As an example, Lim *et al.*[15] reported the use of a cyclohexane/polyoxyethylene (5) nonylphenol ether (NP-5) and polyoxyethylene (9) nonylphenol ether (NP-9)/water ternary system for the precipitation of calcium phosphate powders. The partial phase diagram for this system at room temperature is presented in Figure 2-1. The boundary between the microemulsion region (shaded area) and the non-microemulsion region was established by a systematic titration based on the clear-turbid observation, under the assumption that transparency is due to small dispersion sizes (5-20 nm) of the aqueous phase,[40] while mixtures become more turbid as the dispersed aqueous droplets become larger in sizes (emulsion phase).

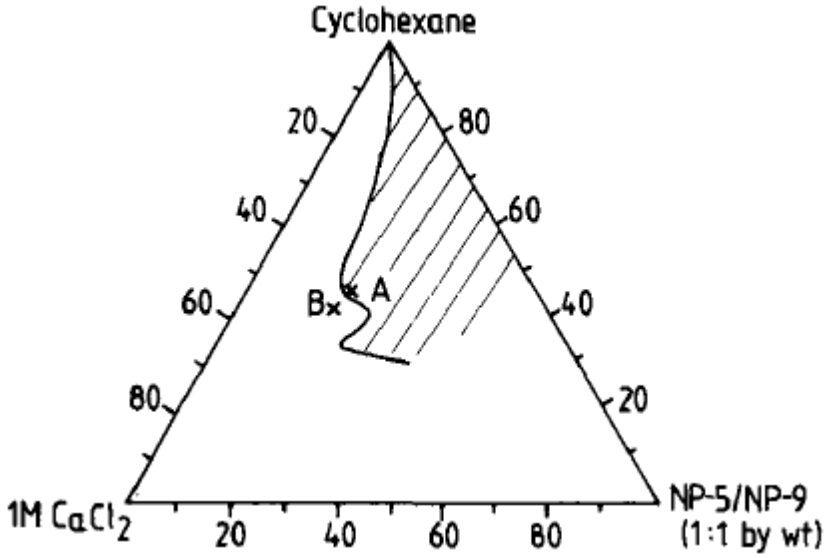


**Figure 2-1.**The partial phase diagram established for the system of cyclohexane-(NP-5 + NP-9)-aqueous solution of 1.0 M $CaCl_2$ at room temperature. The microemulsion region is marked as shaded area. The composition at point A is a microemulsion and that at point B is an emulsion. Taken from Ref. 15.

Utilizing a 45.5 wt% cyclohexane, 19.5 wt% NP-5 + NP-9, and 35 wt% aqueous phase of 1.0 M $CaCl_2$ mixture (Point A), the group were able to precipitate 5 to 10 nm diameter precursor particles within the reverse micelles.[15] Similar efforts by Singh *et al.* [41] reported the precipitation of sub-50 nm calcium phosphate nanoparticles within an inverse microemulsion. However, the stability of these nanoscaled particulate suspensions were not addressed in either report, as the solids were promptly recovered and dried for sintering and bulk processing applications.

Curiously, reports on the precipitation of CP-based nanoparticle suspensions for biological utility do not exploit the advantages afforded by micelle templated synthesis. Consequently, these efforts result in broad particle size distributions and ultimate colloidal instabilities that impair the biological utility of the vectors. A classic approach, such as that employed by Welzel *et al.*,[12] is the controlled addition of a calcium precursor to a phosphate solution. Despite reports of a primary particle size of 10-20 nm in diameter, such a bulk precipitation produces non-uniform particle sizes and offers no colloidal stability in complex solutions. Such CP particles prepared by the Epple group were reported to rapidly agglomerate and settle out of suspension upon administration to serum, thwarting the intended transfection efficacy of their vectors in physiological solution.[19]

The inadequacy of these methods highlights another shortcoming of conventional calcium phosphate nanoparticle-based delivery schemes. To date, the use of CPNPs has primarily focused on nonviral gene transfection and DNA delivery.[6, 12, 19] However, all reports undertake this function by coating the particle surface with the deliverable. While in some cases this surface adsorption provides a fortuitous steric layer and partial stability,[19] it does not afford protection from enzymatic decomposition and biological attack.[42] A more ideal scenario would be one in which the bioactive molecule being delivered, whether it be a nucleic acid, a pharmaceutical, or a molecular probe, is sheltered from premature initiation or degradation so as to extort its most efficient utility. Such shielding is provided by the internalization of the deliverable agent within

the particulate structure, as introduced in the discussion of fluorescent nanoparticles in Chapter 1. This is the architecture of preference for the calcium phosphate-based nanoparticles that will be prepared in the work presented herein.

## 2.2 Solubility and Controlled Dissolution of Calcium Phosphates

Calcium phosphates are a promising avenue for physiological deployment not only due to their bioresorbability,[43] but because they possess a unique chemistry that allows broad flexibility of the material property with respect to the intended application. The primary advantage of CP as an adjuvant for biological application is the bilateral facility by which a molecule can be encapsulated within a rigid matrix and subsequently released in a pH dependent manner. This is in contrast to attachment of deliverables to the particle surfaces, as internalization, and thus protection, does not necessarily segregate the molecules permanently; the CP particle can be designed such that the encapsulated molecules are available for use under a programmed set of environmental conditions. All calcium phosphates phases are relatively insoluble at physiological pH (pH 7.4), and have increasing solubility below pH 6.5 (Figure 2-2). This means that the particle will remain intact in the blood stream, but will dissolve and release its encapsulant in the low pH environments that are found in the body,[44] such as in solid tumors,[45] and during endocytosis.[46, 47]

Furthermore, CP is able to form a wide variety of crystalline and amorphous phases dictated primarily by the conditions under which the particles are formed.[44, 48] For the greatest degree of flexibility in the dissolution kinetics of a CPNP, an amorphous phase is ideal, as it has a comparatively higher solubility at the slightly acidic intercellular environments, as indicated by the region of the amorphous band in Figure 2-2. However, a level of integral insolubility may support the stability in physiological conditions. Thus, the calcium phosphate synthesized in this

work will incorporate a small fraction of silicate in the amorphous phase. Fortunately, CP is an easily substituted matrix, with a proven ability to incorporate both inorganic,[10, 43] and organic[6] dopants, and the inclusion of silicate is anticipated to reduce the solubility of the amorphous phase as assurance for stability in physiological pH 7.4.

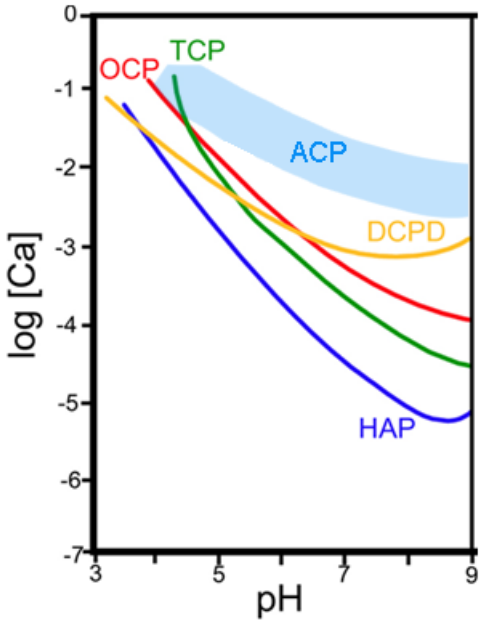


**Figure 2-2.**The solubility phase diagram for the ternary system, $Ca(OH)_2$-$H_3PO_4$-$H_2O$ at 37°C. The concentrations of calcium as a function of pH in saturated salt solutions. HAP= Hydroxyapatite [$Ca_5(PO_4)_3OH$], OCP=Octacalcium phosphate [$Ca_8H_2(PO_4)_6•5H_2O$], TCP=Tricalcium phosphate [$Ca_3(PO_4)_2$], DCPD=dicalcium phosphate dihydrate (Brushite) [$CaHPO_4•2H_2O$]. ACP = amorphous calcium phosphate [variable]. Redrawn from Ref. 44.

## 2.3 Materials and Methods

### 2.3.1 Materials

All chemicals used in this work were purchased as described: calcium chloride dehydrate (99+%, A.C.S. Reagent), sodium hydrogen phosphate (99+%, A.C.S. Reagent), disodium citrate dihydrate (99+%, A.C.S. Reagent), sodium metasilicate, and ethylenediaminetetraacetic acid

(99.995%) from Sigma Aldrich (St Louis, MO); indocyanine green from TCI America (Portland, OR); cyclohexane (99.9+%, A.C.S Reagent) from VWR International (West Chester, PA); polyoxyethylene(5) nonylphenyl ether (Igepal® CO-520) from Rhodia Inc. (Cranbury, NJ); ethyl alcohol (200-proof, Absolute, ACS/USP Grade) from Pharmco-AAPER (Brookfield, CT).

All wash solutions were prepared with $CO_2$-free deionized water (pH 7). Water was deionized using a Millipore Milli-Q purification system (Billerica, MA), passed through a 200 nm filter, and boiled while flushing with argon to remove $CO_2$. All pH measurements were performed using a Sentron ISFET pH probe (Argus IP 65 ISFET, Sentron Inc., The Netherlands) calibrated against aqueous standards.

### 2.3.2 Synthesis of Dye-Encapsulating Calcium Phosphosilicate Nanoparticles (CPSNPs)

Dye-doped, amorphous calcium phosphosilicate nanoparticles (CPSNPs) were synthesized employing a double reverse microemulsion approach (Figure 2-3). The two reverse microemulsions were formed by a cyclohexane/nonylphenoxyl (glycolether) (Igepal CO-520)/water system; 650 μL of $10^{-2}$ M $CaCl_2$ was added to 14 mL of a 29 volume percent solution of Igepal CO-520 in cyclohexane (Microemulsion A), while 65 μL each of $6x10^{-3}$ M disodium phosphate and $8.3x10^{-3}$ M disodium silicate was added to a separate 14 mL of a 29 volume percent Igepal CO-520/cyclohexane mixture (Microemulsion B) (see scheme in Figure2-4). This ternary composition (62.6wt% oil, 32.1wt% surfactant, 5.3wt% $H_2O$) falls within the shaded microemulsion region of the phase diagram for the similar system presented in Figure 2-1. The dopant fluorophore (520 μL of $10^{-2}$ M ICG) was added to Microemulsion B based on charge considerations to preclude precipitation-inhibition that can occur once calcium binds to the sulfonate-groups present on the fluorophore molecule. All solutions were in $CO_2$-free deionized water (pH 7) unless otherwise noted. The microemulsions were equilibrated under constant

stirring for 5 minutes before being combined to form a microemulsion mixture (Microemulsion C) which served as a microreactor for the precipitation of the CPSNPs and the ICG entrapment. Microemulsion C was stirred for 2 minutes before the dispersant, 225 µL of $10^{-3}$ M sodium citrate, was added and stirred for an additional 15 minutes. Finally, the micelles were disrupted with 50 mL of ethanol adjusted to an ionic strength of $3.5x10^{-4}$ with KOH before laundering via a van der Waals high performance liquid chromatography (vdW-HPLC) procedure, whereby control of electrostatic charge during different stages of the laundering procedure washes and separates the concentrated particle suspension from the synthesis precursors.

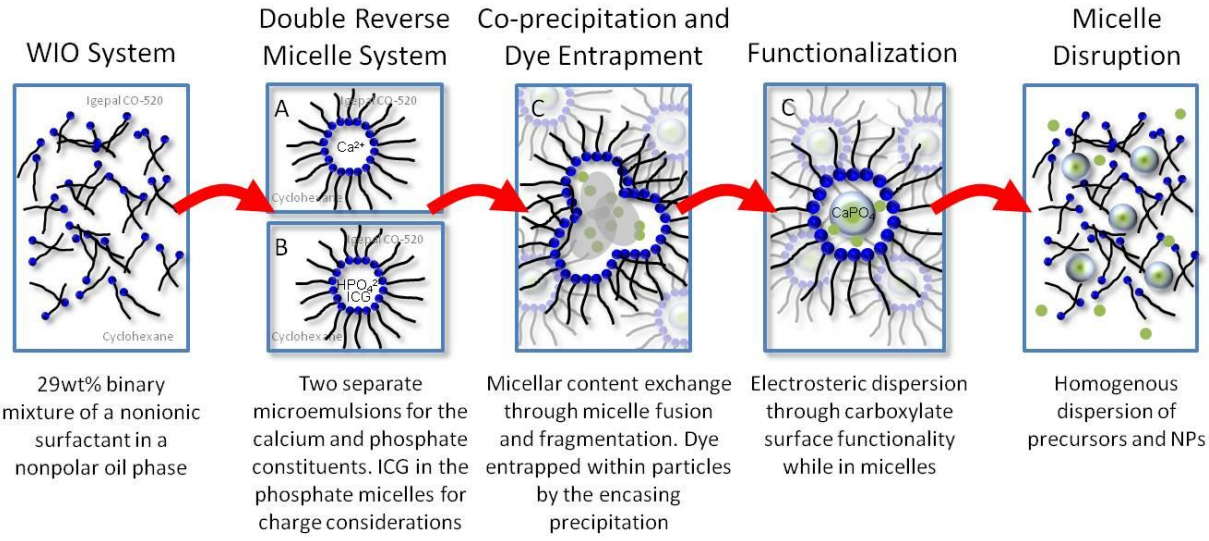


**Figure 2-3.** Illustration of the stages of the CPSNP synthesis and ICG encapsulation. Particles are templated within water-in-oil (WIO) self-assembled reverse micelles, within which precipitation occurs upon micellar exchange of the calcium and phosphate constituents during dynamic fusion and fragmentation of the nano-chambers. A fraction of ICG molecules are indirectly entrapped within each forming particle during precipitation. Individual CPSNPs are functionalized while still encased in their respective template, providing the necessary electrosteric surface charging to remain dispersed in suspension upon micellar disruption.

### 2.3.3 Laundering of CPSNP Suspensions

The particles were washed by first loading the sample solution onto a chromatography column containing silica microspheres (Stellar Phases Inc., ~20 μm diameter, 60 Å pores). The principles behind this washing scheme, which exploit the variable surface charging interactions between the media and NPs in different solvent environments, are illustrated in Figure 2-5. During this loading, the CPSNPs adhered to the silica media due to the negligible surface charge present in the low dielectric solution of the post-disrupted sample volume, which was approximately 25 v/o cyclohexane in ethanol. The system was then flushed with ethanol (IS $3.5x10^{-4}$) and monitored at the characteristic absorption wavelength of ICG (785 nm) using a UV-Vis absorption detector (Shimadzu SPD-6A; Shimadzu Scientific, Kyoto, Japan). The ethanol mobile phase swept the synthesis precursors and any unencapsulated dye through the column, while the relatively large van der Waals attraction between the CPSNPs and column media caused retention of the particles within the column. This washing step was concluded only when the detector reached the pre-set baseline, indicating the removal of residual free dye, and stabilized for 10 additional minutes to remove any remaining synthesis precursors on the column.

The CPSNPs, which remained bound on the column, were then eluted with a 7:3 ethanol:water solution, which provided enough charge for electrostatic repulsion to dominate the CPSNP-silica media interaction energies, allowing the particles to traverse down the column for collection. The first major peak, corresponding to the elution of the doped particles, was collected. The ethanol mobile phase was adjusted with small additions of 1 M aqueous KOH for an ionic strength of $3.5x10^{-4}$. The eluent was prepared with $CO_2$-free deionized water and also adjusted to pH 7 with 1 M KOH.

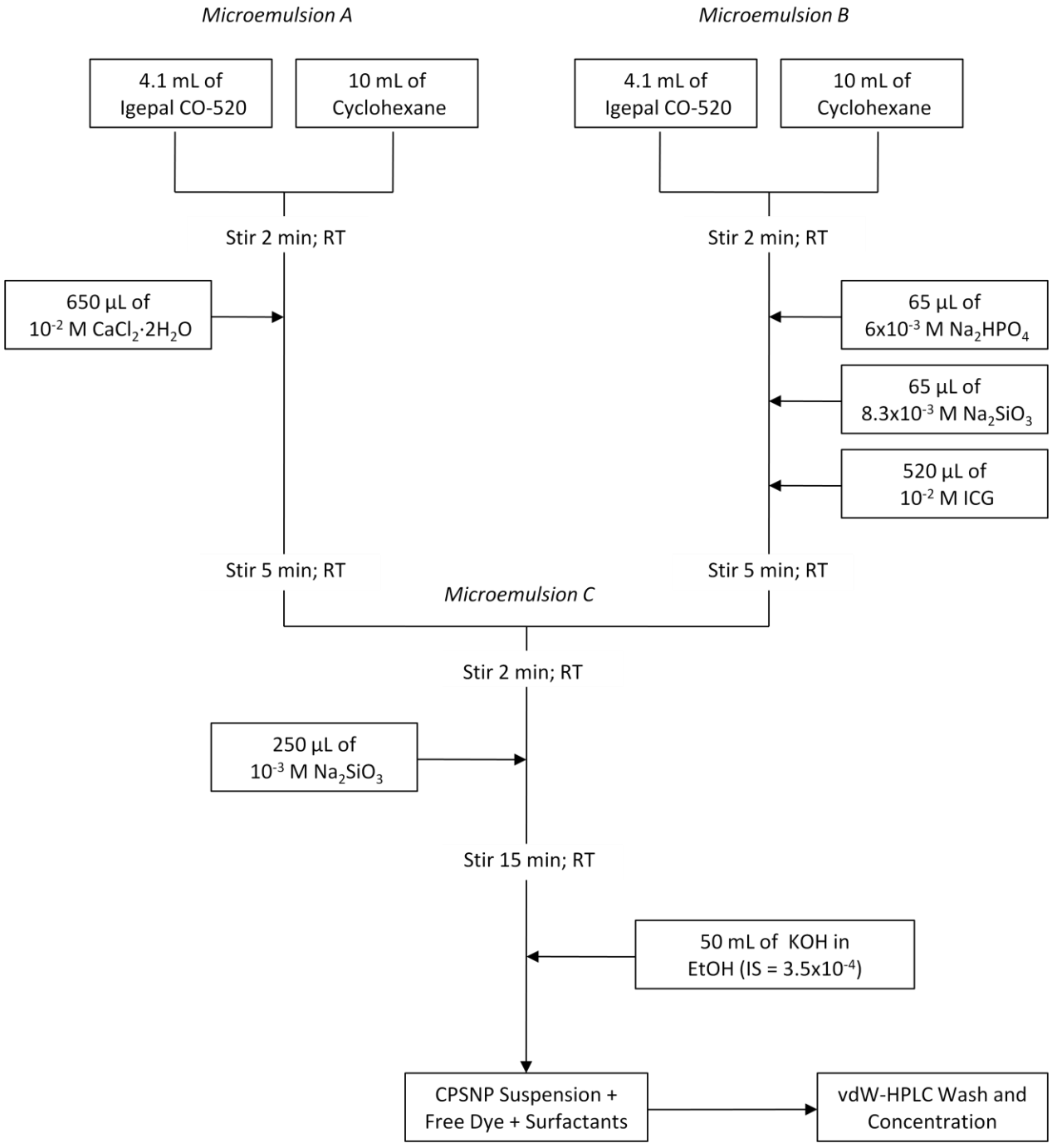


**Figure 2-4.**Synthesis flow chart for the precipitation of calcium phosphosilicate nanoparticles (CPSNPs). The synthesis uses a template formed by the self-assembly of the reverse microemulsion in a water-in-oil cyclohexane/ polyoxyethylene(5) nonylphenyl ether/water ternary system.

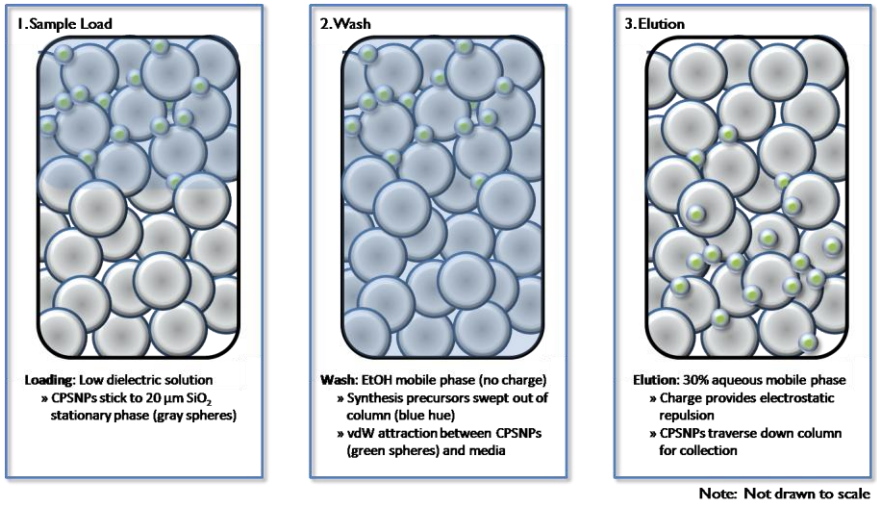


**Figure 2-5.** Illustration of the van der Waals-HPLC laundering method. The sample suspension is loaded onto a packed column of 20 µm diameter silica microspheres in the as-synthesized, low dielectric solution of 25 v/o cyclohexane in ethyl alcohol. The column is then washed with an ethanol mobile phase that flushes synthesis precursors and unencapsulated dye out, while the CPSNPs are reversibly bound to the stationary phase. The CPSNPs are finally swept off the column by introducing a 30 v/o water in ethanol eluent that promotes electrostatic charging, causing a repulsion between the nanoparticles and the $SiO_2$ media.

### 2.3.4 Characterization of CPSNPs

The size, morphology and state of dispersion of the nanoparticles were characterized using a Philips 420 transmission electron microscope (TEM), while chemical information of individual particles were discerned from ionization edges in the electron energy loss spectrum (EELS) conducted on a JEOL 2010F TEM in scanning mode. Samples were prepared on lacey carbon support film on a 300-mesh copper specimen grid (#LC305-CU; Electron Microscopy Sciences, Hatfield, PA). Each TEM specimen was prepared by dropping as-prepared suspensions of CPSNP in 70:30 ethanol:water on the TEM grid. All imaging was conducted at 120 keV with current densities below 70 $pA/cm^2$ to avoid beam damage to the organic-inorganic composite nanoparticles. ImageJ software (freeware available through NIH) was used to provide the particle diameter for each particle in the TEM photomicrographs and PeakFit (v.4.12; Jandel Scientific,

San Rafael, CA) used to fit the diameter data to a log normal distribution by area. EELS maps were collected on individual particles favorably positioned over vacuum (hanging off the C film). The EELS probe was 1 nm in diameter and collected ionization edges every 10 nm across the particle in scanning (STEM) mode. Map psuedocoloring and quantification were conducted using DigitalMicrograph$^{TM}$ software (Gatan Inc., Pleasanton, CA).

To validate this chemical composition and eliminate any subjectivity associated with single particle assumptions, a bulk chemical analysis was conducted on a dried suspension of CPSNPs with energy dispersive X-ray spectroscopy (EDS). A particle suspension was dried at 250$^{o}$C overnight in a conical-bottom glass vial. The dried solids were reconstituted into 100 uL of deionized water, pipetted onto carbon tape on an aluminum scanning electron microscope (SEM) stub, and dried again at 120$^{o}$C for one hour. Analysis was conducted in an FEI Quanta 200 environmental scanning electron microscope (ESEM) (FEI, Hillsboro, Oregon) under low vacuum (0.6 – 0.83 torr) and EDS spectra collected with a gaseous SE detector. Quantification was conducted using INCAEnergy software (Oxford Instruments, Abingdon, UK).

The zeta potential distributions were collected using a Brookhaven ZetaPALS zeta potential analyzer in ZetaPLUS mode (Brookhaven Instruments Corp., Holtsville, NY). The particles were analyzed without dilution (7:3 EtOH:$H_2O$, pH 7) and are the average of seven measurements comprised of five runs each.

The fluorophore encapsulation yield was determined by relating the concentration of ICG encapsulated within the CPSNPs in suspension, to the initial concentration of the fluorophore added to microemulsion B. The ICG content within the particles was quantified by measuring the optical absorption at 785 nm of the dye molecules released from the particles (to remove optical effects associated with the presence of the scattering particle shell). This release of the encapsulated fluorophore was induced with the addition of a 10:1 volume ratio of a $10^{-3}$ M solution of ethylenediaminetetraacetic acid (EDTA) to the particle suspension. EDTA is a

chelating agent that sequesters the divalent $Ca^{2+}$ ion from the nanostructure, dissolving the CPSNPs. The 785 nm absorption value of the released ICG was compared to a standard curve of absorption units as a function of ICG molarity collected in an EDTA-salt solution ($10^{-3}$ M EDTA, 5 x $10^{-4}$ M $CaCl_2$, 3 x $10^{-4}$ M $Na_2HPO_4$, 4.1 x $10^{-5}$ M $Na_2SiO_3$) in a binary 7:3 EtOH:$H_2O$ solvent mixture, designed to be isotonic to the solvent environment that arises post-nanoparticle dissolution. This analysis determined the true fluorophore concentration encapsulated within the original (intact) particles in suspension.

## 2.4 Results and Discussion

### 2.4.1 Synthesis and Washing of NIR dye-doped CPSNPs

Spherical CPSNPs doped with ICG were synthesized using aqueous precipitation of calcium chloride and disodium hydrogen phosphate in the presence of disodium silicate within water-in-oil microemulsions as described above. ICG doping was accomplished through the designed addition of the fluorophore into the microemulsion during precipitation, of which a portion of the molecules are inadvertently entrapped and internalized within the forming particle.

Particle suspensions were then laundered via a van der Waals high performance liquid chromatography (vdW-HPLC) protocol to remove residual synthetic components and concentrate the particles in a 7:3 by volume ethanol:water mixture.[49] A representative absorption chromatrogram (785 nm) is presented in Figure 2-5. This washing protocol exploits the difference between the relatively strong long range van der Waals attraction associated with condensed matter (i.e., two solid particles interacting with one another) as opposed to the short range and weaker van der Waals interaction between uncharged molecules and solid surfaces.[50] Control over the electrostatic surface charges with the mobile phase solvent provides the ability to either

inhibit or promote surface charging with relatively non-polar and polar solvents, respectively. The sample, which is approximately 25 volume percent cyclohexane in ethanol after micellar dissolution, is initially loaded onto the silica HPLC column. Surface charge inhibition with this non-polar washing solvent permits the van der Waals attractive forces to dominate, and reversible particle adhesion onto the stationary phase is achieved. By maintaining this non-polar environment, the weakly attracted organic molecules, such as amphiphiles and free dye, are flushed through the column while the particles remain adhered, hence the decrease in absorption associated with the fluorophore (785 nm) or optical density of the shorter scattering wavelength (400 nm) in the chromatograms as a function of wash duration. Shifting to a more polar solvent, in this case 70:30 ethanol:water by volume, increases the surface charging on both the stationary phase as well as the nanocolloids and provides significant electrostatic repulsion to overcome the van der Waals attractive forces, allowing the particles to break off of the column and be eluted, indicated by the sharp elution peak in the laundering chromatograms. The point of CPSNP collection is indicated by the yellow band in Figure 2-6. The end result is a concentrated solution of well-dispersed nanocolloids in a total volume of 13 mL in a 7:3 EtOH:$H_2O$ binary aqueous mixture. It is clear that while the elution peak is recovered, there are particles that are prematurely forced out of the column during the loading and washing steps that are indistinguishable from the free fluorophore until background subtraction is applied, and are thus ultimately lost in the process.

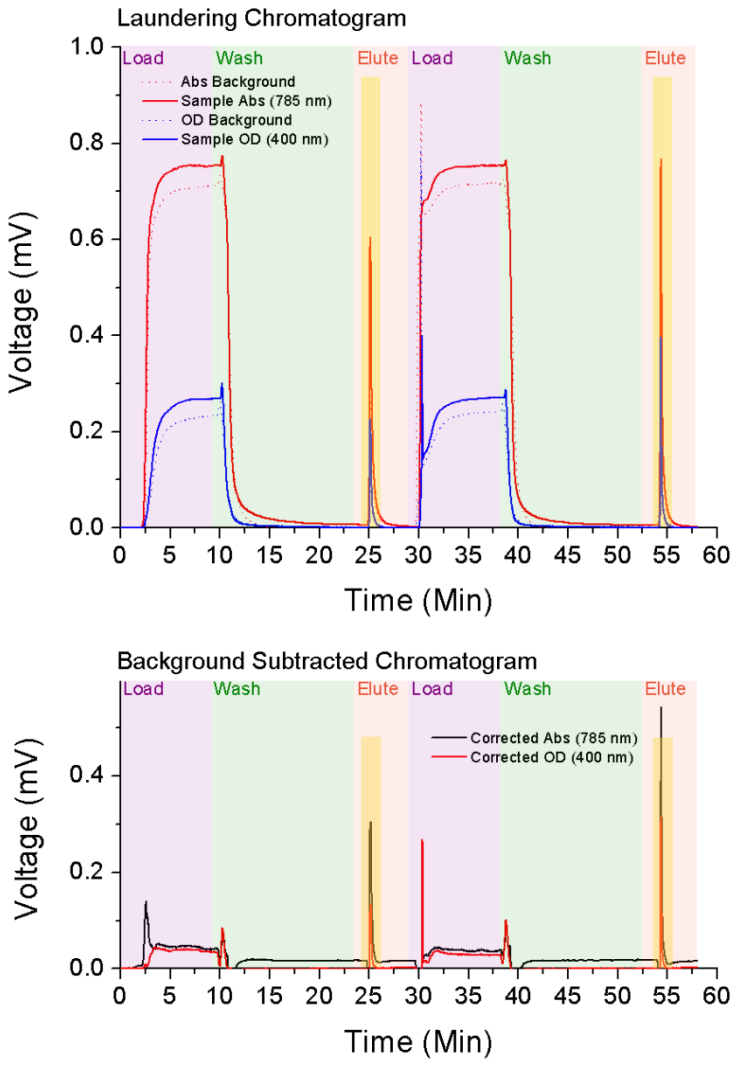


**Figure 2-6.** Chromatograms collected from the in-line UV-Vis detector during sample laundering are presented for both the characteristic absorption wavelength of the fluorophore (785 nm - red), and a non-absorbing, short wavelength for particle scattering (400 nm - blue). The top chromatogram presents the raw spectra (solid lines) and the background of particle-free solutions (dotted lines). The bottom spectra are adjusted by subtracting the background such that the optical response is directly attributed to the CPSNPs. The yellow bands in each chromatogram indicate the point of collection.

### 2.4.2 Colloidal Characterization

Colloidal characterization included the size distribution, morphology, and the state of dispersion of the collected nanoparticle suspensions, as well as the chemical composition of individual CPSNPs using transmission electron microscopy (TEM). Figure 2-7 is a TEM micrograph of the ICG-doped CPSNPs. The figure underscores the well dispersed state of the suspension, with the magnified inset illustrates the representative particle size and spherical morphology. Figure 2-8 presents the log normal particle size distribution of a CPSNP suspension based on TEM particle counting. The mean log normal diameter is 16 nm with a log normal standard deviation equal to 0.23 for 99 percent of the distribution (n = 932). The log normal standard deviation of 0.23 gives a value of 9 nm for -1 standard deviation and 27 nm for +1 standard deviation from the mean value. This size range falls within the accepted window for the most efficient cellular uptake ($\leq$ 50 nm) and closely matches the optimal size of 25 nm for receptor-mediated endocytosis.[51]

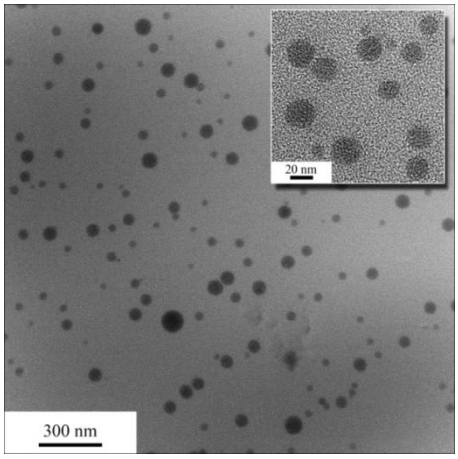


**Figure 2-7.** A TEM micrograph of a dye-encapsulating ICG-CPSNP dispersion with a magnified inset showing the particles in detail. The imaged CPSNPs are clearly spherical in morphology, a consequence of templating with reverse micelles. The particles are also well dispersed, as individual particles are visibly isolated with no signs of aggregate structures present across the carbon film of the sample grid.

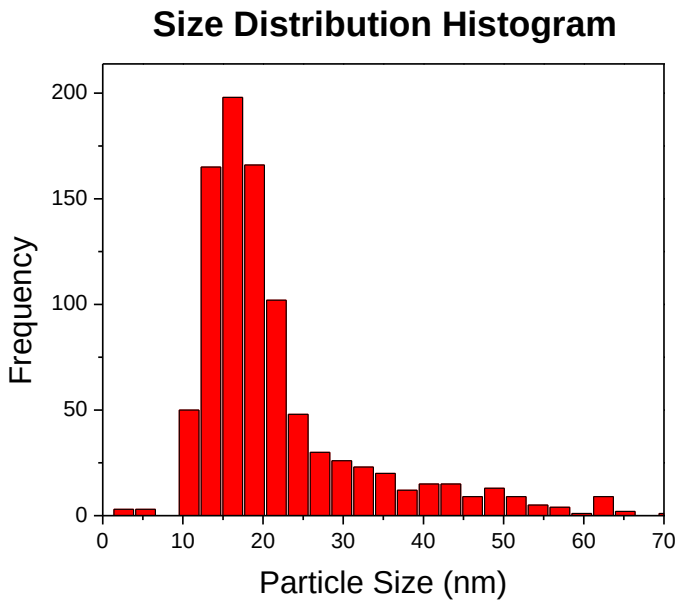


**Figure 2-8.**The log normal mean and standard deviation of the particle number distribution is 16 nm (n = 932) with a $\sigma_z$ equal to 0.23, respectively. The log normal standard deviation of 0.23 gives a value of 9 nm for -1 standard deviation and 27 nm for +1 standard deviation from the mean value. A second peak centered at 63 nm comprising 1 percent by area with a log normal standard deviation equal to 0.01 is also evident, and is attributed to the coalescence of multiple micelles at the moment of disruption.

A second peak centered at 63 nm comprising 1 percent by area with a log normal standard deviation equal to 0.01 was also determined by the log normal probability fit. This latter peak is real as seen in the TEM of Figure 2-7, and is attributed to the coalescence of multiple micelles in the microemulsion at the time of disruption.

As introduced in Chapter 1, silicate addition to the calcium phosphate matrix is intended to decrease the solubility of the amorphous calcium phosphate phase. Previous x-ray diffraction data (not shown) identified the amorphous nature of the synthesized NPs.[52] Figure 2-9 maps the local chemical composition across a single CPSNP. The EELS map depicts a homogeneous distribution of Ca, P, and Si atoms across the particle, with no apparent core or shell architecture. Furthermore, quantitative analysis of the EELS data reveals a 1:1.72:0.41 Ca:P:Si atomic ratio. The relatively low Ca contribution is likely due to calcium-dye complexes that form within the

micelles and are excluded from the precipitation of the nanostructures. However, by nature of the EELS collection, for which zero background is ideal and thus a particle must hang off the carbon film over vacuum, this characterization technique is limited to small population sizes; evaluation was conducted on only five adequately positioned particles out of the thousands present on the TEM grid, hardly satisfactory for a representation of the entire suspension. Therefore, to corroborate this elemental composition as satisfactorily representative of the suspension, EDS spectra were collected on a dried suspension. Both the spectra and the quantitative results are presented in Figure 2-10. The probe size for EDS in the ESEM was 200 nm. Therefore, at the size scale of the individual particles, this technique can be considered a bulk analysis. The elemental composition and ratios of the individual CPSNP from EELS and the bulk suspension from EDS match nicely. A sodium peak is detected in the bulk EDS spectra that is absent in the individual EELS map. The presence of this Na signal is attributed to the ESEM sample preparation, in which a suspension was dried onto the Al sample stub. Any free ions in the solution would thus crystallize upon drying and materialize in the analyte area.

Previous reports have conveyed the long-term particle stability of CPSNPs via dynamic light scattering at 37$^{o}$C in phosphate buffered saline (PBS) for weeks.[53] This dispersion is fostered through electrostatic repulsion via citrate surface functionalization.[54] Sodium citrate is a well known complexing agent for calcium,[55] and was thus expected to adsorb strongly to the CPSNP surface and provide a highly negative surface potential. Light scattering particle electrophoretic mobility was used to verify the surface charge on the CPSNPs.

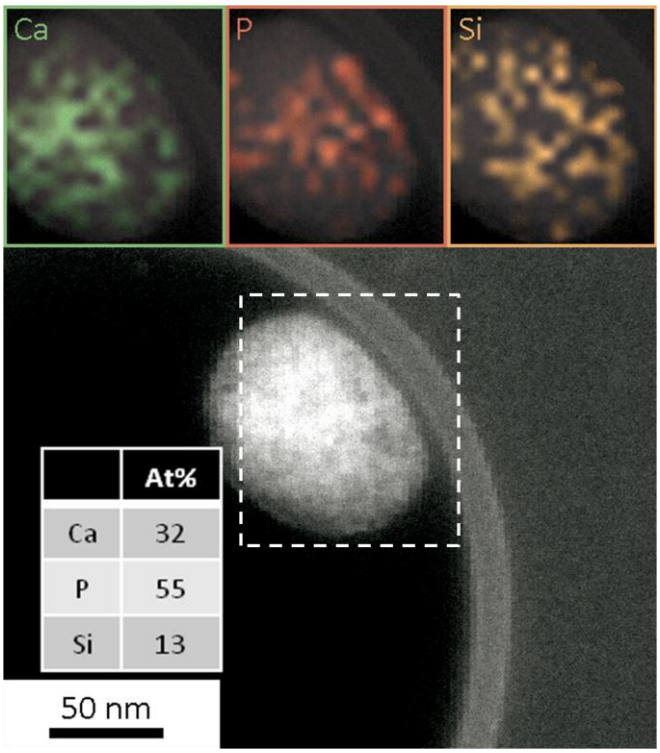


**Figure 2-9.** EELS map of elements Ca, P, and Si across a single particle. The pseudocoloring reveals a homogenous distribution of elements throughout the particle volume with no discernible morphological characteristics, such as a Si rich shell or organic rich core (C map not shown).

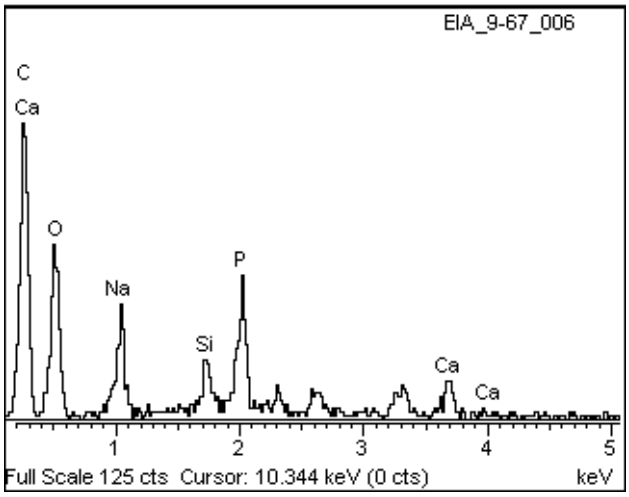


**Figure 2-10.** EDS spectra collected on a dried suspension of CPSNPs. The probe size relative to primary particle diameters renders this technique a bulk analysis. The quantification of the bulk particles (32% Ca, 55% P, 13% Si) matches nicely with the elemental analysis collected for an individual particle by EELS. The presence of a Na peak in the spectra is attributed to free ions in solution that crystallize upon drying and are present in the analyte area.

Figure 2-11 shows the zeta potential distributions in 7:3 ethanol:water (pH 7) of the as-synthesized carboxy-terminated CPSNPs and those coated with a polyethylene glycol (PEG) layer that will be introduced in Chapter 4. The citrate-functionalized CPSNPs exhibit a reasonably high- magnitude negative charge of -29 ±3 mV. The citrate functionalization provides the electrostatic repulsion to avert particle agglomeration in suspension that is absent in alternate CPNP work reported in the literature.[6, 12]

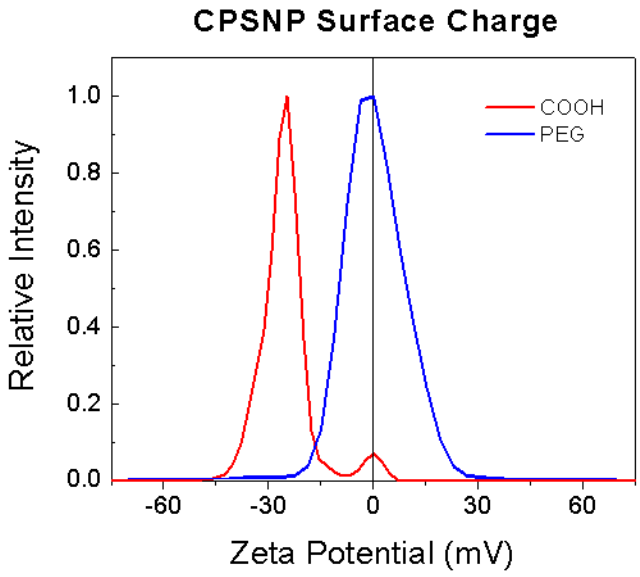


**Figure 2-11.** Zeta potential distributions of CPSNP suspensions in 7:3 EtOH:$H_2O$ (pH 7). The zeta potential of an as-synthesized suspension of citrate-functionalized CPSNPs is -29 ± 3 mV, consistent with the carboxylate ($COO^-$)-termination. The surface passivation with polyethylene glycol (PEG) shifts the distribution of charge to a net zero charge (3 ± 2 mV).

### 2.4.3 Particle Number Calculation

The solids loading of the CPSNP suspensions is needed for subsequent evaluation and characterization, particularly when assessing the optical performance of the internalized fluorophores (Chapter 3). A particle number was calculated from the synthesis parameters, the approximate elemental composition of particles, and a few essential assumptions.

The total mass of calcium phosphosilicate (CPS) synthesized, based on the chemical formula of $\left[Ca_{3.2}(PO_4)_{5.5}\,(SiO_x)_{1.3}(OH)_y\right]$ (EELS data above) and 100% yield, is calculated as:

$$moles_{CPS} = \left\{\frac{6.5 \times 10^{-6}\ moles_{CaCl_2.2H_2O}}{3.2}\right\} = 2.0 \times 10^{-6}\ moles_{CPS} \qquad \text{[Eqn. 2-1]}$$

$$Mass_{CPS} = \ (2.0 \times 10^{-6}\ moles_{CPS}) \times \left(707.7 \frac{g_{CPS}}{mole_{CPS}}\right) = 1.4 \times 10^{-3}\ grams_{CPS} \qquad \text{[Eqn. 2-2]}$$

for a minimum formula weight of the synthesized CPS of 707.7 g· $mol^{-1}$ for x, y = 1. The theoretical mean CPSNP mass is then calculated as:

$$Vol_{CPSNP} = \frac{4}{3}\pi\left(\frac{d}{2}\right)^3 = 2.2 \times 10^{-18}\frac{mL}{particle} \qquad \text{[Eqn. 2-3]}$$

where the mean diameter (*d*) of a CPNP is 16 nm, as determined above. The composite particles are assumed to comprise approximately 10 weight % organic, based on a monolayer surface coverage of citrate per CPSNP and encapsulated fluorophore content. The 90 wt% CPS contribution was calculated above to be 1.4 x $10^{-3}$ grams, thus the total mass is equal to 1.56 x $10^{-3}$ grams, and the mass of organic is 0.156 x $10^{-3}$ grams. The density of the synthesized amorphous calcium phosphosilicate is approximated to 3.0 g/$cm^3$, a median value for calcium phosphate phases (dicalcium phosphate dihydrate; $Ca(HPO_4)H_2O$ $\rho_o$=2.929 g/$cm^3$, hydroxyapatite; $Ca_{10}(PO_4)_6(OH)_2$ $\rho_o$=3.156 g/$cm^3$), while the density of associated organics are assumed to be $\rho_o$=1.0 g/$cm^3$ . Using these density approximations, the volume fraction of CPS and organic per composite ICG-CPSNP is calculated to 75 vol% and 25 vol%, respectively. Accordingly, the density of a single CPSNP is approximated to:

$$\rho_{CPSNP} = 0.75\left(3.0\frac{g}{cm^3}\right) + 0.25\left(1.0\frac{g}{cm^3}\right) = 2.5\frac{g}{cm^3} \qquad \text{[Eqn. 2-4]}$$

The theoretical mass of an individual CPSNP is thus calculated to be

$$Mass\ _{CPSNP} = (2.2 \times 10^{-18} mL) \times \left(2.5\frac{g}{mL}\right) = 5.5 \times 10^{-18}\frac{g}{particle} \qquad \text{[Eqn. 2-5]}$$

such that the theoretical number of CPSNPs synthesized ($N_{CPSNP}$) is

$$N_{CPSNP} = \frac{1.4 \times 10^{-3} g}{5.5 \times 10^{-18} \frac{g}{particle}} = 2.5 \times 10^{14}\ particles \qquad \text{[Eqn. 2-6]}$$

and the average solids loading of a CPSNP suspension amounts to:

$$CPSNP\ Solids\ Loading = \frac{2.5\ \times\ 10^{14} particles}{13\ mL} = 1.9\ \times\ 10^{13}\ \frac{particles}{mL} \qquad \text{[Eqn. 2-7]}$$

### 2.4.4 Fluorophore Encapsulation Yield

The fluorophore encapsulation yield was determined by comparing the concentration of dye released from the particles to the initial concentration used in microemulsion B. The average ICG concentration for a standard 13 mL CPSNP suspension is 2 x $10^{-6}$ M, which amounts to a mere 0.5% capture of the fluorophore. Based on the theoretical particle number calculated above, on average, there are 63 molecules of ICG encapsulated within each CPSNP.

The encapsulation yield has been increased to 9% (3.5 x $10^{-5}$ M, ~1000 molecules per CPSNP) when the pre-equilibration time prior to micelle mixing to form microemulsion C was lengthened to 60 minutes and great care was taken to shield the solutions and micelles from ambient light. However, this was not the standard procedure, and all subsequent characterizations and *in vivo* experiments presented herein involved CPSNP suspensions encapsulating 2 x $10^{-6}$ M ICG.

## 2.5 Summary

A template synthesis in the self-assembled reverse microemulsion of a water-in-oil cyclohexane/ polyoxyethylene(5) nonylphenyl ether/water ternary system was used to precipitate

calcium phosphosilicate nanoparticles (CPSNPs). These nanoparticles were designed to encapsulate the NIR active fluorophore ICG, which was added to the micelles prior to precipitation. Functionalization of the CPSNPs was achieved with the reaction of sodium citrate, yielding a carboxylate-terminated surface. The sample suspension was then laundered via a van der Waals-HPLC protocol that utilizes surface charging to separate and concentrate the CPSNPs from the synthesis precursors and unencapsulated fluorophore molecules.

Imaging with TEM revealed the well dispersed state of particles, the spherical morphology, and the log normal mean particle diameter of 16 nm. EELS mapping identified a chemical compositional Ca:P:Si ratio of 1:1.72:0.41, which was found to be homogeneous in composition without evidence of a particular elemental rich or deficient region. Zeta potential of the citrate-functionalized CPSNPs was measured to be -29 ±3 mV. Finally, a theoretical solids loading of $1.9 \times 10^{13}$ CPSNP/mL was calculated for a standard suspension. The mean ICG content per suspension is $2 \times 10^{-6}$ M, which equates to approximately 63 fluorophore molecules encapsulated per CPSNP.

## 2.6 Acknowledgements

The TEM characterization of these delicate organic-inorganic composites was developed with the help of Matt Olszta and Trevor Clark of the Materials Research Institute (MRI; Penn State). The EELS analysis for Figure 2-8 was conducted by both Trevor Clark and Joe Kulik, manager of the TEM facility at MRI. The vdW-HPLC laundering protocol was modified from the original work of Jun Wang and Sarah Rouse, and developed into its present state in collaboration with Thomas Morgan.

## 2.7 References


1. Weber, J. N.; White, E. W.; Lebiedzik, J. New Porous Biomaterials Replication of Echinoderm Skeletal Microstructures. *Nature* **1971,** *233*, (5318), 337-339.
2. Dubok, V. A. Bioceramics - Yesterday, Today, Tomorrow. *Powder Metall. Met. C.* **2000,** *39*, (7-8), 381-394.
3. Chiroff, R. T.; White, R. A.; White, E. W.; Weber, J. N.; Roy, D. M. The Restoration of Articular Surfaces Overlying Porous Biomaterials. *J. Biomed. Mater. Res.* **1977,** *11*, (2), 165-178.
4. He, Q.; Mitchell, A. R.; Johnson, S. L.; Wagner-Bartak, C.; Morcol, T.; Bell, S. J. D. Calcium Phosphate Nanoparticle Adjuvant. *Clin. Diagn. Lab. Immunol.* **2000,** *7*, (6), 899-903.
5. Radin, S.; Campbell, J. T.; Ducheyne, P.; Cuckler, J. M. Calcium Phosphate Ceramic Coatings as Carriers of Vancomycin. *Biomaterials* **1997,** *18*, (11), 777-782.
6. Bisht, S.; Bhakta, G.; Mitra, S.; Maitra, A. Pdna Loaded Calcium Phosphate Nanoparticles: Highly Efficient Non-Viral Vector for Gene Delivery. *Int. J. Pharm.* **2005,** *288*, 157-168.
7. Schmidt, H. T.; Gray, B. L.; Wingert, P. A.; Ostafin, A. Assembly of Aqueous-Cored Calcium Phosphate Nanoparticles for Drug Delivery. *Chem. Mater.* **2004,** *16*, 4942-4947.
8. Olton, D.; Li, J.; Wilson, M. E.; Rogers, T.; Close, T.; Close, J.; Huang, L.; Kumta, P. N.; Sfeir, C. Nanostructured Calcium Phosphate (Nanocaps) for Non-Viral Gene Delivery: Influence of Synthesis Parameters on Transfection Efficiency. *Biomaterials* **2007,** *28*, 1267-1279.
9. Roy, I.; Mitra, S.; Maitra, A.; Mozumdar, S. Calcium Phosphate Nanoparticles as Novel Non-Viral Vectors for Targeted Gene Delivery. *Int. J. Pharm.* **2003,** *250*, 25-33.
10. Sokolova, V.; Prymak, O.; Meyer-Zaika, W.; Colfen, H.; Rehage, H.; Shukla, A.; Epple, M. Synthesis and Characterization of DNA-Functionalized Calcium Phosphate Nanoparticles. *Mat.-wiss. u. Werkstofftech* **2006,** *37*, (6), 441-445.
11. Schmidt, H. T.; Ostafin, A. E. Liposome Directed Growth of Calcium Phosphate Nanoshells. *Adv. Mater.* **2002,** *14*, (7), 532-535.
12. Welzel, T.; Meyer-Zaika, W.; Epple, M. Continuous Preparation of Functionalised Calcium Phosphate Nanoparticles with Adjustable Crystallinity. *Chemical Communication* **2004,** *DOI: 10.1039/b402521k*, 1204-1205.
13. Sarda, S.; Heughebaert, M.; Lebugle, A. Influence of the Type of Surfactant on the Formation of Calcium Phosphate in Organized Molecular Systems *Chemistry of Materials* **1999,** *11*, 2722-2727.
14. Sadasivan, S.; Khushalani, D.; Mann, S. Synthesis of Calcium Phosphate Nanofilaments in Reverse Micelles. *Chemistry of Materials* **2005,** *17*, 2765-2770.
15. Lim, G. K.; Wang, J.; Ng, S. C.; Gan, L. M. Processing of Fine Hydroxyapatite Powders Via an Inverse Microemulsions Route. *Materials Letters* **1996,** *28*, 431-436.
16. Singh, S.; Bhardwaj, P.; Singh, V.; Aggarwal, S.; Mandal, U. K. Synthesis of Nanocrystalline Calcium Phosphate in Microemulsion - Effect of Nature of Surfactants. *Journal of Colloids* **2008,** *319*, 322-329.
17. Scheirtz, J.; Wiehe, A.; Gräfe, S.; Gitter, B.; Epple, M. Calcium Phosphate Nanoparticles as Efficient Carriers for Photodynamic Therapy against Cells and Bacteria. *Biomaterials* **2009,** *30*, 3324-3331.
18. Puajindanetr, S.; Best, S. M.; Bonfield, W. Characterization and Sintering of Precipitated Hydroxyapatite. *British Ceramic Transactions* **1994,** *93*, 96-99.

19. Welzel, T.; Radtke, I.; Meyer-Zaika, W.; Heumann, R.; Epple, M. Transfection of Cells with Custom-Made Calcium Phosphate Nanoparticles Coated with DNA. *Journal of Materials Chemistry* **2004,** *14*, 2213-2217.
20. Deptula, A.; Lada, W.; Olczak, T.; Borello, A.; Alvani, C.; di Bartolomeo, A. Preparation of Spherical Powders of Hydroxyapatite by Sol-Gel Process. *Journal of Non-Crystalline Solids* **1992,** *147&148*, 537-541.
21. Vallet-Regi, M.; Gutierrez-Rois, M. T.; Alonso, M. P.; de Frutos, M. I.; Nicolopoulos, S. Hydroxyapatite Particles Synthesized by Pyrolysis of an Aerosol. *Journal of Solid State Chemistry* **1994,** *112*, 58-64.
22. Hattori, T.; Iwadate, Y. Hydrothermal Preparation of Calcium Hydroxyapatite Powders. *Journal of the American Ceramic Society* **1990,** *73*, 1803-1805.
23. Lim, G. K.; Wang, J.; Ng, S. C.; Chew, C. H.; Gan, L. M. Processing of Hydroxyapatite Via Microemulsion and Emulsion Routes. *Biomaterials* **1997,** *18*, 1433-1439.
24. Chandradass, J.; Kim, K. H. Size-Controlled Synthesis of Laalo3 by Reverse Micelle Method: Investigation of the Effect of Water-to-Surfactant Ratio on the Particle Size. *Journal of Crystal Growth* **2009,** *311*, 3631-3635.
25. Gan, L. M.; Chan, H. S. O.; Zhang, L. H.; Chew, C. H.; Loo, B. H. Preparation of Fine Lanio3 Powder from Oxalate Precursors Via Reactions in Inverse Microemulsions. *Materials Chemistry and Physics* **1994,** *37*, 263-268.
26. Gobe, M.; Kon-No, K.; Kandori, K.; Kitahara, A. Preparation and Characterization of Monodisperse Magnetite Sols in W/O Microemulsion. *Journal of Colloid and Interface Science* **1983,** *93*, 293-295.
27. Pileni, M. P.; Lisiecki, I. Nanometer Metallic Copper Particles Synthesis in Reverse Micelles. *Colloids and Surfaces A - Physicochemical and Engineering Aspects* **1993,** *80*, 63-68.
28. Kandori, K.; Konno, K.; Kitahara, A. Dispersion Stability of Nonaqueous Calcium-Carbonate Dispersion Prepared in Water Core of W/O Microemulsion. *Journal of Colloid and Interface Science* **1987,** *115*, 597-582.
29. Chew, C. H.; Gan, L. M.; Shah, D. O. The Effect of Alkanes on the Formation of Ultrafine Silver Bromide Particles in Ionic W/O Microemulsions. *Journal of Dispersion Science and Technology* **1990,** *11*, 593-609.
30. Eicke, H.-F.; Rehak, J. On the Formation of Water/Oil-Microemulsions. *Helvetica Chimica Acta* **1976,** *59*, 2883-2891.
31. Zulauf, M.; Eicke, H.-F. Inverted Micelles and Microemulsions in the Ternary System H2o/Aerosol-Ot/Isooctane as Studied by Photon Correlation Spectroscopy. *Journal of Physical Chemistry* **1979,** *83*, 480-486.
32. Zinsli, P. E. Inhomogenous Interior of Aerosol Ot Microemulsions Probed by Fluorescence Ad Polarization Decay. *Journal of Physical Chemistry* **1979,** *83*, 3223-3231.
33. Boutonnet, M.; Kizling, J.; Stenius, P. The Preparation of Monodisperse Colloidal Metal Particles from Microemulsions. *Colloids and Surfaces* **1982,** *5*, 209-225.
34. Kurihara, K.; Kizling, J.; Stenius, P.; Fendler, J. H. Laser and Pulse Radiolytically Induced Colloidal Gold Formation in Water and in Water-in-Oil Microemulsions. *Journal of the American Ceramic Society* **1983,** *105*, 2574-2579.
35. Danielsson, I.; Lindman, B. The Definition of Microemulsion. *Colloids and Surfaces* **1981,** *3*, 391-392.
36. Chieng, T. H.; Gan, L. M.; Chew, C. H. Morphology of Microporous Polymeric Materials by Polymerization of Methyl Methacrylate and 2-Hydroxyethyl Methacrylate in Microemulsions. *Polymer* **1995,** *36*, 1941-1946.

37. Boakye, E.; Rodovic, L. R.; Osseo-Asare, K. Microemulsion-Mediated Synthesis of Nanosize Molybdenum Sulfide Particles. *Journal of Colloid and Interface Science* **1994,** *163*, 120-129.
38. Lim, G. K.; Wang, J.; Ng, S. C.; Gan, L. M. Formation of Nanocrystalline Hydroxyapatite in Nonionic Surfactant Emulsions. *Langmuir* **1999,** *15*, 7472-7477.
39. Bose, S.; Saha, S. K. Synthesis and Characterization of Hydroxyapatite Nanopowders by Emulsion Technique. *Chemistry of Materials* **2003,** *15*, 4464-4469.
40. Langevin, D. Microemulsions. *Accounts of Chemical Research* **1988,** *21*, 255-260.
41. Singh, A.; Mukherjee, M. Effect of Polymer-Particle Interaction in Swelling Dynamics of Ultrathink Nanocomposite Films. *Macromoecules* **2005,** *38*, (21), 8795-8802.
42. Strain, A. J.; Wyllie, A. H. The Uptake and Stability of Simian-Virus-40 DNA after Calcium-Phosphate Transfection of Cv-1 Cells. *Biochemical Journal* **1984,** *281*, 475-482.
43. Dorozhkin, S. V.; Epple, M. Biological and Medical Significance of Calcium Phosphates. *Angewandte Chemie - Internaltional Edition* **2002,** *41*, (17), 3130-3146.
44. Tung, M. S., Calcium Phosphates: Structure, Composition, Solubility and Stability. In *Calcium Phosphates in Biological and Industrial Systems*, Amjad, Z., Ed. Kluwer Academic Publishers: Boston, 1998; pp 1-19.
45. Stubbs, M.; McSheehy, P. M. J.; Griffiths, J. R.; Bashford, C. L. Causes and Consequences of Tumor Acidity and Implications for Treatment. *Molecular Medicine Today* **2000,** *6*, 15-19.
46. Tycko, B.; Maxfield, F. R. Rapid Acidification of Endocytic Vesicles Containing A2-Macroglobulin. *Cell* **1982,** *28*, 643-651.
47. Panyam, J.; Labhasetwar, V. Biodegradable Nanoparticles for Drug and Gene Delivery to Cells and Tissue. *Advanced Drug Delivery Reviews* **2003,** *55*, (3), 329-347.
48. De Groot, K.; Klein, C. P. A. T.; Wolke, J. G. C.; de Blieck-Hogervors, J. M. A. Chemistry of Calcium Phosphate Bioceramics. *CRC Press: Boca Raton* **1990**, 3-17.
49. Wang, J.; White, W. B.; Adair, J. H. Dispersion of $SiO_2$-Based Nanocomposites with High Performance Liquid Chromatography. *J. Phys. Chem. B* **2006,** *110*, 4679-4685.
50. Israelachvili, J., *Intermolecular and Surface Forces*. Second ed.; Academic Press: London, 1992.
51. Gao, H.; Shi, W.; Freund, L. B. Mechanics of Receptor-Mediated Endocytosis. *Proc. Natl. Acad. Sci. USA* **2005,** *102*, (27), 9469-9474.
52. Rouse, S. M. Synthesis and Properties of Unagglomerated Nanocomposite Particles for Nanomedical Applications. *PhD dissertation, Pennsylvania State University* **2005**.
53. Kester, M.; Heakal, Y.; Fox, T.; Sharma, A.; Robertson, G. P.; Morgan, T. T.; Altınoğlu, E. İ.; Tabakovic, A.; Parette, M. R.; Rouse, S. M.; Ruiz-Velasco, V.; Adair, J. H. Calcium Phosphate Nanocomposite Particles for in Vitro Imaging and Encapsulated Chemotherapeutic Drug Delivery to Cancer Cells. *Nano Letters* **2008,** *8*, (12), 4116-4121.
54. Adair, J. H.; Kumar, R.; Antolino, N.; Szepesi, C.; Kimel, R. A.; Rouse, S. M., Colloidal Lessons for Dispersion of Nanosize Particulate Suspensions. In *Proceedings of the World Academy of Ceramics*, Cesenatico, Italy, 2004.
55. Joseph, N. R. The Dissociation Constants of Organic Calcium Complexes. *Journal of Biological Chemistry* **1946,** *164*, 529-541.

# Chapter 3

# Optical Properties of Indocyanine Green-Encapsulating CPSNPs

The first criterion of calcium phosphosilicate nanoparticles (CPSNPs) to serve in any capacity as a theranostic agent is the functional emission of a detectable signal during its use. This signal serves as the means by which a diagnosis of disease is achieved, and will be discussed in Chapter 4. To satisfy this condition, the CPSNPs are embedded with a near infrared (NIR) fluorescing agent in order to continuously emit a strong and stable signal in the therapeutic window of the electromagnetic spectrum. The CPSNP-internalization of this fluorophore is expected to enhance the overall optical performance by way of a matrix-shielding effect. This chapter evaluates these composite fluorescent probes as the imaging element in the diagnostic imaging portion of the proposed bifunctional theranostic modality.

The NIR emitting fluorophore indocyanine green (ICG) was selected as the ideal fluorophore for encapsulation in CPSNPs due, in part, to U.S. Food and Drug Administration (FDA) approval for human use,[1] as well as for reputable and effective clinical use in various optical imaging applications.[2-7] Despite the numerous favorable characteristics presented in Chapter 1, there are several unfortunate photophysical attributes of ICG that diminishes the capacity for clinical deep-tissue imaging, and limits the potential for theranostic use. It is these traits of the free fluorophore that are improved by matrix-shielding via CPSNP encapsulation.

## 3.1 Photo-Excitation and Relaxation of a Fluorophore

In order to rationally appreciate the implications of the impeding photophysical characteristics of ICG, it is necessary to understand the fundamental photoexcitation and

relaxation process. Thus, we begin by reviewing the various mechanisms involved in the relaxation of an excited fluorophore, and then extend our examination to the specific pathways that encumber ICG optical performance.

Figure 3-1 presents a Jablonski diagram that will be used as the starting point for discussing the various molecular processes that can occur between the absorption and emission of light. The diagram depicts the singlet ground, first, and second electronic states by $S_0$, $S_1$, and $S_2$, respectively, each with a number of vibrational energy levels represented by the superscripts 1, 2, 3, etc. The process initiates with the absorption of light with sufficient energy to excite the molecule to a higher energy state (termed *absorption*):

$$S_0 + h\nu \rightarrow S_1^n$$

where $n$ represents some vibrational energy level ($n \geq 1$). This transition between the states is depicted as a vertical line in Figure 3-1 to illustrate the relatively instantaneous nature of light absorption ($10^{-15}$ s).[8] Though the fluorophore is typically excited to some higher vibrational level of the first or second excited state, molecules in condense phases rapidly relax to the lowest vibrational level of $S_1$ via thermal or vibrational processes that are termed internal conversion (IC), which generally occur within $10^{-12}$ s or less:[8]

$$S_1^n \xrightarrow{k_{IC}} S_1^1$$

where $k_{IC}$ is the rate constant for internal conversion. It should be noted that the simplified diagram in Figure 3-1 does not explicitly illustrate the individual relaxation processes that lead to the relaxed $S_1^1$ state, since the time interval of these mechanisms are much faster than the principle $S_1 \rightarrow S_0$ transition relevant to this chapter. Therefore, to simplify matters for this discussion, only those pathways responsible for return to the ground state are individually illustrated.

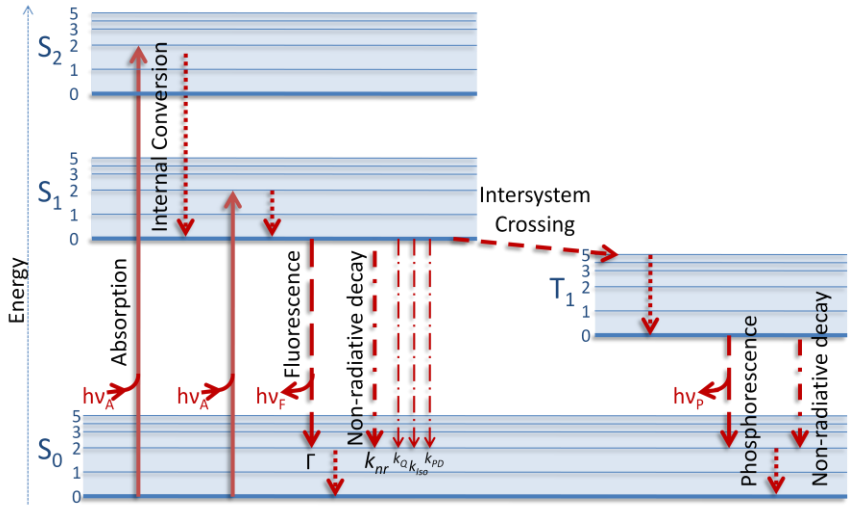


**Figure 3-1.** A simplified Jablonski diagram illustrating the photoexcitation process (absorption [$10^{-15}$ s] to the singlet first and second excited energy states, $S_1$ and $S_2$ respectively, and the various energy deactivation channels (internal conversion [$10^{-12}$ s], fluorescence [$10^{-8}$ s], and non-radiative decay (variable)) that return the molecule to its original ground state ($S_0$). The intersystem crossing process to the excited triplet state ($T_1$), and its associated radiative relaxation channel (phosphorescence [$10^{-2}$ s]), are also illustrated and will be discussed further in Chapter 5.

Once populating the lowest vibrational level of the first excited state ($S_1^1$ is herein simply $S_1$), the electron in the excited orbital is paired (by opposite spin) to the second electron in the ground-state orbital ($S_0$) (Figure 3-2). Consequently, return to the ground state is spin allowed and therefore can occur rapidly by any number of competing processes.[8] These energy relaxations are classified as either radiative or non-radiative mechanisms and are described in detail below.

## 3.2 Fluorescence

The favorable relaxation pathway in terms of an imaging centered application, is the radiative emission of a photon, termed *fluorescence*:

$$S_1 \xrightarrow{h\nu} S_0^n$$

The emission rates of fluorescence are typically on the order of $10^{-8}$ s, and are therefore significantly slower than the rate of IC, thus fluorescence always occurs from the lowest energy vibration state ($S_1$).

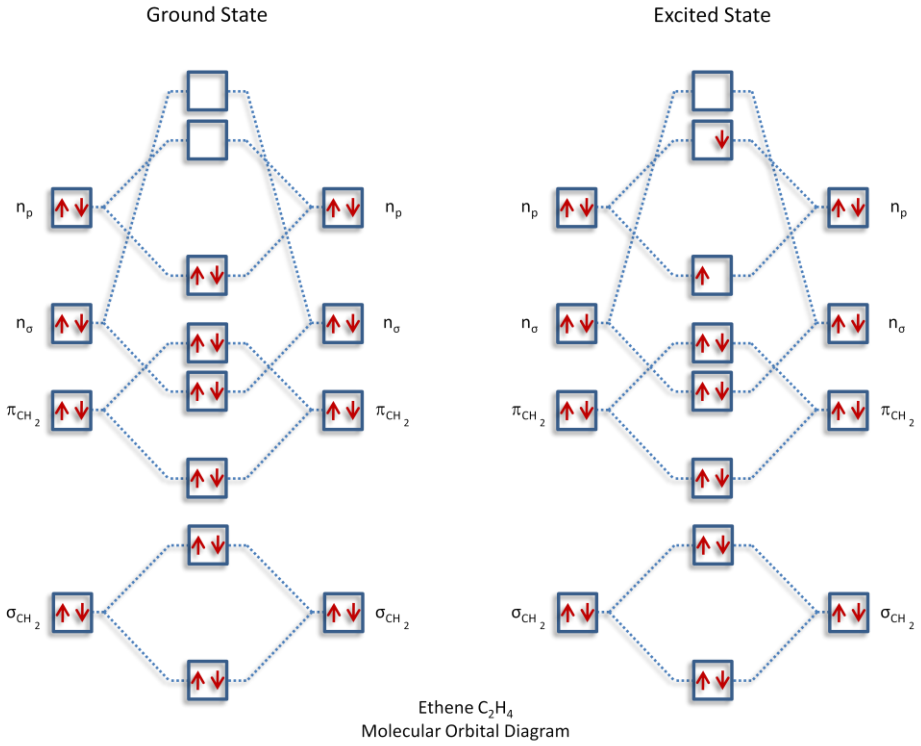


**Figure 3-2.**The molecular orbital (MO) diagram of an ethene molecule ($C_2H_4$) is used to illustrate the spin-opposite paring of the electron elevated to an excited state upon photoexcitation with its associate electron in the highest occupied orbital of the ground state. The return to the ground state is spin allowed and therefore may occur through a variety of relaxation pathways.

However, rivaling the radiative relaxation of fluorescence is a number of alternative, non-radiative relaxations pathways. Though each of these mechanisms is distinct, they often transpire in tandem to varying degrees for any given fluorophore and environmental condition. Therefore, a metric to ascertain the contribution of these non-radiative processes relative to the radiative decay processes is the fluorescence quantum yield.

The quantum yield of fluorescence ($\Phi_F^0$) is the number of emitted photons relative to the total number of absorbed photons, including those that decay via non-radiative processes. The

rate constants for these two decay channels, radiative ($\Gamma$) and non-radiative ($k_{nr}$), both depopulate the excited state, as illustrated in Figure 3-1. Thus, the fraction that decay through radiative emission, $\Phi_F^0$, is given by:

$$\Phi_F^0 = \frac{\Gamma}{\Gamma + k_{nr}} \qquad \text{[Eqn. 3-1]}$$

An ideal fluorophore for imaging applications has a non-radiative decay rate that is much smaller than the rate of radiative decay (that is: $k_{nr} << \Gamma$), and therefore boasts a $\Phi_F^0$ close to unity.[8] The specific radiative and non-radiative rates for ICG in aqueous solutions have been determined at 0.12 $ns^{-1}$ and 6.1 $ns^{-1}$, respectively, resulting in a calculated intrinsic quantum yield of $\Phi_F^0 = 0.16$.[9] In Equation 3-1, all instantaneous non-radiative decay processes are grouped into the single rate constant $k_{nr}$. However, in real systems, most organic dye molecules are prone to additional non-radiative decays to the ground state, particularly in complex physiological environments, that alter the intrinsic yield of a fluorophore and result in actual fluorescence yields ($\Phi_F$) far from the ideal.[8, 10] Indocyanine green is no exception, and presents a notably low fluorescence quantum yield ($0.027 \pm 0.005$ in aqueous solutions) that limits its clinical imaging faculty.[11, 12] In the case of ICG, the low $\Phi_F$ is due to the prevailing incidences of internal conversions,[10, 11] as well as its propensity for photobleaching and nonspecific quenching events, all of which result in non-radiative relaxations and thus limit the utility for sensitive and prolonged *in vivo* applications.[11, 13-15] Each of these mechanisms will be individually addressed as they relate to specific limitations of ICG use *in vivo*.

## 3.3 Non-Radiative Relaxations that Affect ICG

### 3.3.1 Non-specific Static and Dynamic Quenching

The primary opposition to fluorescent relaxation in ICG is the incidence of quenching, defined as any interactive process that ultimately results in the decrease of fluorescence intensity. The most common route of fluorescence quenching in IGC, particularly in physiological environments, is collisional. This deactivation pathway is a result of energy loss upon contact with some proximal molecule in solution. A wide variety of molecules can act as collisional quenchers, including oxygen, halogens, biological amines, and electron-deficient molecules. Numerous efforts have attributed the optical instability of ICG to collisional quenching in a variety of physiologically relevant solutions, such as water,[16-18] salt solutions,[16, 19] plasma,[16, 18, 19] and blood.[18, 20-22].

Aside from collisional events, fluorescence quenching of ICG can occur by a variety of other processes. In particular, ICG can form a non-fluorescent complex with an adjacent ICG molecule, termed self quenching. Self quenching is referred to as static quenching since it occurs in the ground state and does not rely on diffusion or molecular collision.[8] ICG molecules have been shown to dimerize at concentrations as low was $10^{-7}$ M,[17, 23-25] which can attenuate the absorption capacity from the individual molecules at the expense of emission intensity.[26] As concentrations begin to increase above $5 \times 10^{-4}$ M, more molecules begin to form dimers and oligomers (marked by a rise of a new hypsochromic absorbance peak between 680 and 730 nm),[27-29] resulting in further quenching influences and reducing fluorescence. Finally, concentrations on the order of $1.5 \times 10^{-3}$ M trigger the onset of a self-organization and polymerization scheme of oligomers into stable, thread-like arrangements, a process called J-

aggregation.[27] These J-aggregates involve significant self-quenching interactions that markedly reduce fluorescence yields.[11]

The net effect of the incidence of quenching is the reduction in the quantum yield, seen by incorporating this additional mechanism as a contributor to the depletion of the excited state:

$$\Phi_F = \frac{\Gamma}{\Gamma + k_{nr} + k_Q} \ , \qquad \text{[Eqn. 3-2]}$$

where $k_Q$ is the rate constant of all quenching processes. Dividing $\Phi_F^0$ by $\Phi_F$ produces the relative quantum yield, which yields the Stern-Volmer expression:

$$\Phi_F^0 \Phi_F = 1 + \frac{k_Q}{\Gamma + k_{nr}} = 1 + K[Q] \ . \qquad \text{[Eqn. 3-3]}$$

The Stern-Volmer expression specifically relates the decrease in fluorescent emission owing to the incidence of quenching mechanisms. In this expression, *K* is the Stern-Volmer quenching constant and [*Q*] the quencher concentration. The quenching constant *K* indicates the sensitivity of the fluorophore to a particular quencher.

To illustrate the inverse relationship between fluorescence performance (yield) and competing non-radiative relaxation channels, examination of the above relation reveals that the higher the propensity to quenching (larger *K*), the greater the quenching rate constant ($k_q$) contribution to the denominator of radiative efficiency (Equation 3-2), and thus, the lower the resultant fluorescent performance ($\Phi_F$).

### 3.3.2 Internal Conversion and Photoisomerization

In addition to quenching mechanisms, a major competitor to fluorescent relaxation of ICG is the non-radiative energy decay consequent to internal conversions (IC).[10, 11] As previously introduced, IC accounts for various thermal and vibrational relaxation processes within the vibrational levels of a given excited state. However, a significant deactivation from such a

process beyond small vibrational decays can promptly return the excited molecule directly to its ground state at the expense of the relatively protracted radiative rate of photon emission. The principle avenue of such internal conversion in ICG has been attributed to reversible rotational relaxations of the molecule, specifically the *cis*/*trans* photoisomerizations.[30] This is ascribed primarily to the non-planar structure of the molecule arising from a conformationally loose polymethine chain linking the substituent heteroaromatic fragments.[31-35] Upon photoexcitation, the molecule can structurally convert from its native *cis*-configuration (substituent groups oriented in the same direction), to the *trans*-configured isomer (substituent groups in opposite directions) via a rotation about a double bond in the parent chain of the hydrocarbon (Figure 3-3). This rotation relaxes the excited state back to ground without the radiative emission of a photon. The rate constant for this rotational relaxation is defined as $k_{Iso}$, and, like $k_Q$, directly contends with the rate of fluorescence ($\Gamma$), reducing $\Phi_F$.

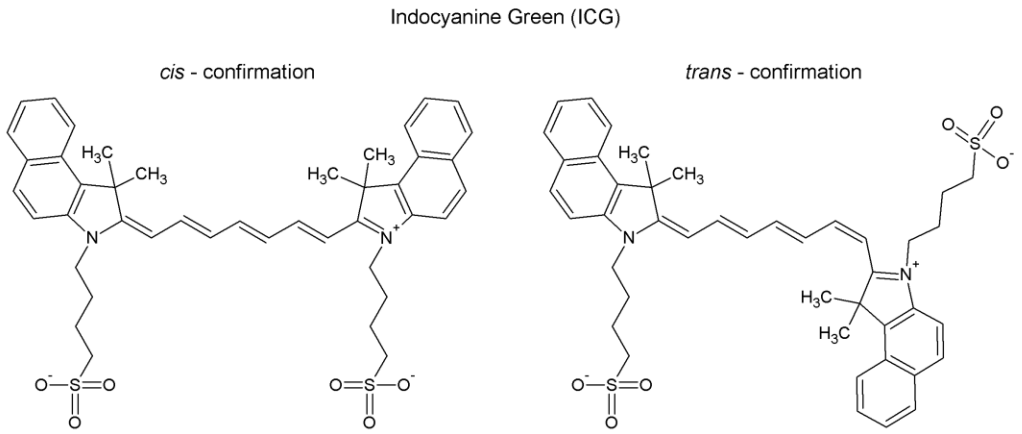


**Figure 3-3.**The *cis*/*trans* isomerization of indocyanine green is illustrated. The planar *cis* conformation structurally converts to the *trans*-configured isomer, for which the substituent groups orient in opposite directions, via a rotation about a double bond (C=C) of the polymethine chain.

### 3.3.3 Photodegradation

While the isomerization is reversible, in that the non-radiative relaxation restores the molecule to its original confirmation in preparation to repeat the photoexcitation cycle, other photo-induced structural modifications can lead to irreversible alterations that terminate the photoexcitation sequence, known as photodegradation. In aqueous solution, this is attributed to interactions with solvent radicals and ions leading to the formation of leucoforms – electrochemically reduced, non-fluorescent forms of the dye molecule.[27, 29] A significant ICG photodegradation process in particular is the photo-initiated [2+2]-cycloaddition of the polymethine chain (Figure 3-4).[36] Reactive species, such as singlet oxygen, can react with the double bonds of the polymethine length resulting in dioxetanes (Figure 3-4B).[37] These, in turn, fragment thermally to yield two non-fluorescent carbonyl products (Figure 3-4C). Reactive oxygen, and the self-sensitized degradation process for ICG, will be discussed in detail in Chapter 5. The rate constant for such photodegradation processes is termed $k_{PD}$.

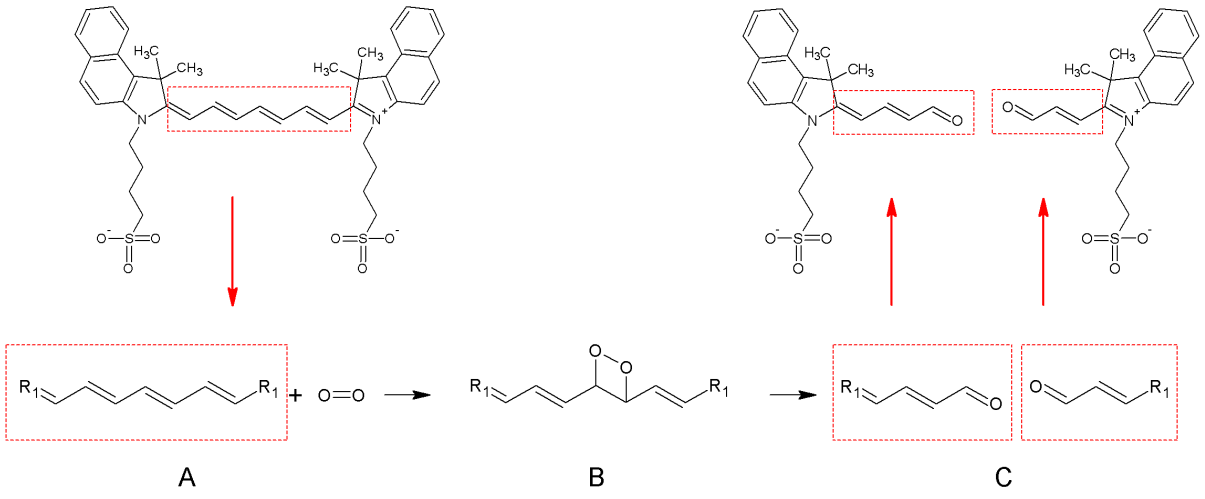


**Figure 3-4.**The [2+2]-cycloaddition photodegradation process in ICG is illustrated. (A) Reactive species such as $O_2$ molecules react with the alkenes of the polymethine chain of the fluorophore to (B) form dioxetanes ($C_2O_2H_4$) which, in turn, (C) thermally fragment to yield two non-fluorescent carbonyl leucoforms.

### 3.4 Enhancing ICG Optical Performance

The three abovementioned processes were described as additional relaxation pathways that can appreciably diminish the fluorescence intensity and contend with the rate of fluorescence emission in IGC. Therefore, the fluorescence quantum yield expression presented in Equation 3-1 is now adapted to include these significant non-radiative rate constants:

$$\Phi_F = \frac{\Gamma}{\Gamma + k_{nr} + k_Q + k_{Iso} + k_{PD}} \quad \text{[Eqn. 3-4]}$$

A second metric of fluorescent performance is the excited state lifetime of fluorescence, $\tau_0$*:*

$$\tau_0 = \frac{1}{\Gamma + k_{nr}} \quad \text{[Eqn. 3-5]}$$

The lifetime of the excited state is defined by the average time the molecule spends in the excited state prior to returning to the ground state. It is understood that shorter lifetimes result in higher incidences of total relaxation from the excited state. For simplicity, $k_{nr}$ represent all non-radiative rates, this time including the rates of quenching, photoisomerism, and photodegradation introduced in the previous sections. The excited state lifetime for ICG is 20 ± 5 ps in water.[11] The lifetime in absence of the non-radiative relaxation components is called the intrinsic or natural lifetime, and is given by:

$$\tau_n = \frac{1}{\Gamma} \quad \text{[Eqn. 3-6]}$$

This natural lifetime can be calculated from the measured lifetime ($\tau_0$) and quantum yield ($\Phi_F$):

$$\tau_n = \frac{\tau}{\Phi_F} \quad \text{[Eqn. 3-7]]}$$

For ICG, the intrinsic lifetime is calculated to be on the order of 700 ps. Thus, it is clear that the actual lifetime is significantly modified by factors that compete with the rate constant $\Gamma$ (the minor relaxation pathway), as $\tau_0$ is 35-fold shorter than $\tau_n$.

Unfortunately, sensitive, real-time *in vivo* imaging schemes require that a fluoroprobe emit a strong fluorescent signal (high $\Phi_F$), retain its performance in physiological environments (reduced $k_q$), and prolong signal intensity (no $k_{Iso}$ or $k_{PD}$).[38] Therefore, recent efforts have been undertaken to eliminate many of these unfavorable relaxation pathways in favor of promoting $\Gamma$. One of the significant advantages nanotechnology has brought to bioimaging is the capacity to improve various fluoroprobe molecules for *in vivo* applications.[38, 39] Perhaps the most promising attribute of fluorophore-doped particles is the improved photostability of the encapsulate by both the inhibition of unfavorable conformational reorganization[10] and reduced interactions with solvent molecules,[40] which avoid dynamic processes that result in non-radiative energy losses. The work presented in this chapter appraises the optical properties of ICG-encapsulating CPSNPs (ICG-CPSNPs) against the free fluorophore, with particular emphasis on any improvements afforded by way of a matrix-shielding effect of the calcium phosphosilicate carrier particles. Specifically, reductions in rotational relaxations, collisional quenching, and photodegradation are assessed in terms of fluorescence intensity, environmental stability, and excitation lifetime, respectively. Evaluation of the successful diminution of the non-radiative pathways is determined in terms of a quantum yield comparison between the free fluorophore and the composite ICG-CPSNPs.

## 3.5 Materials and Methods

### 3.5.1. Materials

All chemicals used in this work were purchased as described: dimethylsulfoxide (>99.9%, A.C.S. Reagent), Dulbecco's Modified Eagle's Medium, and ethylene glycol (99.8%, Anhydrous) from Sigma Aldrich (St Louis, MO); indocyanine green from TCI America

(Portland, OR); methanol (99.9+%, OmniSolv spectroscopic grade) from VWR International (West Chester, PA); ethyl alcohol (200-proof, Absolute, ACS/USP Grade) from Pharmco-AAPER (Brookfield, CT); 1,1′,3,3,3′,3′-hexamethylindotricarbocyanine iodide from Exciton (Dayton, OH); fetal bovine serum (35-010-CV, Regular) from Mediatech, Inc. (Manassas, VA). Water was deionized in our lab using a Millipore Milli-Q purification system (Billerica, MA), passed through a 200 nm filter, and boiled while flushing with argon to remove $CO_2$.

### 3.5.2 Optical Measurements

For all optical measurements, samples were placed in a low-volume fluorescence cuvette (9F-SOG-10-GL14-S; Starna Cells, Inc., Atascadero, CA), and held by a modified cuvette holder. Absorption spectra were recorded on a PerkinElmer Lambda 950 UV-Vis-NIR spectrophotometer (Perkin Elmer, Waltham, MA). The dye-doped particle absorption at 785 nm was compared to a standard curve of absorption vs. ICG concentration to identify the apparent encapsulate content, though not accounting for any optical matrix effects. Next, the release of the encapsulated fluorophore was induced with the addition of a 10:1 volume ratio of a $10^{-3}$ M solution of ethylenediaminetetraacetic acid (EDTA) to the particle suspension. EDTA is a chelating agent that sequesters the divalent $Ca^{2+}$ ion from the nanostructure, dissolving the calcium phosphosilicate particles. The 785 nm absorption value of the released ICG was compared to a second standard curve in an EDTA-salt solution, isotonic to the solvent environment after nanoparticle dissolution. This procedure gave the true fluorophore concentration encapsulated within the particles.

Fluorescence measurements were performed using custom-built collection optics connected via a fiber optic cable to an Ocean Optics HR-2000 USB spectrometer, with a resolution of 0.42 nm/pixel. Emitted radiation was collected at 90 degrees with a 10X microscope

objective (N.A. 0.3) coupled into the fiber optic cable. A high power 785 nm diode laser (450 $mW/cm^2$) was used as the excitation source (RL785; Renishaw plc, Gloucestershire, UK). Solvent influence was recorded on both free ICG and doped nanoparticle suspensions of comparable fluorophore content. Aliquots of each were diluted 1:10 into the test solvent and kept in the dark. Measurements were conducted precisely 10 minutes after the sample introduction.

### 3.5.3 Fluorescent Lifetime Measurements

The decay of the fluorescence with time for ICG was generated by recording the fluorescent spectra of both the free dye solution and doped nanoparticle suspension of equivalent fluorophore concentration at five second intervals under continuous illumination of the 785 nm laser. A set of measurements for each sample was conducted both at full laser power (100 mW) and at a reduced 11.6 mW power using an absorptive neutral density filter of +1.0 optical density (NE10A; Thor Labs, Newton, NJ). A 120 μL volume of each analyte was used to ensure simultaneous illumination over the entire analyte volume. Free ICG samples were diluted from the same $10^{-3}$ M stock solution. Measurements were recorded in duplicate using fresh solutions for each run.

### 3.5.4 Quantum Efficiency Determination

Quantum efficiency measurements were conducted following the comparative method of Williams *et al*.,[41] for which a reference sample with identical absorbance at the same excitation wavelength of the unknown analyte is assumed to absorb the same number photons as the latter, noting that the quantum efficiency of a material is largely independent of the wavelength used to excite the system.[42] Hence, the ratio of the integrated fluorescence intensities of the test solution

to the reference of known efficiency yields the ratio of the quantum efficiency values, provided they are recorded under identical conditions. Since $\Phi_F$ for the reference sample is known, the $\Phi_F$ for the test sample is readily calculated.[43] This comparative approach is numerically expressed by the equation:[42]

$$\Phi_{\mathrm{F}} = \Phi_{\mathrm{F},R} \frac{I}{OD} \frac{OD_R}{I_R} \frac{n^2}{n_R^2} \qquad \text{[Eqn. 3-8]}$$

where $\Phi_F$ is the fluorescent quantum efficiency, $I$ is the integrated emitted intensity collected (integrated over wavelength, proportional to the total number of photons emitted), $OD$ is the optical density (related to the total number of photons absorbed), $n$ is the refractive index of the solvent in which the molecules are dissolved, and the subscript $R$ denotes the values for the reference sample. The ratio of refractive indices, $\frac{n^2}{n_R^2}$, normalizes the effective solid angle of the collection optics by accounting for possible changes in the total emitted solid angle of light entering into the collection system for different samples due to differences in refraction caused by different solvent refractive indices, as shown in Figure 3-5.[42]

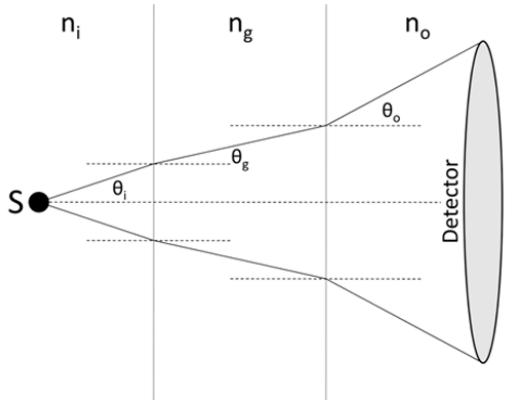


**Figure 3-5.** A schematic illustration of the change in the solid angle of emitted light as it travels towards a detector from the source (S). This change is due to differences in refraction ($\Theta$) caused by the different solvent refractive indices ($n_i$, $n_g$, $n_o$) through which the light propagates. Reproduced from Lakowicz (2006).[8]

It is useful to consider the relationship between *I* and *OD*. A sample absorption and emission scan for an ICG solution is shown in Figure 3-6A and B. If a series of optical density and integrated emitted intensity measurements are performed, then the resulting values can be plotted as shown in Figure 3-6C. In order to stay in the regime where Equation 3-8 is valid (the Beer's law regime), dye concentrations are chosen such that the optical density (measured at the excitation wavelength of 785 nm) is less than or equal to 0.25.[44, 45] The *x*-axis in Figure 3-6C corresponds to the optical density and the *y*-axis to the integrated emitted intensity. The intercept is taken to be at zero, because when there is no light absorbed, there should be no light emitted. Thus, the slope of the line obtained, proportional to the ratio of the number of photons emitted (*I*) to the number of photons absorbed (*OD*, in the Beer's law regime), corresponds to the fluorescent quantum efficiency.[43, 45]

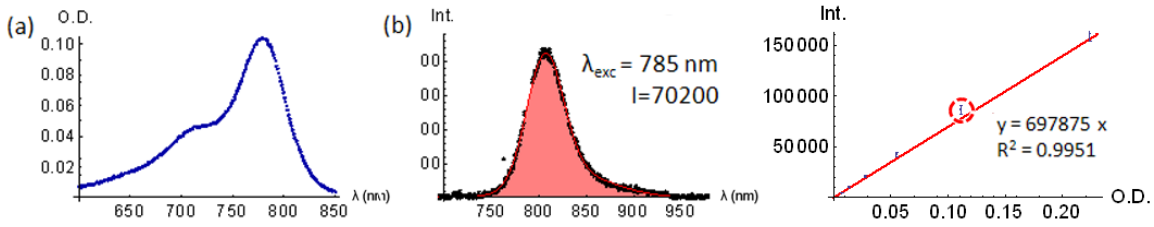


**Figure 3-6.** (A) Optical Density of $10^{-6}$ M ICG in 7:3 EtOH:$H_2O$ solution. The line at 785 nm shows the OD for this solution concentration used in the determination of the optical density-emission behavior as part of the calculation of $\Phi$. (B) Emitted intensity of the $10^{-6}$ M ICG solution at 785 nm excitation. The area under the curve is the integrated intensity *I*, and is the second component of the optical density-emission plot needed for Eqn. 3-11 for the calculation of $\Phi_F$. The missing points around 785 nm are the saturation due to the laser line. Here, the integrated intensity is ~70000. (C) Plot and linear fit of integrated emitted intensity vs. optical density for a range of solution concentrations. The circled data point represents the values obtained for the $10^{-6}$ M ICG concentration in panels (A) and (B). The slope of the fit, *I/OD*, is used for the calculation of $\Phi_F$ in Eqn. 3-11.

The reference fluorphore used as the known standard for fluorescent quantum yield measurements is the laser dye 1,1′,3,3,3′,3′-hexamethylindotricarbocyanine iodide (HITC; Exciton, Inc.; Dayton, OH). Solutions of free indocyanine green were prepared by dissolving the powder in either deionized water, a 7:3 volume mixture of ethanol and water, or 0.15 M

phosphate buffered saline (PBS, pH 7.4) prepared according to Dulbecco *et al*.,[46] while HITC was prepared in methanol. All solutions were prepared immediately before characterization to minimize specious bleaching of the dyes. Each measurement was conducted in duplicate on two separate occasions using freshly prepared stock solutions and a new set of standard data. This comparative quantum efficiency determination was developed for molecular systems, and as such, does not take into account scattering or attenuation influences characteristic of particulate suspensions. However, the measured values are presented as a conservative approximation of quantum efficiency for the encapsulated fluorophore, as adjustments for the attenuated light that actually reaches the encapsulated molecules within the highly scattering particle geometry are expected to show a larger fluorescent ratio and thus yield higher efficiency values than reported.

## 3.6 Results and Discussion

### 3.6.1 Emission Enhancement

The fluorescence spectrum of the dye-doped CPSNPs was compared to that of the corresponding free ICG dye under identical optical conditions (785 nm excitation). Figure 3-7 shows that the shape of both the absorption and emission curves are similar for free ICG and the doped nanoparticles in aqueous solution. This indicates that the encapsulation of the fluorophore within the rigid CPS matrix retains the monomeric state of the encapsulated ICG without deleterious structural[31-35] or chemical[8] alterations that adversely affect absorption and emission of the dye. These undesirable phenomena result in peak transformations or spectral shifts, respectively, which are not observed for the embedded ICG spectra. Additionally, the fluorescence emission intensity of one dye-doped CPSNP is approximately $10^3$ times that of one

ICG dye molecule. The enhanced brightness is similar to reports by Zhao *et al*. on fluorescent silica nanoparticles.[47]

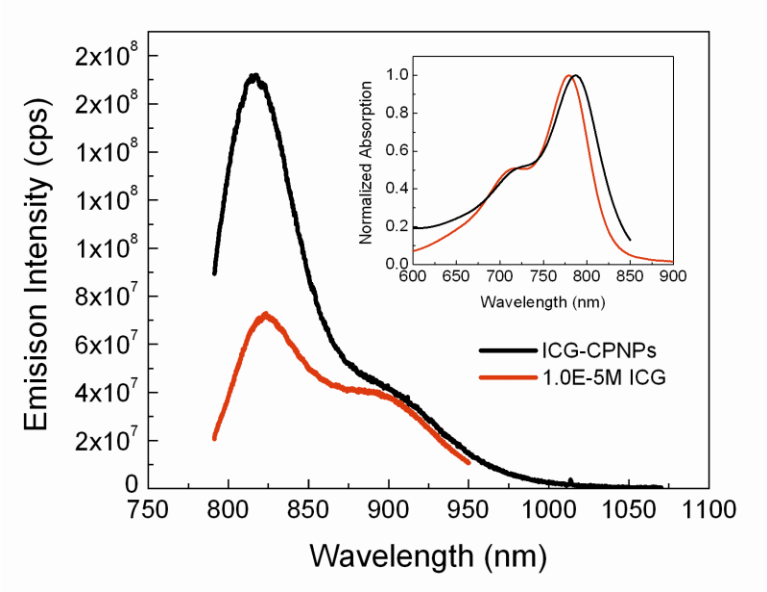


**Figure 3-7.** Absorption (inset) and fluorescence spectra of free ICG (red) and ICG-CPSNPs (black) in aqueous solution. The CPSNP suspension ($10^{13}$ particles/mL) had an apparent fluorophore content of roughly $10^{-5}$ M based on absorption standards; a matching concentration of free dye was used for the comparison. The shape and position of both the absorption and emission spectra are similar, indicating the absence of either chemical modification or dimerization upon encapsulating the dye in the calcium phosphosilicate matrix. Emission from the ICG-CPSNPs is significantly brighter than the matching free dye solution, which suffers from quenching interactions due, in part, to free dye self-aggregation.

This enhanced brightness is at least partly due to the nanoparticle architecture, with multiple dye molecules encapsulated in a single particle. Thus, brightness or intensity does not provide evidence that the encapsulation provides intrinsically different fluorescence performance than the free molecules. However, it is proposed that a consequence of the rigid installation of the embedded molecules within the CPSNPs is the restriction of the molecule to a planar conformation, inhibiting the possibility of rotational translation necessary for isomerization to

occur during the excited-state lifetime.[9] This effectually serves to eliminate the rotational non-radiative relaxation pathway, $k_{Iso}$, contributing in favor of radiative relaxation.

Figure 3-8 illustrates the static dimer and oligomer self-quenching events for free ICG that occur in aqueous solutions above 5 x $10^{-6}$ M at pH 7 and binary ethanol-water mixture above 3 x $10^{-6}$ M , resulting in the loss of further emission intensity. This quenching threshold is similar to that reported by Saxena *et al*. (2.6 x $10^{-6}$ M).[29] However, the comparatively elevated intensity from a $10^{-5}$ M concentration of fluorophore encapsulated with the CPSNP suspension (Figure 3-7) indicates that the molecules are uniformly distributed in their monomeric form and not self-aggregated within the calcium phosphosilicate matrix, physically isolating adjacent molecules from each other, even at high molar concentrations. This physical separation of encapsulates imparts a diminished incidence of self-quenching, $k_Q$, allowing the use of a greater number of fluorescing units for a brighter signal than is possible in the unencapsulated state.

### 3.6.2 Solvent Protection

The chemical stability of the encapsulated fluorophore was experimentally verified by analyzing fluorescence spectra as a function of solvent environment. The effect of four bio-relevant solvents (water, Dulbecco's modified Eagle's medium (DMEM), ethylene glycol, and dimethylsulfoxide (DMSO)) on the free ICG dye is shown in Figure 3-9A, with shifts in the normalized emission spectra dependent on the solvent environment. The positions of the maximum emission wavelengths have a standard deviation of 7.8 nm over an 18 nm spread.

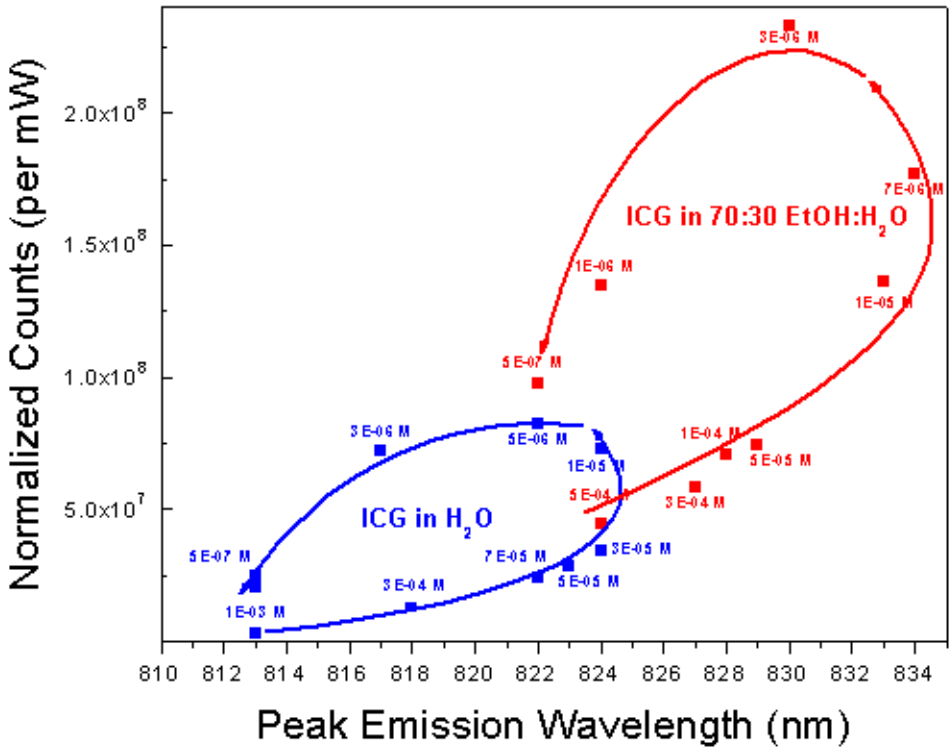


**Figure 3-8.** A map of the emission peak position and intensity of free ICG as function of concentration and solvent illustrates that ICG is prone to dimerizations that alter the absorption behavior (thus shifts in corresponding peak emission wavelength) and self-quenching effects on fluorescence intensity, that cap the emissive properties of the free fluorophore. The intensity values reported are normalized to the energy of the excitation beam.

These peak values experience a bathochromic shift toward longer wavelengths relative to the aqueous spectra due to a combination of general solvent influences[9] as well as specific solvent effects such as molecule-molecule interactions and hydrogen bonding that increase the quenching constant ($K$) and rate of collisional quenching mechanisms ($k_Q$).[8]

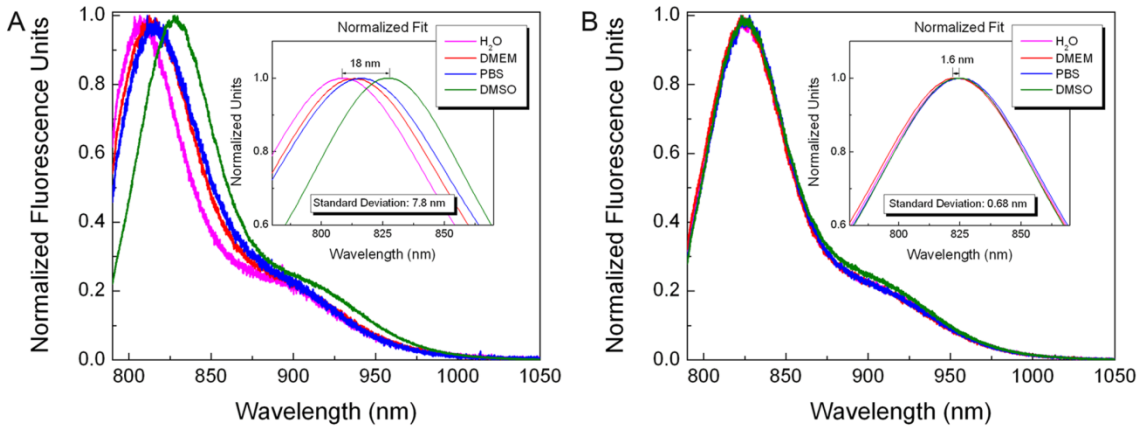


**Figure 3-9.** The comparative spectral effect of four bio-relevant solvents on the emission response of (A) free ICG dye and (B) dye-doped ICG-CPSNPs. The normalized peaks spread across 18 nm for the free fluorophore (standard deviation of 7.8 nm), while encapsulation in CPSNPs has an order of magnitude smaller 1.6 nm spread (0.68 nm standard deviation). This data confirms the largely impermeable nature of the CPS matrix to the surrounding environment, shielding the encapsulated dye from solvent interaction.

In contrast, the emission spectra for the encapsulated dye in CPSNPs are stable regardless of solvent environment. Figure 3-9B (peak standard deviation of 0.68 nm, 1.6 nm spread) highlights the solvent resilient nature of the encapsulated fluorophores molecules, which are shielded from solvent interactions and specific solvent-induced alterations. Such a shielding results in the reduction of the quenching constant; the solvent-impermeable ceramic shell encasing protects the fluorophores from interactive collisions with entities in the solvent environment, drastically reducing the overall rate of quenching.

### 3.6.3 Photostability

As described in section 3.3.3, photodegradation is often a consequence of chemical interactions in the excited state and is typically credited to a reaction between the fluorophore molecule and dissolved oxygen.[10] The physical positioning of the encapsulated ICG molecules

within the rigid matrix appears to resist structural alterations such as cycloadditions, as evidenced by a notable increase in the fluorescent half-life of the encapsulated dye versus the free dye when subjected to continuous illumination (Figure 3-10). An occurrence such as this is credited with a matrix shielding effect, allowing prolonged periods of excitation without significant degradation in emission intensity. Free ICG dye and doped CPSNPs were excited under continuous illumination from a diode laser (785 nm; 450 mW/cm$^2$) at comparable concentrations in PBS (pH 7.4) to mimic the physiological environment. Responses in Figure 3-10 show that CPSNP encapsulation yields an approximately 500 percent increase in emission half-life at a laser power significantly higher than typical clinical NIR imaging applications (5 to 50 mW/cm$^2$),[48] and even provides a 240 percent increase under extremely high laser power conditions (1000 mW/cm$^2$). Such performance can be ascribed to a decline in the rate of degradation processes, and thus a reduction in $k_{PD}$.

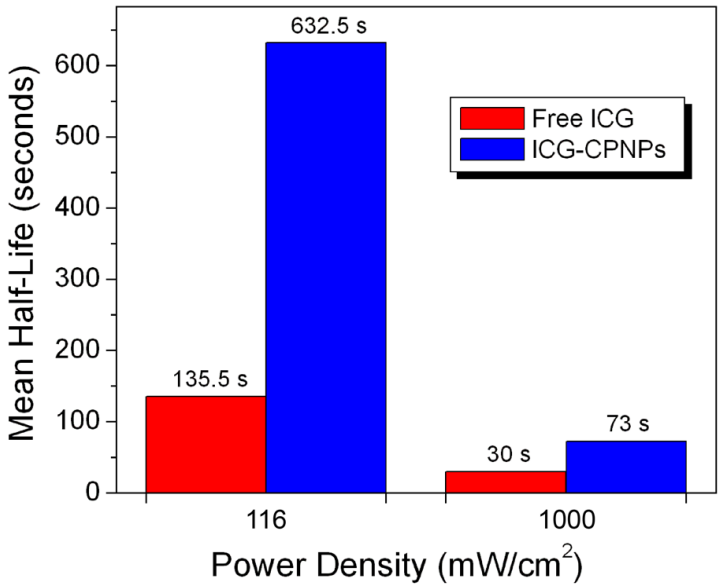


**Figure 3-10.** Fluorescent half-life for a free ICG fluorophore (red) and ICG-CPSNP (blue) suspension of matching absorption ($10^{-6}$ M) in PBS under 785 nm excitation at two power densities. Encapsulation provides an average of 470 percent increase in half-life at an excitation power commonly used in clinical settings (~100 mW/cm$^2$), and a 240 percent increase under even extremely high laser power density (1000 mW/cm$^2$).

### 3.6.4 Quantum Efficiency

Thus far, the physical presence of the rigid CPSNP encasing has demonstrated the ability to isolate the component fluorophore molecules from the external environment, separating them from any of the competing, non-radiative relaxation channels typically prone to ICG in solution and consequently reducing the respective rate constants of these pathways ($k_{Iso}$, $k_Q$, $k_{PD}$). Thus, the influence of encapsulation, or the matrix-shielding effect, can be defined as the attenuation of rotational, collisional, and degradation mediated relaxation pathways to the ground state that shorten the excited state lifetime of a fluorescent molecule. To gauge the influence this proposed effect has on overall optical performance, the fluorescence quantum yields in various environments are compared for the free and encapsulated fluorophores.

The *I* versus *OD* curves for HITC in methanol (known reference) and free (unencapsulated) ICG in two different solvents are shown in Figure 3-11A. The two solvents chosen for the ICG solutions are: (1) 7:3 EtOH:$H_2O$ by volume (the solvent for the as-synthesized nanoparticles) and (2) standard 0.15 M phosphate buffered saline (PBS, pH 7.4), which is a solvent often used in clinical and biological applications as a proxy that is isotonic to blood. The fluorescent quantum efficiencies for ICG in these solvents obtained using the comparative method with HITC in methanol as the reference ($\Phi_{F,R} = 0.28$) are $\Phi_{F,1} = 0.084 \pm 0.001$ for the EtOH:$H_2O$ solution and $\Phi_{F,2} = 0.027 \pm 0.001$ for PBS. The measured low $\Phi_F$ for ICG in high ionic strength environments, such as pH 7.4 PBS, epitomizes the interference effects of non-radiative contributions to excited-state relaxation. In such physiological environments, ICG is immediately muddled by the presence of complex molecules.[11] Physically-bound ground state dimers and oligomers that form act as quenching centers and modes of degradation of fluorescence intensity due to the energy transfer between excited and non-excited states.[49] Thus,

the reduced $\Phi_F$ in PBS of the free dye indicates an increase in non-radiative decay rates, $k_Q$ and $k_{PD}$, which significantly hinders the performance of ICG in physiological applications.

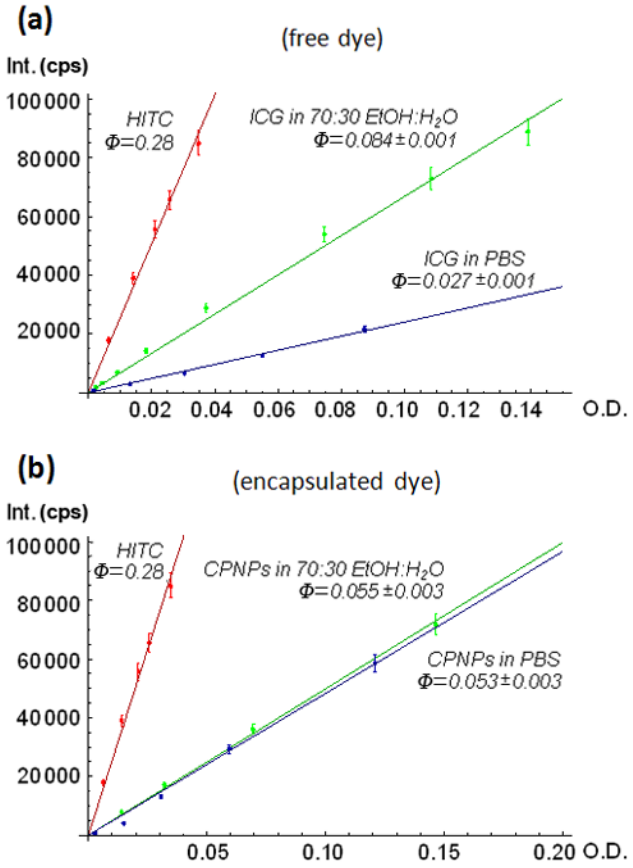


**Figure 3-11.** Plots of integrated emitted intensity vs. optical density for HITC (reference dye in MeOH, $\Phi_F$ = 0.28) and (A) free ICG in 7:3 EtOH:$H_2O$ and phosphate buffered saline ($\Phi_F$ = 0.084 and $\Phi_F$ = 0.027, respectively) and (B) ICG-doped CPS particles in 7:3 EtOH:$H_2O$ and phosphate buffered saline ($\Phi_F$ = 0.055 ± 0.003 and $\Phi_F$ = 0.053 ± 0.003, respectively). The $\Phi_F$ for ICG-CPSNPs in both solvents is identical to within the 95% confidence interval, verifying that the encapsulated ICG is shielded from the particle's external environment.

Identical experiments were conducted for suspensions of calcium phosphosilicate nanoparticles (CPSNPs) that contained ICG molecules. Figure 3-11B shows the emission versus optical density plots for these ICG encapsulating CPSNPs in the two different solvents (7:3 EtOH:$H_2O$ and PBS), the fluorescent quantum efficiencies for which are $\Phi_{F,1}$ = 0.055 ± 0.003 and $\Phi_{F,2}$ = 0.053 ± 0.003, respectively. The measured yields for each case are presented in Table 3-1.

The $\Phi_F$ for CPSNPs in PBS is 2-fold greater, attributed to the CPS matrix reducing the occurrence of non-radiative energy transfers. It is noteworthy that, in contrast to the free fluorophore, the fluorescent quantum efficiency obtained for a single particle is independent of the solvent environment ($\Phi_F$ values for the two solvents fall within overlapping 95% confidence intervals) – in essence, the calcium phosphosilicate comprising the nanoparticle becomes the "solvent" surrounding the fluorophore. Thus, the contribution of possible relaxation channels become characteristic to the particle, and therefore is consistent regardless of the greater solvent in which the CPSNPs are suspended. Furthermore, this result presents an objective explanation for the increased brightness from the ICG-CPSNPs relative to the free fluorophore. Thus, CPSNPs doped with ICG exhibit intrinsically greater brightness and enhanced $\Phi_F$ relative to the free dye for *in vivo* and *in vitro* applications.

**Table 3-1.** Fluorescence quantum efficiency ($\Phi_F$) values measured for free ICG and ICG-CPSNPs in two solvent environments (7:3 EtOH:$H_2O$ and PBS, pH 7). Values were determined via the comparative method with HITC in methanol as the reference.

| ***Solvent*** | ***$\Phi_F$ Free ICG*** | ***$\Phi_F$ ICG-CPSNPs*** |
|---|---|---|
| 7:3 EtOH: $H_2O$ | 0.084 ± 0.001 | 0.055 ± 0.003 |
| PBS (pH 7) | 0.027 ± 0.001 | 0.053 ± 0.003 |

## 3.7 Summary

Calcium phosphosilicate nanoparticles were used to encapsulate the near-infrared emitting fluorophore indocyanine green (ICG) as a new nanoparticulate-fluoroprobe for sensitive diagnostic imaging. The optical properties of these ICG-CPSNPs were demonstrated to be well suited for early stage *in vivo* tumor imaging in that encapsulation provided significantly better

optical properties compared to the free fluorophore. This improvement was realized through the elimination of specific non-radiative relaxation pathways indicative of ICG in solution (fluorescence quenching, photoisomerization, and photodegradation) that detrimentally shorten the excited state lifetime and, consequently, reduce the fluorescence quantum yield.

The rigid installation of the embedded molecules within the CPSNPs inhibits structural translations, thereby eliminating the translational non-radiative relaxation pathway of photoisomerization, ($k_{Iso} = 0$). By removing this competing decay channel, the internalized molecules afford a higher contribution to fluorescence, accounting partly for the significantly brighter emission intensity compared to a matching concentration of the free fluorophore. Additionally, fixing the internal molecules with the CPSNPs mitigates intermolecular associations that typically afflict aggregations and self-quenching behavior. This results in a lower contribution of the self-quenching aspect of $k_Q$. Thus, greater concentrations of ICG are exploitable for use in generating a higher emissive signal when encapsulated within CPSNPs, while the low quenching threshold around $10^{-5}$ M caps the efficiency of the unencapsulated fluorophore.

What is more, the physical boundary encasing the ICG molecules serves as a shield from effects by the surrounding solvent environment, protecting against dynamic collisional interactions that deactivate the excited state at the expense of radiative emission, and additional contribution to the reduced $k_Q$ rate of non-radiative decay. The ICG-CPSNPs were demonstrated to be solvent-resilient, imparting a consistent optical performance irrespective of solvent influences and environmental effects.

Furthermore, this matrix protection presents heightened fluorescence lifetimes, afforded by the deferred onset of degradation mechanisms of the internalized molecules. Specifically, the dye-doped CPSNPs exhibited a 4.7-fold longer fluorescent half-life at clinical imaging excitation

power ranges. In so doing, the magnitude of the rate of photodegradation ($k_{PD}$) is reduced in favor of radiative relaxation.

The inclusive effect of these individual alterations was established by the comprehensive fluorescence performance in the recognized ICG- depressing environment of PBS. Specifically, by removing or diminishing the influence of competing contributions of ICG excited state relaxation ($k_{Iso}$, $k_Q$, and $k_{PD}$), the encapsulated fluorophores are afforded a greater component to radiative relaxation, $\Gamma$, as evidenced by the 2-fold increase in quantum efficiency ($0.053 \pm 0.003$). The corollary to these properties is an increased brightness and prolonged signal intensity via the ICG-CPSNPs, assets that are vital for the sensitive diagnostic aspect of a theranostic modality.

## 3.8 Acknowledgments

The indispensable insights and guidance of the late Dr Peter Eklund of the Physics Department are greatly appreciated. His unmatched knowledge of photophysical processes and optics underlines the work presented. Also, the fluorescence experimentation would not have been possible if not for the assistance of Dr Tim Russin, without whom none of this work would have been possible. Particularly, Russin's critical involvement in assisting the design and implementation of the fluorescence lifetime and quantum efficiency experiments is acknowledged.

## 3.9 References

1. Malicka, J.; Gryczynski, I.; Geddes, C. D.; Lakowicz, J. R. Metal-Enhanced Emission from Indocyanine Green: A New Approach to in Vivo Imaging. *J. Biomed. Opt.* **2003,** *8*, (3), 472-478.
2. Schutt, F.; Fischer, J.; Kopitz, J.; Holz, F. G. Indocyanine Green Angiography in the Presence of Subretinal or Intraretinal Haemorrhages: Clinical and Experimental Investigations. *Clin. Exp. Ophthalmol.* **2002,** *30*, (2), 110-114.

3. Motomura, K.; Inaji, H.; Komoike, Y.; Kasugai, I.; Noguchi, S.; Koyama, H. Sentinel Node Biopsy Guided by Indocyanine Green Dye in Breast Cancer Patients. *Jpn. J. Clin. Oncol.* **1999,** *29*, (12), 604-607.
4. Ishihara, H.; Okawa, H.; Iwakawa, T.; Umegaki, N.; Tsubo, T.; Matsuki, A. Does Indocyanine Green Accurately Measure Plasma Volume Early after Cardiac Surgery? *Anesth. Analg.* **2002,** *94*, (4), 781-786.
5. Ott, P. Hepatic Elimination of Indocyanine Green with Special Reference to Distribution Kinetics and the Influence of Plasma Protein Binding. *Pharmacol. Toxicol.* **1998,** *82*, 1-48.
6. Paumgartner, G.; Probst, P.; Kraines, R.; Leevy, C. M. Kinetics of Indocyanine Green Removal from the Blood. *Ann. NY Acad. Sci.* **1970,** *170*, 134-147.
7. Caesar, J.; Shaldon, S.; Chiandussi, L.; Guevara, L.; Sherlock, S. The Use of Indocyanine Green in the Measurement of Hepatic Blood Flow and as a Test of Hepatic Function. *Clin. Sci.* **1961,** *21*, 43-57.
8. Lakowicz, J. R., *Principles of Fluorescence Spectroscopy*. 3rd ed.; Springer: Baltimore, MD, 2006.
9. Soper, S. A.; Mattingly, Q. L. Steady-State and Picosecond Laser Fluorescence Studies of Nonradiative Pathways in Tricarbocyanine Dyes - Implications to the Design of near-Ir Fluorochromes with High Fluorescence Efficiencies. *Journal of the American Chemical Society* **1994,** *116*, (9), 3744-3752.
10. Soper, S. A.; Mattingly, Q. L. Steady-State and Picosecond Laser Fluorescence Studies of Nonradiative Pathways in Tricarbocyanine Dyes: Implications to the Design of near-Ir Fluorochromes with High Fluorescence Efficiencies. *J. Am. Ceram. Soc.* **1994,** *116*, 3744-3752.
11. Philip, R.; Penzkofer, A.; Baumler, W.; Szeimies, R. M.; Abels, C. Absorption and Fluorescence Spectroscopic Investigation of Indocyanine Green. *J. Photoch. Photobio. A* **1996,** *96*, 137-148.
12. Benson, R. C.; Kues, H. A. Fluorescence Properties of Indocyanine Green as Related to Angiography. *Physics in Medicine and Biology* **1978,** *23*, (1), 159.
13. Yu, J.; Yaseen, M. A.; Anvari, B.; Wong, M. S. Synthesis of near-Infrared-Absorbing Nanoparticle-Assembled Capsules. *Chem. Mater.* **2007,** *19*, (6), 1277-1284.
14. Sevick-Muraca, E. M.; Houston, J. P.; Gurfinkel, M. Fluorescence-Enhanced, near Infrared Diagnostic Imaging with Contrast Agents. *Curr. Opin. Chem. Biol.* **2002,** *6*, (5), 642-650.
15. Yan, J.; Estevez, C.; Smith, J.; Wang, K.; He, X.; Wang, L.; Tan, W. Dye-Doped Nanoparticles for Bioanalysis. *Nano Today* **2007,** *2*, (3), 44-50.
16. Landsman, M. L. J.; Kwant, G.; Mook, G. A.; Zijlstra, W. G. Light-Absorbing Properties, Stability, and Spectral Stabilization of Indocyanine Green. *J. Appl. Physiol.* **1976,** *40*, (4), 575-583.
17. Desmettre, T.; Devoisselle, J. M.; Mordon, S. Fluorescence Properties and Metabolic Features of Indocyanine Green (Icg) as Related to Angiography. *Survey of Ophthalmology* **2000,** *45*, (1), 15-27.
18. Simmons, R.; Shephard, R. J. Does Indocyanine Green Obey Beer's Law? *J. Appl. Physiol.* **1971,** *30*, (4), 502-507.
19. Gathje, J.; Steuer, R. R.; Nicholes, K. R. K. Stability Studies on Indocyanine Green Dye. *J. Appl. Physiol.* **1970,** *29*, (2), 181-185.
20. Holzer, W.; Mauerer, M.; Penzkofer, A.; Szeimies, R. M.; Abels, C.; Landthaler, M.; Baumler, W. Photostability and Thermal Stability of Indocyanine Green. *J. Photoch. Photobio. B* **1998,** *47*, (2-3), 155-164.

21. Mordon, S.; Devoisselle, J. M.; Soulie-Begu, S.; Desmettre, T. Indocyanine Green: Physicochemical Factors Affecting Its Fluorescence in Vivo. *Microvasc. Res.* **1998,** *55*, (2), 146-152.
22. Maarek, J. M. I.; Holschneider, D. P.; Harimoto, J. Fluorescence of Indocyanine Green in Blood: Intensity Dependence on Concentration and Stabilization with Sodium Polyaspartate. *J. Photoch. Photobio. B* **2001,** *65*, (2-3), 157-164.
23. Mauerer, M.; Penzkofer, A.; Zweck, J. Dimerization, J-Aggregation and J-Disaggregation Dynamics of Indocyanine Green in Heavy Water. *Journal of Photochemistry and Photobiology B: Biology* **1998,** *47*, 68-73.
24. Kochubey, V. I.; Kulyabina, T. V.; Tuchin, V. V.; Altshuler, G. B. Spectral Characteristics of Indocyanine Green Upon Its Interaction with Biological Tissues. *Optics and Spectroscopy* **2005,** *99*, 560-566.
25. Zweck, J.; Penzkofer, A. Microstructure of Indocyanine Green J-Aggregates in Aqueous Solution. *Chemical Physics* **2001,** *269*, 399-409.
26. Altınoğlu, E. İ.; Russin, T. J.; Kaiser, J. M.; Barth, B. M.; Eklund, P. C.; Kester, M.; Adair, J. H. Near-Infrared Emitting Fluorophore-Doped Calcium Phosphate Nanoparticles for *in Vivo* Imaging of Human Breast Cancer. *ACS Nano* **2008,** *2*, (10), 2075-2084.
27. Holzer, W.; Mauerer, M.; Penzkofer, A.; Szeimies, R.-M.; Abels, C.; Landthaler, M.; Bäumler, W. Photostability and Thermal Stability of Indocyanine Green. *Journal of Photochemistry and Photobiology B: Biology* **1998,** *47*, 155-164.
28. Zhang, Y.; Wang, M. The Luminescent Properties and Photo-Decay of Sulfosalicylic Acid Doped Ormosils. *Mater. Lett.* **2000,** *42*, 86-91.
29. Saxena, V.; Sadoqi, M.; Shao, J. Degradation Kinetics of Indocyanine Green in Aqueous Solution. *J. Pharm. Sci.* **2003,** *92*, (10), 2090-2097.
30. Sanchez-Galvez, A.; Hunt, P.; Robb, M. A.; Olivucci, M.; Vreven, T.; Schlegel, H. B. Ultrafast Radiationless Deactivation of Organic Dyes: Evidence for a Two-State Two-Mode Pathway in Polymethine Cyanines. *Journal of the American Chemical Society* **2000,** *122*, 2911-2924.
31. Berezin, M. Y.; Lee, H.; Akers, W.; Guo, K.; Goiffon, R. J.; Almutairi, A.; Frechet, J. M. J.; Achilefu, S., Engineering Nir Dyes for Fluorescent Lifetime Contrast. In *31st Annual International Conference of the IEEE EMBS*, Minneapolis, MN, 2009; pp 114-117.
32. Arthurs, E. G.; Bradley, D. J.; Roddie, A. G. Picosecond Measurements of 3,3′-Diethyloxadicarbocyanine Iodide and Photoisomer Fluorescence. *Chemical Physics Letters* **1973,** *22*, 230-234.
33. Kuzmin, V. A.; Darmanyan, A. P. Study of Sterically Hindered Short-Lived Isomers of Polymethine Dyes by Laser Photolysis *Chemical Physics Letters* **1978,** *54*, 159-163.
34. Rentsch, S. K. Modeling of the Fast Photoisomerisation Process in Polymethine Dyes. *Chemical Physics* **1982,** *69*, 81-87.
35. Ponterini, G.; Momicchioli, F. Trans-Cis Photoisomerization Mechanism of Carbocyanines: Experimental Check of Theoretical Models *Chemical Physics* **1991,** *151*, 111-126.
36. Engel, E.; Schraml, R.; Maisch, T.; Kobuch, K.; König, B.; Szeimies, R.-M.; Hillenkamp, J.; Bäumler, W.; Vasold, R. Light-Induced Decomposition of Indocyanine Green. *Investigative Ophthalmology and Visual Science* **2008,** *49*, 1777-1783.
37. Rodriguez, V. B.; Henry, S. M.; Hoffman, A. S.; Stayton, P. S.; Li, X.; Pun, S. H. Encapsulation and Stabilization of Indocyanine Green within Poly(Styrene-Alt-Maleic Anhydride) Block-Poly(Styrene) Micelles for near-Infrared Imaging. *Journal of Biomedical Optics* **2008,** *13*, (1), 14025-1 - 14025-10.

38. Rao, J.; Dragulescu-Andrasi, A.; Yao, H. Fluorescence Imaging in Vivo: Recent Advances. *Curr. Opin. Biotech.* **2007,** *18*, 17-25.
39. Jin, S.; Ye, K. Nanoparticle-Mediated Drug Delivery and Gene Therapy. *Biotechnol. Progr.* **2006,** *23*, (1), 32-41.
40. Avnir, D.; Levy, D.; Reisfeld, R. The Nature of the Silica Cage as Reflected by Spectral Changes and Enhanced Photostability of Trapped Rhodamine 6g. *J. Phys. Chem.-US* **1984,** *88*, (24), 5956-5959.
41. Williams, A. T. R.; Winfield, S. A.; Miller, J. N. Relative Fluorescence Quantum Yields Using a Computer-Controlled Luminescence Spectrometer. *Analyst* **1983,** *108*, 1067-1071.
42. Lakowicz, J. R., *Principles of Fluorescence Spectroscopy*. 3rd ed.; Springer: New York, 2006; p xxvi, 954 p.
43. *A Guide to Recording Fluorescence Quantum Yields - Application Note*; Jobin Yvon Ltd.: Middlesex, UK, 1996.
44. Dhami, S.; Demello, A. J.; Rumbles, G.; Bishop, S. M.; Phillips, D.; Beeby, A. Phthalocyanine Fluorescence at High-Concentration - Dimers or Reabsorption Effect. *Photochemistry and Photobiology* **1995,** *61*, (4), 341-346.
45. Williams, A.; Winfield, S. A.; Miller, J. N. Relative Fluorescence Quantum Yields Using a Computer-Controlled Luminescence Spectrometer. *Analyst* **1983,** *108*, (1290), 1067-1071.
46. Dulbecco, R.; Vogt, M. Plaque Formation and Isolation of Pure Lines with Poliomyelitis Viruses. *Journal of Experimental Medicine* **1954,** *99*, (2), 167-182.
47. Zhao, X.; Bagwe, R. P.; Tan, W. Development of Organic-Dye-Doped Silica Nanoparticles in a Reverse Microemulsion. *Adv. Mater.* **2004,** *16*, (2), 173-176.
48. De Grand, A. M.; Frangioni, J. V. An Operational near-Infrared Fluorescence Imaging System Prototype for Large Animal Surgery. *Technol. Cancer Res. T.* **2003,** *2*, (6), 553-562.
49. Penzkofer, A.; Lu, Y. Absorption Behavior of Methanolic Rhodamine 6g Solutions at High-Concentration. *Chem. Phys.* **1986,** *107*, (2-3), 175-184.

# Chapter 4
# Functionalization of ICG-CPSNPs for Passive Localization and Direct Targeting of Disease for Diagnostic *In Vivo* Imaging

While the photophysical mechanisms presented in Chapter 3 elucidated the intrinsic handicap on the optical capacity of the fluorophore, there are also physical aspects of indocyanine green (ICG) behavior in physiological environments that limit the full potential for efficient long-term use during *in vivo* imaging applications. This chapter addresses the primary physical shortcomings experienced in such use environments, particularly rapid protein binding and premature clearance from circulation, as well as the absence of target selectivity. These characteristics are not representative of two major criteria for accurate extraction of precise diagnostic information: long circulation times, and targeted delivery. Calcium phosphosilicate nanoparticle (CPSNP)-based encapsulation of ICG will demonstrate improvements in both the physiological stability and targeting by virtue of the presence of a matrix encasing. Such progress for *in vivo* functioning will complement the previously described developments in optical performance realized at the photophysical level. The cooperation of these distinct performance improvements serves to enhance the absolute efficacy of this key near infrared (NIR) fluorophore for sensitive, long-term imaging. This, in turn, substantiates ICG-CPSNPs as a model optical diagnostics tool - the leading component of a theranostic modality.

## 4.1 Functionalization of ICG-CPSNPs to Improve *In Vivo* Pharmacokinetics

Despite the ICG molecule itself being well suited for diagnostic purposes in terms of biocompatibility, as it has no known metabolites[1] and presents a low incidence of adverse reactions,[2] it is still restricted from serving as the ideal theranostic fluorophore due to its poor

pharmacokinetic distribution behavior *in vivo*. The elevated rate of biological aggregation in solution is one of the main limitations of ICG for use in physiological mediums,[3] as it is the root cause of the notoriously short plasma half life (3-4 minutes)[4-6] that severely truncates the duration of functionality, an ill-fated characteristic for an agent intended for real-time tracking and imaging of a disease for diagnostic purposes.[7]

### 4.1.1 Physiological Limitations of ICG

The problem with ICG in physiological solutions arises from the high propensity for binding to serum proteins, including albumin and α-1-lipoproteins, stemming from the lipophilic character of the molecule.[4 3, 8, 9] In fact, it has been predicted that up to 98 % of the dye is bound to serum proteins upon intravenous administration.[1, 10] The previous chapter discussed the consequential non-radiative relaxations that affect fluorescence properties as a result of the collisional quenching and degradations related to such interactions. However, the more prominent drawback of such physical association *in vivo* is the untimely elimination of the fluorophore from circulation ahead of any extractable diagnostic data, primarily via the activity of the reticulum endothelial system (RES).[3, 8] Alternatively, unbound ICG is also swiftly removed from the vascular system by hepatic parenchymal cells of the liver, a consequence of the net anionic charge of the molecule, and transported into the bile for secretion.[5, 11]

Real-time fluorescent monitoring schemes require that a fluoroprobe retain its state of dispersion in physiological environments long enough to locate a site of interest. However, the clearance profile of ICG hinders both this ability to localize at an intended site, and, even upon localization, the short retention time *in vivo* limits the potential for practical diagnostics. Furthermore, ICG, like most fluorophore molecules, lacks tissue specificity, a function of great utility for disease-specific diagnosis.[12]

### 4.1.2 Improving Circulation Lifetimes via Surface PEGylation for Passive Localization

Sustaining circulation of a fluoroprobe by improving the plasma half life is realized by concealing the exogenous agent from the RES and eliminating untimely aggregations or sequestering. A reported approach to achieving this is via the passivation of the probe with polyethylene glycol (PEG) moieties, which is established to improve systemic retention and decrease immune-reactivity.[13, 14] The underlying motivation for prolonged circulation is the consequential passive location at solid tumor sites by exploiting the characteristics of tumor biology. It has been well demonstrated that macromolecules and small particles coated with PEG will eventually extravasate and accumulate in solid tumors when allowed sufficient circulation time,[15, 16] a phenomenon referred to as the enhanced permeability and retention (EPR) effect.[17-19] EPR has been attributed to two characteristic features of solid tumors: an increased density of blood vessels and a dysfunctional lymphatic drainage (Figure 4-1A).[20] The increased permeability of blood vessels, coupled with their leaky nature due to large interendothelial junctions, imperfect basement membranes, and large numbers of transendothelial channels, all of which are characteristic of rapid and defective angiogenesis, result in the passive accumulation of exogenous agents from circulaiton.[21] In addition, the inefficient lymphatic drainage of tumors fosters the retention of any accumulated agents.[20]

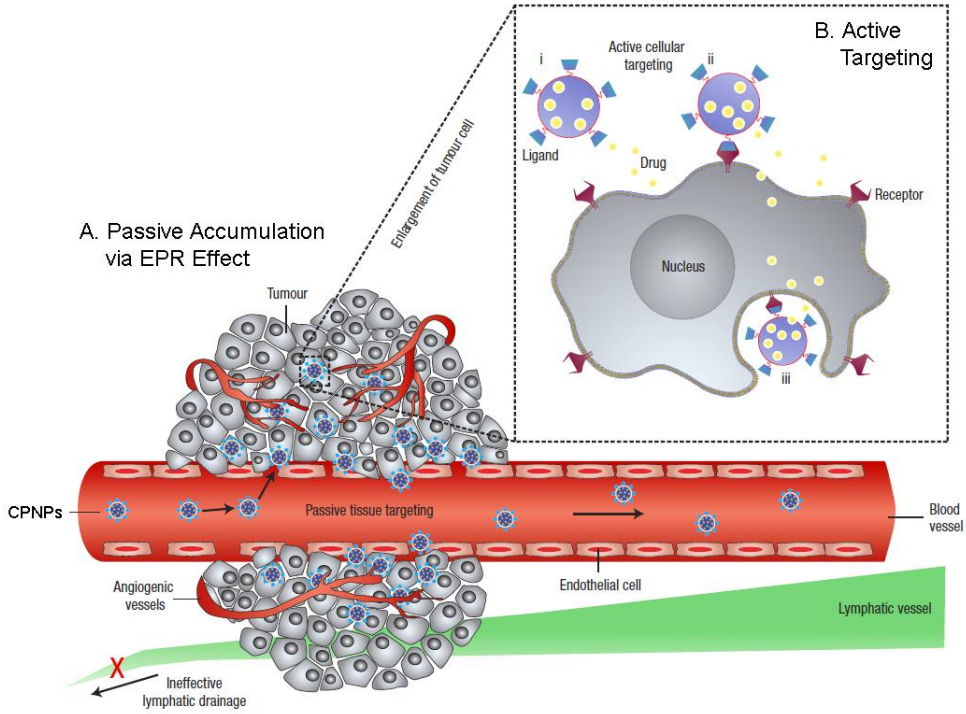


**Figure 4-1.**The schematic illustration represents the two modes of tumor targeting. (A) Passive localization occurs by combined effects of the extravasation of agents through increased permeability of the tumor vasculature and retention due to ineffective lymphatic drainage (EPR effect). (B) A possible mode of active targeting achieved by functionalizing the surface of nanoparticles with ligands that promote cell-specific recognition and binding. The agent can (i) attach to the membrane before (ii) being internalize into the cell. The illustration modified from Peer *et al*.[20]

### 4.1.3 Direct Targeting Approach

While EPR serves as an effective passive targeting strategy, the permeability of vessels may not be the same throughout a single tumor,[22] limiting the rate and effectiveness, and in some diseases, the occurrence of the EPR effect altogether.[20] Therefore, particular interest lies in the ability to actively target diseased cells by binding the agents to specific cells after extravasation, unambiguously denoting the presence of a certain disease. This direct agent-cell associating may be achieved by attaching targeting agents such as ligands (functionalizing) to the surface of the agent.[20] Prompted by ligand–receptor interactions, these functionalized agents localized at, and

eventually internalized within, the particular cells of interest (Figure 4-1B). What is more, direct targeting may also grant reduced localization times, as retention in the desired tissue would be actively initiated rather than simply a matter-of-chance based on inefficiencies of tumor vasculature, thereby condensing the timescale of the overall diagnostic protocol.

A prime model for which such direct targeting would profit is pancreatic cancer, a disease that is disreputably difficult to passively detect. The potential to actively target such cells in this manner stems from the prevalence of a specific gastrin hormone receptor within tissues associated with the disease, specifically the gastrointestinal and central nervous systems.[23-25] Gastrin binds to a family of G-protein-coupled receptors, also known as the cholecystokinin-2 ($CCK_2$ or CCK-B) receptor family.[25, 26] Intriguingly, $CCK_2$ receptor expression is often elevated in many cases of gastrointestinal cancer,[24, 27] including pancreatic cancer.[28] Therefore, it is thought that conjugation of such a moiety to the surface of an imaging probe (in this case the ICG-CPSNPs), would serve as the means for direct targeting of this challenging disease as a proof-positive diagnostic imaging tool.

## 4.2 Materials and Methods

### 4.2.1 Materials

All chemicals used in this work were purchased as described: indocyanine green (ICG) from TCI America (Portland, OR); methoxypolyethylene glycol amine (methoxyPEG-amine, HCl Salt MW 20kDa) and maleimie polyethylene glycol amine (maleimidePEG-amine, TFA Salt MW 5 kDa) from JenKem Technology USA (Allen, TX); ethyl-N-(3-dimethylaminopropyl)-N' hydrochloride carbodiimide (EDAC, Fluka BioChemika $\geq$99.0% AT); Dulbecco's Modified Eagle's Medium, Roswell Park Memorial Institute RPMI-1640 Media, and Paraformaldehyde

(Reagent grade) from Sigma Aldrich (St Louis, MO); fetal bovine serum (35-010-CV, Regular) from Mediatech, Inc. (Manassas, VA); Trypsin (soybean) and Antimycotic solution from Invitrogen (Carlsbad, CA); Phycoerythrin from eBioscience (San Diego, CA); IsolSol from Vedco (St. Joseph, MO).

### 4.2.3 Attachment of PEGamine to carboxylic acid functionalized CPSNPs

The as-synthesized ICG-CPSNPs with carboxylate surface functional groups (Chapter 2) were surface passivated with polyethylene glycol (PEG) via a secondary functionalization scheme. A 4 mL aliquot of the carboxylate-CPSNPs ($7 \times 10^{13}$ particles) were chemically conjugated with methoxypolyethylene glycol amine (mPEG-amine) through an ethyl-N-(3-dimethylaminopropyl)-N' hydrochloride carbodiimide (EDAC) reaction.[29] The sample was first stirred at 550 rpm on a combination magnetic stir/hot plate set to 50$^{o}$C. In a drop wise manner, 1 mL of EDAC (1 mg/mL) followed by 1 mL of mPEG-amine (10 mg/mL), both in aqueous solutions of $CO_2$-free DI water (pH 7), were added to the sample under continuous stirring. This concentration of PEG amounted to a calculated 6-fold excess for monolayer surface coverage of the CPSNPs. The particles were reacted for 15 hours at 50$^{o}$C to form amide linkages between the carboxylate surfaces and the amine-terminations on the PEG. The mixture was then filtered through a centrifuge filter (Microsep 100K Omega; Pall Life Science, East Hills, NY) at 5000 g for 2 minutes (Marathon 22K Centrifuge; Fischer Scientific, Pittsburgh, PA) to remove any excess EDAC and unreacted PEG.

### 4.2.4 Gastrin-10 Bioconjugation of CPSNPs

The conjugation of gastrin-10 to CPSNPs was accomplished via a PEG-maleimide coupling strategy based on work previously described by Sosabowski and colleagues.[30] In brief, a 9 mL aliquot of citrate-CPSNPs was first conjugated with maleimide polyethylene glycol amine (PEG-maleimide; JenKem Technology Inc.), through the identical EDAC fostered amide linkage scheme describe above (Section 4.2.3). The cysteine residue on the gastrin-10 peptide allows for covalent attachment to the maliimide. Thus, the gastrin-10 was added at a 5:1 molar excess to the PEGylated CPSNPs. This solution was incubated overnight at 4 °C, protected from light, to produce CPSNP-PEG-Gastrin-10.

### 4.2.5 Cell Culture Work

Human pancreatic cancer cells (BxPC-3; American Type Culture Collection, Manassas, VA) were cultured in RPMI-1640 supplemented with 10% FBS and 1% antibiotic/antimycotic solution. All cell cultures were maintained at 37°C and 5% $CO_2$. Cells were harvested by trypsin/EDTA detachment for subculture or tumor engraftment. All cell culture experimentation was conducted in collaboration with and within the facilities of the Pennsylvania State University College of Medicine (Hershey, PA).

### 4.2.6 Fluorescence Microscopy

BxPC-3 cancer cells were incubated with CPSNP-PEG-Gastrin-10 (targeted) or CPSNP-PEG (untargeted) followed by a media exchange. Cells were then fixed in 2% (w/v) paraformaldehyde, mounted onto glass slides, and visualized using a Nikon Eclipse E400

microscope through a 40X objective using a combination Nikon DAPI/FIT-C filter cube and recorded on a Nikon Coolpix 995 digital camera.

### 4.2.7 Flow Cytometry

BxPC-3 pancreatic cancer cells were detached from tissue culture-ware, surface Fc receptors blocked with appropriate IgG, incubated with specific antibodies (Phycoerythrin), and fixed in 2% (w/v) paraformaldehyde. Samples were analyzed on a BD$^{TM}$ LSR II flow cytometry system (BD Biosciences; San Jose, CA) housed within the Penn State College of Medicine Flow Cytometry Core, utilizing appropriate compensation controls. Data analysis was performed using BD Biosciences FACS Diva software.

### 4.2.8 *In Vivo* Animal Studies

Four to six week old female athymic nude mice (approximate weight of 15 grams) were purchased from Harlan (Indianapolis, IN). All animal manipulations were performed with sterile techniques at the Penn State College of Medicine, and were approved by the Pennsylvania State University Institutional Animal Care and Use Committee.

Human breast adenocarcinoma cells (MDA-MB-231; American Type Culture Collection, Manassas, VA**)** were cultured in DMEM supplemented with 10% fetal bovine serum (FBS). Exponentially growing cells were removed from the plate by trypsin/EDTA detachment, re-suspended in PBS, and injected subcutaneously into both the right and left flank of the nude mice at approximately $10^6$ cells per mouse. Tumors were allowed to grow to ~5 mm in diameter before the imaging trial was commenced.

For the orthotopic human pancreatic cancer model, mice were fully anesthetized with a mixture of ketamine-HCl (129 mg/kg) and xylazine (4 mg/kg) injected intramuscularly. A small incision was made in the left flank, the peritoneum was dissected and the pancreas exposed. Using a 27-gauge needle, $1x10^6$ BxPC-3 cells (BxPC-3; American Type Culture Collection, Manassas, VA), cultured as above (Section 4.2.6) were prepared in 100 μL of Hank's balanced salt solution and injected into the pancreas. All orthotopic tumors were allowed to establish for one week prior to experimentation.

### 4.2.9. *In Vivo* Whole Animal Imaging

*In vivo* imaging and pharmacokinetic distribution experiments were conducted on athymic nude mice implanted with MDA-MB-231 xenografts (as above). The animal subjects were divided into four test groups each set to receive a systemic injection of one of four different samples: as-synthesized ICG-CPSNP-Carboxylate, ICG-CPSNP-PEG, Ghost-CPSNP-Carboxylate (without a fluorescent encapsulate), and a $10^{-4}$ M solution of free ICG in deionized $H_2O$ (pH 7). The latter two groups served as controls and designed to roughly match the estimated concentration of CPSNPs ($10^{13}$ particles/mL) and ICG content ($10^{-5}$ M) in the injected solutions, respectively. Equivalent ICG concentrations were determined prior to injection via absorption spectroscopy ($2x10^{-6}$ M prior to dilution). A 200 μL volume of each sample was injected into the tail veins of the mice.

Prior to whole animal imaging, anesthesia was induced and maintained by inhalation of 5% IsolSol in 100% oxygen. Each mouse was positioned flat on its abdomen side-by-side for simultaneous imaging. Near-infrared transillumination images (755 nm excitation, 830 nm emission, 3 minute exposure) and corresponding X-ray (1 second exposure) images were obtained with a Kodak In Vivo FX whole animal imaging station (Carestream Health; Rochester,

NY). This anesthesia and imaging procedure was repeated for each time point over a period of 96 hours. The imaging studies were conducted on 20 mice for a total sample size of five (n = 5).

Direct targeting of orthotopic pancreatic cancer was evaluated in a similar manner. Athymic mice were surgically implanted with BxPC-3 pancreatic cells as described in section 4.2.9. Two tests groups received systemic tail vein injections of either ICG-CPSNP-PEG or ICG-CPSNP-PEG-Gastrin-10. Each animal was imaging in the same manner as described for the *in vivo* biodistribution and passive localization experiments on breast cancer described above.

The associated NIR fluorescence image-X-Ray image pairs from both studies were merged to illustrate the fluorescence signal distribution relative to anatomy. All NIR images were pseudocolored and merged using Kodak MI imaging software (v.4; Kodak, Rochester, NY). Signal intensities were evaluated using the same software.

## 4.3 Results and Discussion

### 4.3.1 Verification of Surface Passivation with PEG

Citrate functionalized surfaces of the as-synthesized CPSNPs (Chapter 2) served as the platform for PEGylation and consequent bioconjugation. Changes in the surface charge were used to substantiate the surface chemistry modifications via zeta potential analysis. Figure 4-2 shows the zeta potential distribution of CPSNP-Carboxylate at pH 7 prior to any surface modifications (blue line). These CPSNP-Carboxylate display a negative mean zeta potential value of -29 $\pm$ 3 mV, as reported in Chapter 2. The terminal group of the methoxy-PEG holds no net charge at the same physiological pH. Thus, under the assumption that full surface coverage of these CPSNPs with PEG would mask the negative charge, zeta potential distributions of the CPSNP-PEG were examined (red). The distribution of charges after PEGylation has clearly shifted away from the

net negative charge of the original surfaces towards a net zero charge characteristic of the PEG molecules (+3.0 ± 2.0 mV). The surface charge of gastrin-10 conjugated CPSNPs was also examined, which showed an additional shift in distribution towards a more net positive surface charges (+6 ± 3.2 mV; violet).

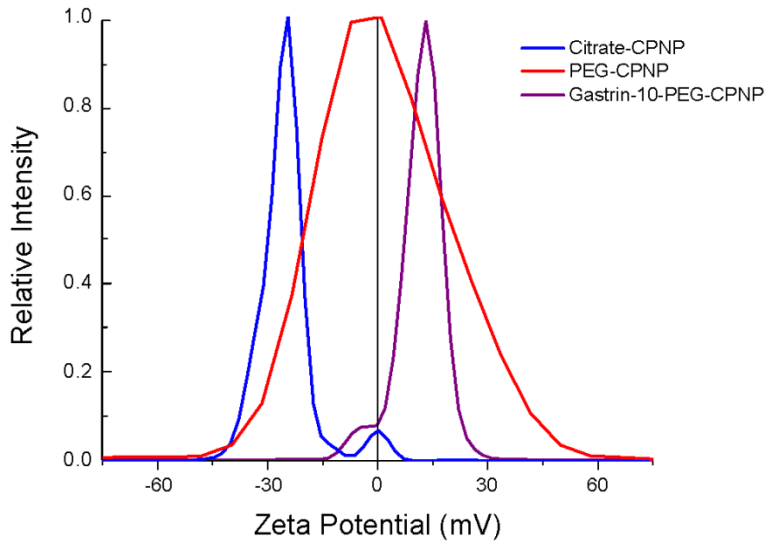


**Figure 4-2**. Zeta potential distributions of CPSNP suspensions of various functionalities in 7:3 EtOH:$H_2O$ (pH 7). The zeta potential of an as-synthesized suspension of citrate-functionalized CPSNPs is -29 ± 3 mV (blue), consistent with the carboxylate ($COO^-$)-termination. Upon PEGylation of the surface, the distribution of charges clearly shifts away from the net negative charge of the original surfaces towards a net zero charge (3 ± 2 mV; red) characteristic of the PEG molecules. The broadened distribution is characteristic of measurements of zero charge. The surface charge of gastrin-10 conjugated CPSNPs was also examined, which showed an additional shift in distribution towards a more net positive surface charges (+6 ± 3.2 mV; violet).

### 4.3.2 *In Vivo* Pharmacokinetic Distribution and Tumor Localization in Nude Mice

A NIR whole animal imaging approach was used to investigate the *in vivo* pharmacokinetic distribution of ICG-CPSNPs in nude mice. Figure 4-3 reveals the fluorescence signal and intensity distribution as a function of time for ICG-CPSNPs delivered systemically via tail vein injections. Two different surface functionalities of CPSNPs were evaluated, as-

synthesized carboxylate surface termination, and particles surface coated with polyethylene glycol (PEG) (Figure 4-3 series iii). The *in vivo* behavior of the ICG-CPSNP samples were compared to two controls: a sample of carboxylated ghost CPSNPs without a fluorescent encapsulate (series i) and free ICG of equivalent absorption (series ii). The fluorescence signals from the ICG-encapsulating CPSNPs *in vivo* are significantly prolonged compared to the free fluorophore; no detectable signal was recorded from the free ICG at 24 hours after injection (Figure 4-3B). In fact, fluorescence signals were completely lost after an average of only six hours. This significantly shorter *in vivo* fluorescence of the free dye is attributed to the fluorescence quenching in physiological environments [5, 6, 31-34] and rapid aggregation and clearance from the body as discussed above.[5, 6] In contrast, the ICG-CPSNPs retained significant fluorescence signals even after 4 days (Figure 4-3C).

The lipophilic character of ICG means it is readily taken up by hepatic parenchymal cells where it is then secreted into the bile.[5] This clearance pathway is consistent with the observations of initial hepatic localization (mid-region, Figure 4-3A) and eventual total clearance through the biliary tree with minimal acute renal involvement. Figure 4-3D illustrates excised organs 24 hours after systemic injection of ICG-CPSNP-PEG, affirming the hepatobiliary clearance with detectable signals along the gastrointestinal route. The hepatobiliary clearance mechanism offers yet another unique advantage of the calcium phosphosilicate nanoparticles. The lack of long term accumulation within the liver, as well as minor renal imaging, suggests minimal potential for hepatic or renal toxicology. Moreover, the lack of brain imaging suggests that barriers, such as the blood brain barrier, are relatively impermeable to the carboxylate- or PEG-coated CPSNPs.

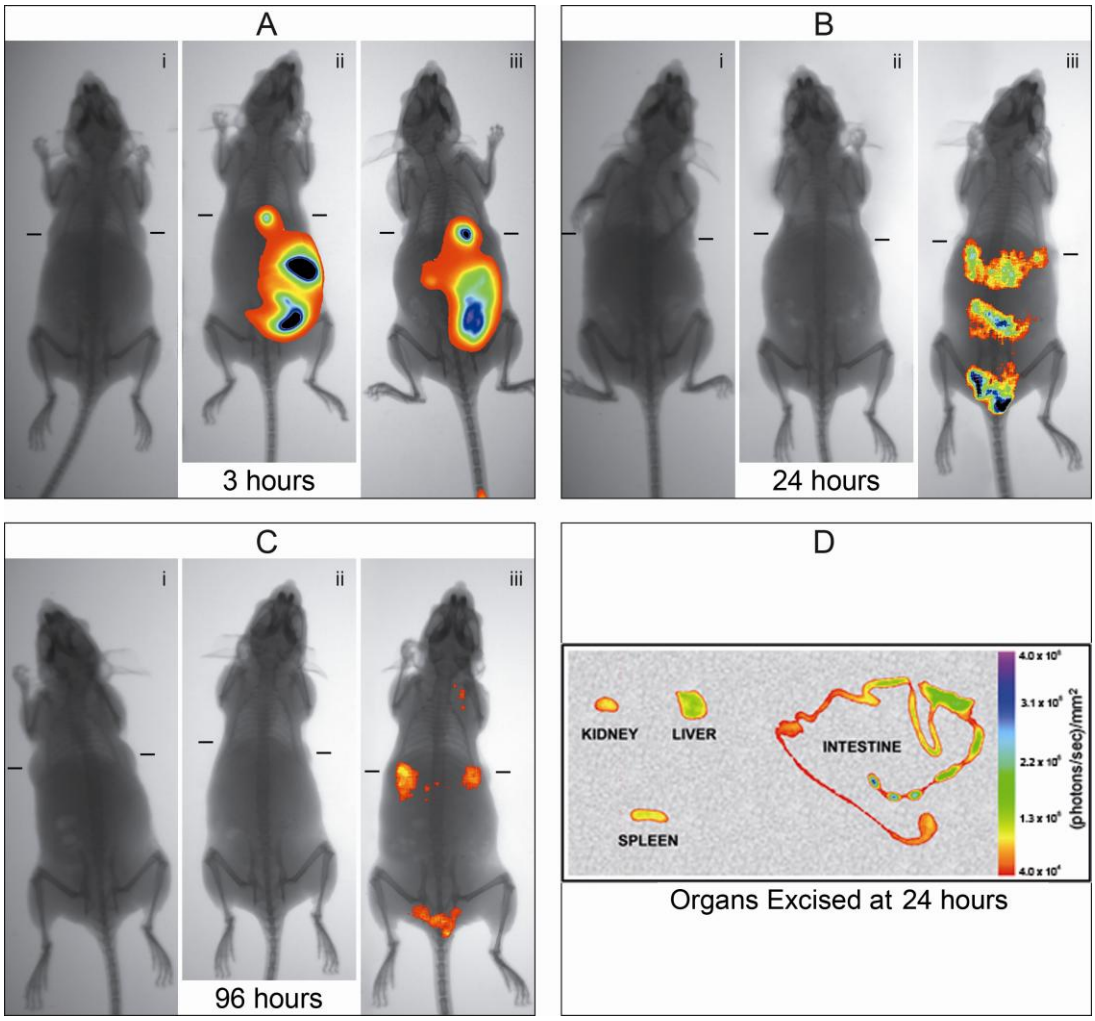


**Figure 4-3.** NIR transillumination images (Ex. 755 nm, Em. 830 nm) taken at various times (A – 3 hours, B – 24 hours, and C – 96 hours) track fluorescence signals and pharmacokinetic distributions for the ICG-CPSNPs and controls delivered systemically via tail vein injections in nude mice implanted with subcutaneous human breast adenocarcinoma tumors. Hash marks next to each mouse indicate the position of the 5 mm tumors. Two control samples (i) carboxylate-terminated CPSNPs without ICG encapsulant and (ii) free ICG, match the particle concentration and fluorophore content ($10^{13}$ particles/mL and $10^{-5}$ M, respectively) of a (iii) PEGylated ICG-CPSNP sample. (Bii) No fluorescence signal is detected from the free ICG at 24 hours post injection while the ICG-CPSNP-PEG sample (Ciii) retains significant signal even after 96 hours. (Biii) The fluorescence signal is unmistakably localized in tumors 24 hours after administration with PEGylated ICG-CPSNPs. The excised organs in panel (D) illustrate the biliary clearance route 24 hours post-injection of ICG-CPSNP-PEG. Fluorescence signal is not seen from the stomach with minimal renal involvement.

A comparison of signal intensity localized within the liver and along the hepato-gastrointestinal tract at the 3 hour time point (Figure 4-3A) shows a lower concentration of ICG-CPSNPs undergoing hepatic uptake and bile secretion relative to the free dye control, further confirming that a greater concentration of ICG-CPSNP remains in circulation than free dye, prolonging the circulation of the fluorescent probes and underlining the additional advantage afforded by the CPSNP encapsulation. The longer *in vivo* retention times permit the particles (and thus the fluorescent signal) to indirectly collect in the breast cancer tumors via the passive EPR mechanism previously discussed. Figure 4-3B shows that the PEGylated ICG-CPSNPs accumulate in the two subcutaneous tumors within 24 hours after injection, which is consistent with previously reported improvements in circulation half-lives for PEGylated quantum dots[14] and EPR tumor accumulation periods for PEGylated gold nanoshell particles.[16] The carboxylate functionalized CPSNPs also showed distinct tumor localization (data not shown), but at significantly lower signal intensities than the PEGylated particles. The *in vivo* imaging studies were replicated in 5 separate groups of mice.

These initial data provide strong evidence that CPSNP-encapsulation of ICG is sufficient for *in vivo* shielding to provide prolonged fluorescence emission over 4 days post systemic injection without the incidence of protein binding and rapid clearance characteristic of unencapsulated ICG. Furthermore, time series animal imaging shows that PEGylated CPSNPs have sustained *in vivo* circulation that allows the exploitation of the EPR effect and provides passive localization and tumor retention that is crucial for diagnostic imaging applications.

### 4.3.3 Evaluation of BxPC-3 Pancreatic Cell Targeting by Gastrin Receptor-Targeted CPSNPs

Attention is now turned to improving cell specificity by way of direct targeting. As a model system, an orthotopic human pancreatic cancer model was used. Increased surface expression of gastrin receptors on pancreatic cells and tumors was targeted by CPSNPs coupled via a PEG linker to a short gastrin peptide (CPSNP-PEG-Gastrin-10). BxPC-3 human pancreatic cancer cells were treated *in vitro* with either targeted CPSNP-PEG-Gastrin-10 or untargeted CPSNP-PEG. Experimental parameters included a five or 60 minute incubation, and either the replacement of media or no media change. Cells were fixed and visualized using a fluorescence microscope. It should be noted that for compatibility with the fluorescence system, both groups of CPSNPs were synthesized to encapsulate the visible fluorophore fluorescein (Ex 495 nm, Em 520 nm) in place of ICG, since filter set and detector of the instrument used is not setup for NIR wavelengths. All other synthesis parameters were identical to those presented for ICG-CPSNP syntheses in Chapter 2. *In vitro* behavior is not expected to be different between the two CPSNP systems, as the only variable, the fluorophore, is sequestered within the particles and isolated from influencing physiological interactions.

Only BxPC-3 cells exposed for 60 minutes to CPSNP-PEG-Gastrin-10 with no media exchange displayed fluorescent staining (Figure 4-4A). Intriguingly, the observed fluorescence was green and blue, indicative of the pH-dependent degradation of CPSNPs as they internalize to the endosomal-lysosomal pathway, and release the encapsulated dye. Fluorescein displays a complex pH-dependent equilibrium and emission from its two fluorescent ionic forms, the monoanion and dianion.[35, 36] In higher pH environments, such as that in the CPSNPs and physiological solutions, the significant emission wavelength is from the dianion (peak excitation 495 nm, green). As pH drops below 6.5, the molecule is protonated into its monoanionic form which is excited in the blue (450 nm). Thus, emission signals from the fluorescein- encapsulating

CPSNPs shift from green toward blue as they experience the pH drop characteristic of the endosomal-lysosomal pathway into the cells, resulting in the dissolution of the particles and release of the fluorophore into the lower pH environment of late stage endosomes, as previously introduced in Chapter 2. The efficacy of direct targeting was also evaluated via flow cytometry (Figure 4-4B). These results further corroborated that CPSNP-PEG-Gastrin-10 (60 minutes exposure) successfully target BxPC-3 cells while untargeted CPSNP-PEG within the same time frame do not.

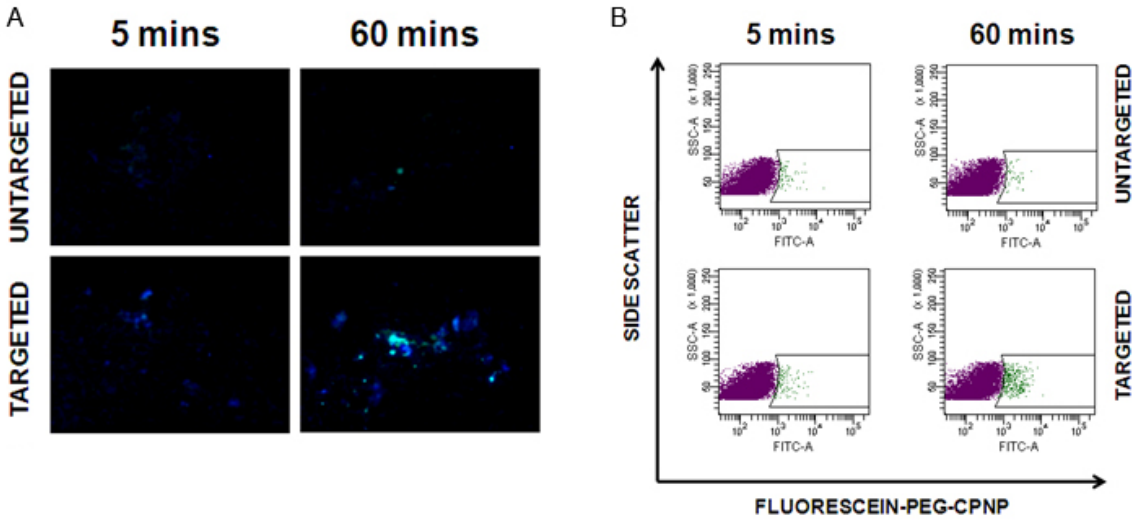


**Figure 4-4.** Gastrin receptor-targeted CPSNPs effectively targeted human BxPC-3 pancreatic cancer cells. BxPC-3 cells were exposed to fluorescein-loaded untargeted PEG-CPSNPs, or Gastrin-10-PEG-CPSNPs, for 5 minutes followed by exchange to fresh media for 55 minutes, or exposure for 60 minutes. (A) Cells were fixed and visualized by microscopy. (B) Cells were fixed and analyzed by flow cytometry with graphs representing 10,000 collected events per sample.

### 4.3.4 Evaluation of Pancreatic Cancer-Targeted CPSNPs *In Vivo*

The examination of direct targeting was extended to an *in vivo* system. It was found that the untargeted CPSNP-PEG effectively accumulated 24 hours post-tail vein injection within small BxPC-3 tumors in the pancreas (Figure 4-5A), and these whole animal images were confirmed by

excision of the pancreas (Figure 4-5B). This corroborates the passive localization via the EPR effect with ICG-CPSNP-PEG presented in the breast cancer model in Section 4.3.2.

However, CPSNP-PEG-Gastrin-10 targeted particles proved to be much more successful at targeting the pancreatic tumors (Figure 4-5A), including peritoneal extensions of the primary tumor, as well as the brain which is also rich in gastrin receptors.[25] Direct targeting of the CPSNP-PEG-Gastrin-10 to the brain was confirmed by excising and imaging the brain during necropsy (Figure 4-5B). It is noteworthy that the untargeted CPSNP-PEG did not display any significant brain-accumulation in this study, once again, reiterating the results from the earlier breast cancer study.

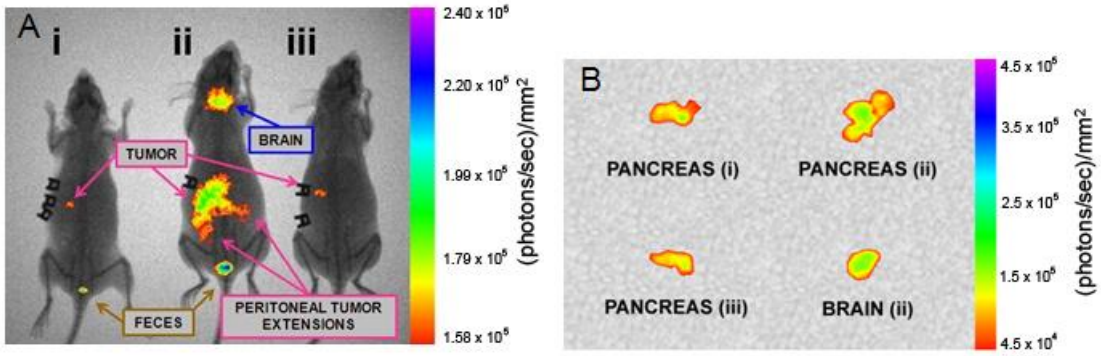


**Figure 4-5.** Targeting gastrin receptors in an *in vivo* orthotopic-tumor model of pancreatic cancer. Human BxPC-3 pancreatic cancer cells were xenografted orthotopically into athymic nude mice. (A) One week following engraftment, ICG-loaded CPSNPs were administered systemically via tail vein injection and near-infrared images were taken 24 hours post-injection. From left to right, mice receiving: (i) untargeted ICG-CPSNP-PEG, (ii) targeted CPSNP-PEG-Gastrin-10. Series (iii) is a third conjugation system not pertinent to the discussion of this work. (B) Excised, tumor-bearing, pancreases from each mouse and excised brain (mouse ii). All images are representative of at least four independent experiments.

## 4.4 Summary

The demonstrated physiological distributions and emission lifetime extension of PEGylated ICG-CPSNPs *in vivo* are well suited for early stage tumor imaging and diagnostics. The *in vivo* emission signal stability from encapsulated ICG was compared to the free fluorophore after systemic administration. Near infrared (NIR) whole animal imaging was employed to map the emission signals. The duration of fluorescent signal from the encapsulated fluorophore was clearly extended, as emission was still resolvable up to four days post-injection. On the other hand, signal was lost within 12 hours from the unencapsulated dye. The presence of the encapsulating matrix thus provides a means for long-term imaging and sensitive tracking applications using ICG.

Aside from the photophysical quenching processes presented in the previous chapter, this abrupt loss in emission from the free fluorophore is attributed to the incidence of high protein binding and prompt clearance characteristics of ICG in physiological systems. The lipophilicity of the fluorophore results in its rapid uptake by hepatic parenchymal cells of the liver, leading to a complete hepatobiliary clearance from the system. This was visually confirmed by a marked signal intensity localized to the gastrointestinal region of the animals immediately after administration, as well as the dissection of associated organs of this biliary clearance route. Examination of the corresponding images for the ICG-CPSNPs revealed that a reduced signal was emitted from this same region, implying that only a minor concentration of fluorphore was sequestered into this clearance pathway, amounting in a greater portion of the administered agent lingering in circulation. Such evasion of untimely clearance provides a longer time for function, and in turn, enables higher precision diagnostics.

Once improved physiological function was established, attention was turned to targeting the emission signal to specific sites of interest in accordance with the proposed diagnostic

element of the imaging protocol. The surfaces of the ICG-CPSNPs were successfully coated with polyethylene glycol (PEG), as evidenced by a masked surface charge and a net neutral zeta potential distribution shift. Comparing the pharmacokinetic behavior of the PEGylated ICG-CPSNPs to the original negatively charged carboxylate-terminated CPSNPs revealed that ICG-CPSNP-PEG were able to passively localize within the solid breast adenocarcinoma tumor xenografts within 24 hours of systemic administration. This observation is consistent with other reports of surface passivation by PEG. The capacity to passively localize at tumor sites is a consequence of the prolonger circulation lifetimes afforded by the PEG-coated particle. PEGylation has been reported to extend systemic retention by decreasing immune-reactivity, setting the stage for direct targeting possibilities for precise tissue selectivity.

An effective diagnosis that readily differentiates tissue types necessitates the accurate and precise detection of specific cells. To impart tissue specificity, the ICG-CPSNP-PEG were bioconjugated with gastrin-10 with the intention of specifically binding a model pancreatic tumor cell line, BxPC-3, which is known to over express the receptor for this hormone. An Initial *in vitro* assessment acknowledged the faculty of this functionalization to preferentially target the cells of interest relative to the untargeted ICG-CPSNP-PEG. Fluorescence microscopy visually revealed this targeting capacity, while flow cell cytometry explicitly characterized the preferential cellular uptake of the CPSNP-PEG-Gastrin-10 by BxPC-3 pancreatic cancer cells.

A NIR whole animal imaging study further revealed that gastrin functionalization does in fact provide a direct means for targeting orthotopic pancreatic tumors, with emission signal intensities from excised tumors measuring higher relative to the controls. However, the *in vivo* study also highlighted the expression of gastrin receptors in numerous other cell types associated with the gastrointestinal system, which were also consequently targeted by the imaging probe. While this exposed the unanticipated potential for gastrin-functionalized CPSNPs to cross the blood-brain barrier, expanding the utility to various gliobastomas or neurodegenerative diseases,

it also emphasized the necessity for selection of a more distinctive target to increase tissue selectivity and thus impart the highest diagnostic precision.

Nevertheless, the work presented in this chapter has clearly highlighted the capacity of ICG-CPSNPs to evade untimely clearance and prolong systemic circulation through surface PEGylation. Furthermore, a model direct targeting scheme using CPSNPs has been successfully demonstrated, underlining the capacity for this nanoparticle-based imaging probe to provide the high selectivity needed for the most effective diagnostic imaging.

## 4.5 Acknowledgements

The invaluable efforts of the Dr Mark Kester research group of the Penn State Hershey College of Medicine's Department of Pharmacology are graciously acknowledged. In particular, the original efforts of James Kaiser involving the initial whole animal imaging experiments must be recognized. Also, all animal manipulations and cell culture work, including *in vitro* fluorescent microscopy, flow cell cytometry, and targeted *in vivo* imaging studies, were possible thanks to Dr Brian Barth and Sriram Shanmugavelandy of the Kester group. Further recognition is extended to Dr Jill Smith's group of the Department of Medicine for their lead on all pancreatic cancer studies. The specific contributions of Chris McGovern and Dr Gail Matters on the orthotopic animal model and gastrin-10 target are further appreciated.

## 4.6 References

1. Engel, E.; Schraml, R.; Maisch, T.; Kobuch, K.; König, B.; Szeimies, R.-M.; Hillenkamp, J.; Bäumler, W.; Vasold, R. Light-Induced Decomposition of Indocyanine Green. *Investigative Ophthalmology and Visual Science* **2008,** *49*, 1777-1783.
2. Hope-Ross, M.; Yannuzzi, L. A.; Gragoudas, E. S.; Guyer, D. R.; Slakter, J. S.; Sorenson, J. A.; Krupsky, S.; Orlock, D. A.; Puliafito, C. A. Adverse Reactions Due to Indocyanine Green. *Retina* **1995,** *15*, 76-80.

3. Gomes, A. J.; Lunardi, L. O.; Marchetti, J. M.; Lunardi, C. N.; Tedesco, A. C. Indocyanine Green Nanoparticles Useful for Photomedicine. *Photomedicine and Laser Surgery* **2006,** *24*, 514-521.
4. Mordon, S.; Devoisselle, J. M.; Soulie-Begu, S.; Desmettre, T. Indocyanine Green: Physicochemical Factors Affecting Its Fluorescence in Vivo. *Microvascular Research* **1998,** *55*, 146-152.
5. Desmettre, T.; Devoisselle, J. M.; Mordon, S. Fluorescence Properties and Metabolic Features of Indocyanine Green (Icg) as Related to Angiography. *Surv. Ophthalmol.* **2000,** *45*, (1), 15-27.
6. Mordon, S.; Devoisselle, J. M.; Soulie-Begu, S.; Desmettre, T. Indocyanine Green: Physicochemical Factors Affecting Its Fluorescence in Vivo. *Microvasc. Res.* **1998,** *55*, (2), 146-152.
7. Abels, C. Targeting of the Vascular System of Solid Tumours by Photodynamic Therapy (Pdt). *Photochemical and Photobiological Sciences* **2004,** *3*, (765-771).
8. Keller, E.; Ishihara, H.; Nadler, A.; Niederer, P.; Seifert, B.; Yonekawa, Y.; Frei, K. Evaluation of Brain Toxicity Following near Infrared Light Exposure after Indocyanine Green Dye Injection. *Journal of Neuroscience Methods* **2002,** *117*, 23-31.
9. Muckle, T. J. Plasma Proteins Binding of Indocyanine Green. *Biochem. Med.* **1976,** *15*, (1), 17-21.
10. Paumgartner, G.; Probst, P.; Kraines, R.; Leevy, C. M. Kinetics of Indocyanine Green Removal from the Blood. *Annals of the New York Academy of Sciences* **1970,** *170*, 134-147.
11. Yaseen, M. A.; Yu, J.; Wong, M. S.; Anvari, B. Stability Assessment of Indocyanine Green within Dextran-Coated Mesocapsules by Absorbance Spectroscopy. *Journal of Biomedical Optics* **2007,** *12*, 064031-1-8.
12. Rao, J.; Dragulescu-Andrasi, A.; Yao, H. Fluorescence Imaging in Vivo: Recent Advances. *Curr. Opin. Biotech.* **2007,** *18*, 17-25.
13. Altınoğlu, E. İ.; Russin, T. J.; Kaiser, J. M.; Barth, B. M.; Eklund, P. C.; Kester, M.; Adair, J. H. Near-Infrared Emitting Fluorophore-Doped Calcium Phosphate Nanoparticles for *in Vivo* Imaging of Human Breast Cancer. *ACS Nano* **2008,** *2*, (10), 2075-2084.
14. Ballou, B.; Lagerholm, B. C.; Ernst, L. A.; Bruchez, M. P.; Waggoner, A. S. Noninvasive Imaging of Quantum Dots in Mice. *Bioconjugate Chem.* **2004,** *15*, (1), 79-86.
15. Kong, G.; Braun, R. D.; Dewhirst, M. W. Hyperthermia Enables Tumor-Specific Nanoparticle Delivery: Effect of Particle Size. *Cancer Res.* **2000,** *60*, (16), 4440-4445.
16. James, W. D.; Hirsch, L. R.; West, J. L.; O'Neal, P. D.; Payne, J. D. Application of Inaa to the Build-up and Clearance of Gold Nanoshells in Clinical Studies in Mice. *J. Radioanal. Nucl. Ch.* **2007,** *271*, (2), 455-459.
17. Matsumura, Y.; Maeda, H. A New Concept for Macromolecular Therapeutics in Cancer Chemotherapy: Mechanism of Tumoritropic Accumulation of Proeins and the Antitumor Agent Smancs. *Cancer Research* **1986,** *46*, 6387-6392.
18. Maeda, H. The Enhanced Permeability and Retention (Epr) Effect in Tumor Vasculature: The Key Role of Tumor-Selective Macromolecular Drug Targeting. *Advan. Enzyme Regul.* **2001,** *41*, 189-207.
19. Maeda, H.; Fang, J.; Inutsuka, T.; Kitamoto, Y. Vascular Permeability Enhancement in Solid Tumor: Various Factors, Mechanisms Involved and Its Implications. *Int. Immunopharmocol* **2003,** *3*, 319-328.
20. Peer, D.; Karp, J. M.; Hing, S.; Farokhzad, O. C.; Margalit, R.; Langer, R. Nanocarriers as an Emerging Platform for Cancer Therapy. *Nature Nanotechnology* **2007,** *2*, 751-760.

21. Dvorak, H. F.; Nagy, J. A.; Dvorak, J. T.; Dvorak, A. M. Identification and Characterization of the Blood Vessels of Solid Tumors That Are Leaky to Circulating Macromolecules. *Am. J. Pathol.* **1988,** *133*, (1), 95-109.
22. Jain, R. K. Barriers to Drug Delivery in Solid Tumors. *Scientific American* **1994,** *271*, 58-65.
23. Smith, J. P.; Fantaskey, A.; Liu, G.; Zagon, I. S. Identification of Gastrin as a Growth Peptide in Human Pancreatic Cancer. *Am J Physiol* **1995,** *268*, R135-R141.
24. Smith, J. P.; Stock, E. A.; Wotring, M. G.; McLaughlin, P. J.; Zagon, I. S. Characterization of the Cck-B/Gastrin-Like Receptor in Human Colon Cancer. *Am J Physiol.* **1996,** *271*, R796-R805.
25. Wank, S. A.; Pisegna, J. R.; de Weerth, A. Brain and Gastrointestinal Cholecystokinin Receptor Family: Structure and Functional Expression. *Proc. Natl. Acad. Sci. U.S.A.* **1992,** *89*, (18), 8691-5.
26. Kopin, A. S.; Lee, Y. M.; McBride, E. W.; Miller, L. J.; Lu, M.; Lin, H. Y.; Kolakowski, L. F., Jr.; Beinborn, M. Expression Cloning and Characterization of the Canine Parietal Cell Gastrin Receptor. *Proc. Natl. Acad. Sci. U.S.A.* **1992,** *89*, 3605-3609.
27. Smith, J. P.; Shih, A. H.; Wotring, M. G.; McLaughlin, P. J.; Zagon, I. S. Characterization of Cck-B/Gastrin-Like Receptors in Human Gastric Carcinoma. *Int. J. Oncol.* **1998,** *12*, 411-419.
28. Smith, J. P.; Liu, G.; Soundararajan, V.; McLaughlin, P. J.; Zagon, I. S. Identification and Characterization of Cck-B/Gastrin Receptors in Human Pancreatic Cancer Cell Lines. *Am. J. Physiol.* **1994,** *266*, R277-R283.
29. Sharma, R. K.; Das, S.; Maitra, A. Surface Modified Ormosil Nanoparticles. *J. Colloid Interf. Sci.* **2004,** *277*, (2), 342-346.
30. Sosabowski, J.; Lee, M.; Dekker, B.; Simmons, B.; Singh, S.; Bereford, H.; Hagan, S.; McKenzie, A.; Mather, S.; Watson, S. Formulation Development and Manufacturing of a Gastrin/Cck-2 Targeting Peptide as an Intermediate Drug Product for Clinical Imaging Study. *Eur J Pharm Sci.* **2007,** *31*, 102-111.
31. Landsman, M. L. J.; Kwant, G.; Mook, G. A.; Zijlstra, W. G. Light-Absorbing Properties, Stability, and Spectral Stabilization of Indocyanine Green. *J. Appl. Physiol.* **1976,** *40*, (4), 575-583.
32. Simmons, R.; Shephard, R. J. Does Indocyanine Green Obey Beer's Law? *J. Appl. Physiol.* **1971,** *30*, (4), 502-507.
33. Gathje, J.; Steuer, R. R.; Nicholes, K. R. K. Stability Studies on Indocyanine Green Dye. *J. Appl. Physiol.* **1970,** *29*, (2), 181-185.
34. Maarek, J. M. I.; Holschneider, D. P.; Harimoto, J. Fluorescence of Indocyanine Green in Blood: Intensity Dependence on Concentration and Stabilization with Sodium Polyaspartate. *J. Photoch. Photobio. B* **2001,** *65*, (2-3), 157-164.
35. Sjoback, R.; Nygren, J.; Kubista, M. Absorption and Fluorescence Properties of Fluorescein. *Spectrochim Acta A* **1995,** *6*, (51), L7-L21.
36. Lakowicz, J. R., *Principles of Fluorescence Spectroscopy*. 3rd ed.; Springer: Baltimore, MD, 2006.

# Chapter 5

# Singlet Oxygen Generation from ICG Encapsulating CPSNPs: Evaluating the Prospect of Photosensitization for Photodynamic Therapy

As the second component to the simultaneous theranostic technology, ICG-CPSNPs are proposed to concurrently serve as a photosensitizing agent in a photodynamic therapy (PDT) modality. As introduced in Chapter 1, PDT is a growing alternative in cancer treatment which is based on the deliberate activation of photosensitizing chemicals that prompt a localized and minimally insidious therapy.[1]This chapter evaluates the capacity of ICG-CPSNPs to generate reactive singlet oxygen through a photodynamic process, a definitive element in their appraisal as a viable mode for point-of-care theranostics.

## 5.1 The Photodynamic Process

The photodynamic process involves the combination of a photo-active agent (the photosensitizer) and light of a wavelength matching the absorption spectrum of said agent. Once excited to a higher energy level, the photosensitizer undergoes intersystem crossing that renders the molecule in a triplet state, from which therapeutic photoactive products are generated prior to relaxing back to the ground state. Each individual step in this cycle is examined below.

The process initiates in the same manner as the radiative emission for fluorescence imaging presented in Chapter 2 – hence arises the opportunity for a single vector to simultaneously serve two distinct tasks as a bifunctional modality. In review, upon absorption of a photon of appropriate energy, the molecule is raised from the ground state ($S_0$) to an electronic excited state ($S_1$). In addition to the assorted relaxation pathways presented in Chapter 2 (radiative

and non-radiative), the excited molecule in the $S_1$ state can also undergo a spin conversion to populate the lowest energy triplet state ($T_1$). This conversion of $S_1$ to $T_1$ is termed intersystem crossing (ISC) and is a result of an energy transfer with a heavy atom or triplet oxygen molecule, such that:[2, 3]

$$S_0 \xrightarrow{h\nu} S_1 \xrightarrow{k_{ISC}} T_1$$

where $k_{ISC}$ is the rate of internal conversion. The Jablonski diagram first presented in Chapter 2 is extended in Figure 5-1 to include the ISC pathway and subsequent triplet state processes.

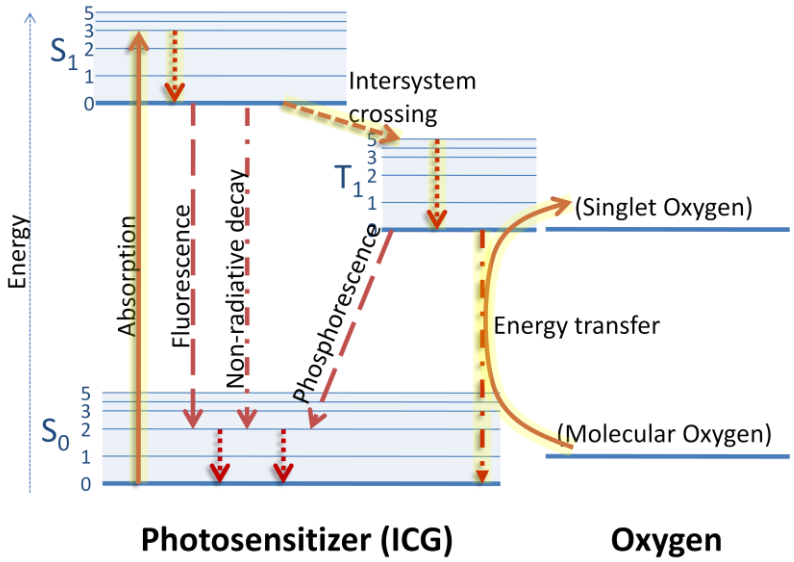


**Figure 5-1.** A simple Jablonski diagram highlighting (yellow) the processes involved in the photoexcitation of molecular ground state oxygen to a biologically active singlet state ($^1O_2$) that serves as the initiating element of photodynamic therapy. The excited singlet state of the photosensitizer is transferred to an excited triplet via an intersystem crossing pathway, from which energy is relaxed back to the ground state through a collisional energy transfer with a proximal oxygen molecule.

Analogous to the fluorescent quantum efficiency, where the fraction of radiative events is compared to all possible relaxation pathways from $S_1 \rightarrow S_0$ (Chapter 2), the quantum efficiency of $T_1$ formation, $\Phi_T$, is given by:

$$\Phi_T = \frac{k_{ISC}}{k_{ISC} + k_\Gamma + k_{nr}} \quad \text{[Eqn. 5-1]}$$

where this time the fraction of $k_{ISC}$ is included in the expression and weighed against the other deactivation processes of the singlet state, $k_\Gamma$ and $k_{nr,}$ the rate constants for fluorescence and all non-radiative channels, respectively.[4] It is evident from this ratiometric evaluation that each deactivation process is interrelated; the incidence of a given pathway can only improve at the expense of the others. This is an important note to consider when evaluating an agent designed to accomplish multiple processes. Unlike a dedicated fluorophore or photosensitizer, where the respective incidences of fluorescence or ISC would be enhanced by arresting the opposing energy transfer or radiative emission, respectively, an agent charged to function in both regards must exhibit sufficient incidences of both $k_\Gamma$ and $k_{ISC}$. Thus, in this unique case, the ideal molecule is not one that yields a quantum efficiency of unity in any one function, but a sufficient compromise between the two to meet the desired utility.

Just like the excited singlet state, the triplet state is metastable and favors energy relaxation back down to the molecular ground state. However, $T_1$ states have a relatively longer intrinsic lifetime due to the fact that, unlike the $S_1$ to $S_0$ deactivation, spontaneous conversion form this state requires an additional spin flip, which is a forbidden transition and thus kinetically unfavored. As a result, the rate constants for triplet emission are several orders of magnitude smaller than those for fluorescence from $S_1$; the deferred radiative emission from the $T_1$ state is termed phosphorescence.[5]

Alternatively, since the triplet states are usually long lived ($10^{-3}$-10 s),[2, 6] energy in $T_1$ is more likely to be quenched to $S_0$ by one of two non-radiative relaxation pathways: (1) a single-electron charge transfer (type I reaction) with some proximate molecule to form an exciplex, or (2) an energy transfer (type II reaction) to a ground state acceptor. Both type I and type II reactions can lead to the generation of reactive species of therapeutic utility; charge transfer

initiates a free radical intermediate through hydrogen-atom abstraction or electron-transfer between the excited sensitizer and a molecule. This radical can react with oxygen to form reactive oxygen species (ROS). On the other hand, energy transfer between a colliding excited sensitizer and a ground state triplet oxygen acceptor directly generates singlet state oxygen ($^1O_2$), a non-radical yet highly reactive form that reacts with many biological molecules.[7-12] Figure 5-2 illustrates these various processes. It is not always clear which mechanism is dominant, though considerable evidence now exists that energy transfer to molecular oxygen is the principal mediator of biological damage in PDT.[11, 13, 14] The sensitizer-mediated generation of singlet oxygen, from absorption by an agent molecule to the energy transfer from its $T_1$ state, is highlighted in Figure 5-1, with the later process described as:[15]

$$T_1 + {}^3O_2 \xrightarrow{k_{en}} S_0 + {}^1O_2$$

where again, $S_0$ represents the singlet ground state, $T_1$ the first excited triplet state, $k_{en}$ the rate constant of energy transfer, $^3O_2$ is the ground state triplet oxygen, and $^1O_2$ the singlet oxygen.

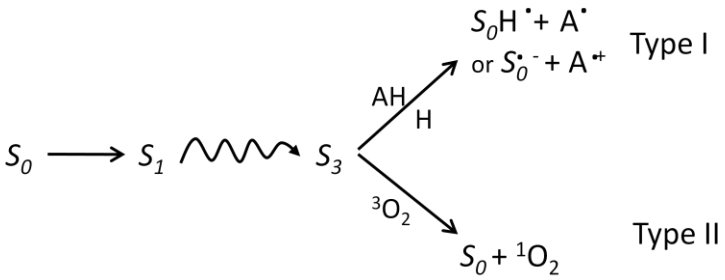


**Figure 5-2.** Schematic illustration of the two possible photochemical reactions for the relaxation of an excited triplet state photosensitizer ($S_3$); Type 1 sensitizers initiate radical reactions through either electron or hydrogen atom abstraction and can proceed in the absence of molecular oxygen. In Type 2 reactions, molecular oxygen is involved and can react with the $S_3$ in a spin-conserved reaction to regenerate the ground-state sensitizer and form $^1O_2$.

### 5.1.1 Singlet Oxygen

The highly reactive behavior of excited state $^1O_2$ is a reflection of the unique electronic structure of its ground state.[16] Molecular oxygen is comprised of two bound oxygen atoms, each with six outer electrons, leading to the electronic configuration:

$$O_2KK(2\sigma_g)^2(2\sigma_u)^2(3\sigma_g)^2(1\pi_u)^4(1\pi_g+)(1\pi-_g+)$$

The molecular orbital (MO) diagram is presented in Figure 5-3. Notably, the diradical ground-state $O_2$ has two electrons in two separate degenerate antibonding $\pi_{g,x}$ and $\pi_{g,y}$ orbitals with angular momentum opposed but parallel spins, thus yielding the molecules paramagnetic behavior.[12] Therefore, unlike most stable molecules, the lowest $O_2$ electronic ground state is a spin triplet, $O_2(X^3\Sigma_g^-)$.In contrast to the ground state, the two electrons in the highest energy of the electronically excited state are antiparallel and are thus in the singlet configuration. Molecular orbital theory predicts two low-lying excited singlet states, $O_2(^1\Delta_g)$ and $O_2(^1\Sigma_g^+)$. These electronic states differ only in the spin and the occupancy of the two degenerate antibonding $\pi_g$-orbitals.[9] The excitation energy for $O_2(^1\Delta_g)$ is 0.98 eV (22.5 kcal/mole).[16, 17] Due to the aforementioned spin-forbidden transition to the ground state, $O_2(^1\Delta_g)$ has quite a long lifetime, lasting up to 45 minutes in the gas phase at low pressure.[12] In the liquid phase, due to collisional deactivation, lifetimes range between 2 and 1000 μs, depending on the solvent (3 μs in water, 50 μs in $D_2O$)[12, 18-20]. The second singlet state, $O_2(^1\Sigma_g^+)$, is very short lived ($10^{-11}$ s)[16] and relaxes rapidly to the lower lying $O_2(^1\Delta_g)$ excited state, and as such, there is minor interest of its presence in biological systems.[15, 21] It is thus the $O_2(^1\Delta_g)$-state which is the commonly referred singlet oxygen (herein defined simply as $^1O_2$).

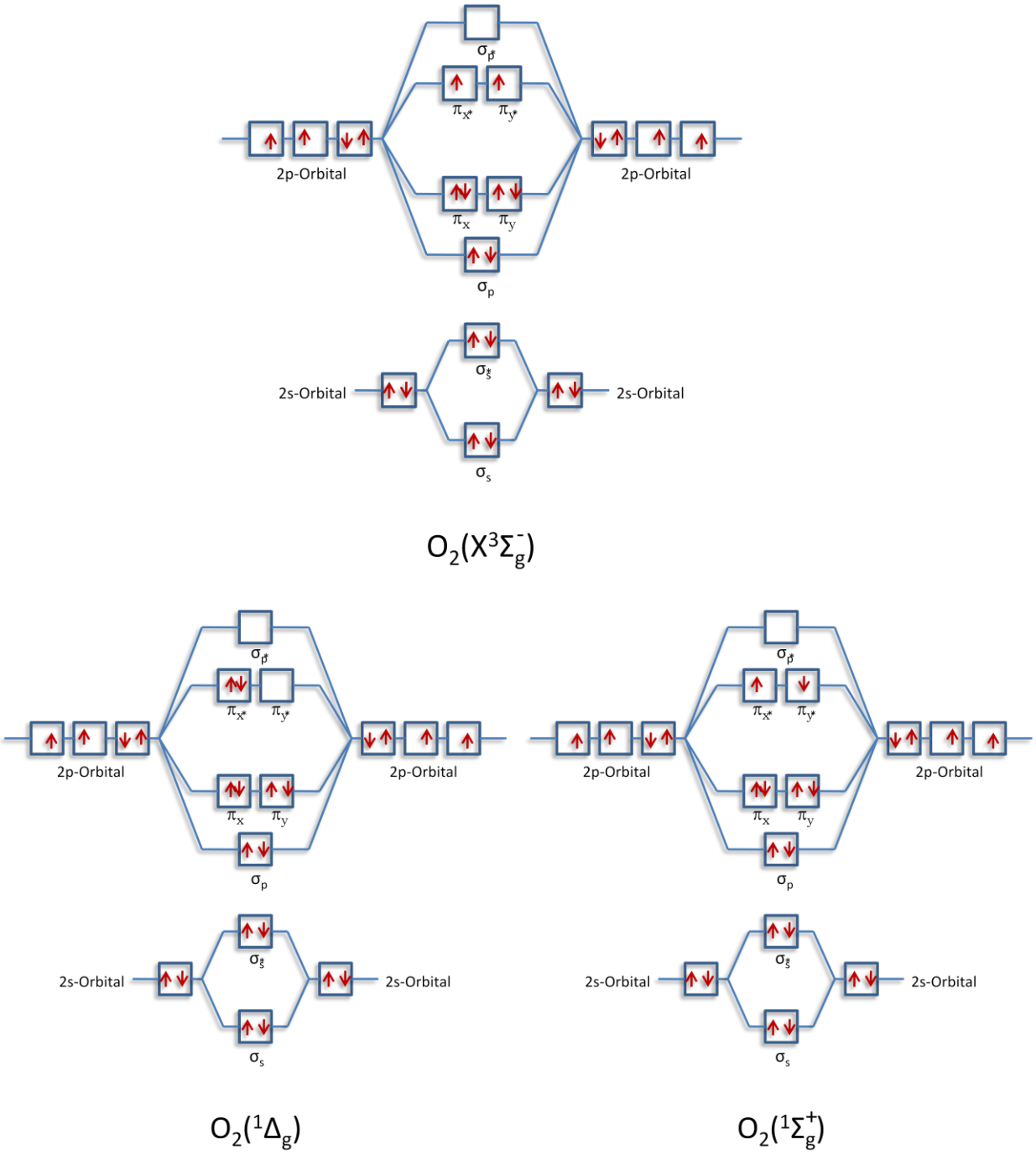


**Figure 5-3.** Molecular orbital diagrams for the three electronic configurations of molecular oxygen. The top is the triplet ground state, whereas the bottom right is the singlet oxygen $^1\Delta_g$ excited state, and left is the singlet oxygen $^1\Sigma_g^+$ excited state. Note that the states only differ in the spin and the occupancy of the two degenerate antibonding $\pi_g$-orbitals.

Subsequent to its generation, $^1O_2$ can either undergo spontaneous deactivation (process 1) or it can react oxidatively with a nearby labile biomolecule (*R*) to form some product or initiate some consequent reaction (*P*) (process 2):

$$Process\ 1:\ O_2(\ ^1\Delta_g) \xrightarrow{k_\Delta} O_2(\ ^3\Sigma_g^-)$$

$$Process\ 2:\ O_2(\ ^1\Delta_g) + R \xrightarrow{k_{P\Delta}} O_2(\ ^3\Sigma_g^-) + P$$

where $k_\Delta$ is the sum of all the unimolecular processes (radiative and non-radiative) that deactivate $O_2(^1\Delta_g)$. The latter relaxation reaction and initiation of succeeding *P* (process 2) is the critical behavior of $^1O_2$ in a biological system that is exploited as the therapeutic utility of this photodynamic process. Specifically, $^1O_2$ is employed as a transient tool to damage diseased cells[8] by oxidizing critical cellular macromolecules, including lipids, nucleic acids and proteins,[10, 11, 22, 23] and by recruiting inflammatory cells[24] and initiating the nonspecific activation of the immune system.[25] Furthermore, caspase activation, nuclear condensation, phosphatidylserine translocation, and a decrease in intracellular calcium levels, all induced by $^1O_2$, have been shown to stimulate apoptotic cell death.[8, 26, 27]

Though the consequence of this collective photodynamic process can yield a highly efficient, cytotoxic tool that causes irreversible cellular damage and tumor destruction,[28] each of the component steps in isolation (excitation, ISC, and energy transfer) is harmless. Thus, the underlying objective of this therapeutic approach is the controlled initiation and maximal interrelation of this series of photodynamic mechanisms to deliver an $^1O_2$ dose within the targeted disease site sufficient enough to eradicate local cells and irreversibly inactivate the disease propagation.[29, 30]

It is readily apparent from this description of interconnected events that PDT efficacy is dependent on three primary components involved in the initiation, production, and yield of the

antiproliferative initiator: the activating irradiation, photosensitizer agent, and endogenous oxygen content, respectively, all of which are complicatedly interdependent.[31]

### 5.1.2 Components of PDT

Returning briefly to the associated photophysical processes, we take a closer look at the potential for $^1O_2$ generation from the populated triplet state. Recall that molecular triplet states are metastable species that exhibit intrinsic decay primarily via deactivation through solvent collisions to overcome the spin forbidden $T_1 \rightarrow S_0$ transition.[4] Typical values of $T_1$ lifetimes ($\tau_T^0$) in aqueous solutions are on the order of tens of μs.[4] However, in complex systems that are comprised of multicomponent micro-environments, such as living tissue, multi-solvent effects[32, 33] and interfering/colliding molecules[33, 34] contribute additional decay modes that compete with the PDT-favorable oxygen interactions. Thus, the triplet lifetime $(\tau_T^{'})$ is reduced according to:

$$\frac{1}{\tau_T^{'}} = k_{TG} + k_{ox}[O_2] \qquad \text{[Eqn. 5-2]}$$

where the rate of triplet-to-ground deactivation $k_{TG} = 1/\tau_T^0$ and $k_{ox}$ is the sum of the rate parameters that describe the interactions between oxygen and $T_1$, including the formation of $O_2(^1\Delta_g)$:

$$T_1 + O_2(\,^3\Sigma_g^-) \xrightarrow{k_{\Delta T}} S_0 + O_2(\,^1\Delta g)$$

$$T_1 + O_2(\,^3\Sigma_g^-) \xrightarrow{k_{\Sigma T}} S_0 + O_2(\,^3\Sigma_g^-)$$

Note that $k_{ox} = k_{\Delta T} + k_{\Sigma T}$. From the above, the quantum yield of singlet oxygen generation ($\Phi_\Delta$) can be described as:

$$\Phi_\Delta = \Phi_T \frac{k_{ox}[O_2]}{k_{ox}[O_2] + k_{TG}} \qquad \text{[Eqn. 5-3]}$$

where $[O_2]$ is the intrinsic dissolved oxygen concentration. In most cases $k_{ox}[O_2] >> k_{TG}$; then:

$$\Phi_{\Delta} = \Phi_T S_{\Delta} \qquad \text{[Eqn. 5-4]}$$

where $S_{\Delta}$ is the fraction of quenching of $T_1$ by $O_2$ that lead to $O_2[^1\Delta_g]$.[4] Thus it is clear that the rate at which singlet oxygen is produced, as well as its yield, is critically dependent upon the oxygen concentration.[35] This influence of the oxygen saturation of the diseased site, is (for all intents and purposes) a situational variable that, though perhaps the most direct and influential on the ultimate outcome of the therapy - adequate molecular oxygen is required for the generation of $^1O_2$,[30] is characteristic of the particular disease and cannot be practically altered for functional sake.[30, 36] Most often, the oxygen saturation of tumor masses is in a depleted, hypoxic state.[37]

However, a number of studies have identified an association between the available oxygen content and the first component of PDT listed above, the incident irradiation used to initiate the process. There appears to be a direct affect between the photochemical consumption of oxygen during PDT and the fluence rate of the incident light.[38-40] Thus, it is now accepted that PDT is most effective when the fluence rate is reduced.[30] In this manner, the oxygen content to feed the therapeutic activity becomes a regressand of the activation light, in effect, capping light dosing to minimize superfluous attenuation of the already limited level of available oxygen.

Correspondingly, light dosage is also interrelated with the therapeutic capacity of the photosensitizer, in that enough energy must be applied to incite the excited sate and ultimately generate a critical amount of reactive $^1O_2$. Therefore, an efficient light dose is defined as that which provides enough energy to initiate the photosensitizer, while ensuring redundant energy is not applied that will improvidently reduce the concentration of available molecule oxygen. Following this basic analysis, the remaining PDT component, the therapeutic capacity of the photosensitizer, is revealed to be the workable independent variable in optimizing PDT efficacy. Modification of this amendable parameter will explicitly influence the critical $[O_2]$ requirement and light dosimetry needed to realize the therapeutic outcome.

The therapeutic capacity may be described as the agent's propensity to generate $^1O_2$ under the complex biological use conditions. Recent years have seen the development of novel photosensitizers which aim to maximize this functional capacity.[41, 42]On the whole, the model PDT photosensitizer enhances performance in four distinct areas:[43] (1) photophysically, the agent would have a high molar extinction coefficient in the ~700–850 nm wavelength range for maximum light penetration in tissue[44]; (2) photochemially yield a high $\Phi_T$ and resist significant photobleaching; (3) chemically remain stable in physiological environments; and (4) biologically present low dark toxicity, selective uptake in target tissues, microlocalization to key subcellular targets, and complete pharmacokinetic clearance at the end of use. To date, no single photosensitizer exhibits all of these properties; rather, many offer a favorable compromise of the abovementioned elements that demonstrate promise for improved efficacy in use.[1, 44]

### 5.1.3 Photosensitizers

At present, a large number of photosensitizers are in various stages of trials, though only a few of these has received regulatory approval.[29] Haematoporphyrin derivative (HpD), and its commercial oligomer analogues such as Photofrin (Axcan Pharma Inc.; Mont-Saint-Hilaire, Canada) and Photoheme (Academy of Fine Chemical Technology, Moscow), denote the first generation of clinically approved photosensitizers, with the first round of PDT results obtained over two decades ago.[9] Unfortunately there are several disadvantages associated with these first generation photosensitizers that have limited their clinical utility.[29, 42] In particular, these original agents demonstrated especially poor selectivity in terms of healthy and diseased tissues; only 0.1-3% of injected agent was found to concentrate in the tumor tissue. This is due, in part, to the high propensity of cutaneous tissue uptake and retention of these derivatives, sometimes for up to 10 weeks after initial administration, thus causing unfavorable long-term photosensitivity in the

patient. Furthermore, selective accumulation of the photosensitizer molecules in diseased tissues is required to avoid untargeted effects to healthy cells, an infamous consequence associated with conventional chemotherapeutic approaches for the management and eradication of malignant disease.[44] Another significant shortcoming is that these compounds exhibit low extinction coefficients[9] and absorption spectra in the red region of the electromagnetic spectrum, allowing only limited penetration depths in tissue (5 mm).[9] What is more, most first generation photosensitizer molecules are hydrophobic and aggregate easily in aqueous media. As discussed in earlier chapters, such interactions affect the chemical, photophysical, and biological properties by decreasing solubility, increasing collisional non-radiative deactivation, and encouraging untimely immune clearance, respectively. Thus, these limitations encouraged the development of many second generation photosensitizers with particular emphasis on improved tissue selectivity and photophysical activation characteristics.[9]

One such class of second generation molecules are the cyanines, which have been increasingly studied as potential PDT tools during the last decade.[1] Cyanine compounds demonstrate favorable *in vivo* distribution, mitigating the previous issue of cutaneous localization and hyper photo-sensitivity. The *in vivo* distribution is influenced by the chemical structure; therefore the cyanines hold particular value for their amphiphilicity, which facilitates the crossing of cell membranes. As a prime candidate, indocyanine green (ICG) was recently introduced into photomedicinal practice.[1]

In addition to the encouraging *in vivo* behavior, ICG is favored for biological application due to the strong absorption in the near infrared (NIR) region of the electromagnetic spectrum (700-1000 nm). As introduced in Chapter 1, the spectral position of the ICG absorption maximum (785 nm, related to the $S_o \rightarrow S_1$ transition.[6]) is close to the minimum isosbestic point of the absorption spectra of hemoglobin and oxyhemoglobin, the major absorbing constituents of biological tissue,[45, 46 47] allowing maximal penetrations with minimal attenuation. However,

despite the numerous auspicious properties, it was not until recently that the potential for ICG as a photosensitizer, by way of numerous observations of a potent *in vitro* antineoplastic activity upon irradiation, was uncovered.[22, 46, 47] Further attention in ICG for PDT was sparked with the observation that cells embedded with the fluorophore resisted photodamage when incubated with specific $^1O_2$ quenchers.[22]

### 5.1.4 Current Limitation of ICG as an Effective Photosensitizer

Unfortunately, despite the numerous advantages, several of the previously examined traits of ICG in solution constrain the maximum capacity in PDT application, paralleled to its limitations as a fluorescent probe in bioimaging applications (Chapter 3). Of specific PDT significance is the restrained yield of ICG triplet formation ($\Phi_T$), which has been determined to be 14% in water and 11% in aqueous albumin solution.[1, 22, 47] This low $\Phi_T$ response is expected for ICG based on the earlier discussions regarding the efficient deactivation of the excited state ($S_1$) from a multiplicity of photophysical and photochemical processes which come as an alternative to triplet formation (and fluorescence emission):[1, 48] Thus, the pace at which the excited state is decayed (hence the short fluorescent lifetime), leaves only a fleeting amount of time for intersystem crossing to occur. Therefore, akin to the influence on $k_\Gamma$ and $\Phi_F$, this factor comes at the expense of $k_{ISC}$, effectively diminishing $\Phi_T$ [Eqn. 5-1].

Although second-generation photosensitizers such as ICG are overall more efficient than their foregoing counterparts, a third generation of agents is presently being developed to eliminate the few lingering limitations. Third generation photosensitizers are classified as second generation agents that are bound or internalized into carriers for selective accumulations and *in vivo* improvements. Thus, the ICG-encapsulating CPSNPs, originally developed for augmentation of imaging utility, can potentially fall into this category as an improved third generation

photosensitizer for PDT application. The work herein examines the functional improvements of ICG $^1O_2$ generation by encapsulating within the CPSNP matrix as it relates to PDT, analogous to the previously demonstrated optical improvements as they related to imaging use.

## 5.2 Materials and Methods

### 5.2.1 Materials

Indocyanine green was acquired from TCI America (Portland, OR) and kept in dark refrigeration until use. Methyl alcohol (99.8%, anhydrous) and deuterium oxide (99.9 atom % D) were purchased from Sigma Aldrich (St Louis, MO). Singlet Oxygen Sensor Green® (SOSG) reagent was acquired from Invitrogen (Carlsbad, CA). All reagents were prepared immediately prior to use. ICG-CPSNPs were synthesized by the method introduced in Chapter 2 and stored in refrigeration prior to use. All solutions were warmed to 37$^o$C in a water bath during experimentation to mitigate any thermal concerns. The dissolved oxygen concentrations were measured on a dissolved oxygen meter (Extech 407510; Extech Instruments, Waltham, MA).

### 5.2.2 SOSG Signal Optimization and Lifetime

In order to qualitatively relate the scale of generated singlet oxygen from free ICG molecules and molecules internalized within CPSNPs, the $^1O_2$ generated was indirectly detected through the chemiluminescence of Singlet Oxygen Sensor Green® (SOSG), a highly selective reagent for $^1O_2$ with no appreciable response to hydroxyl radicals or superoxide.[49] This sensor exhibits a weak native blue fluorescence (excitation 372/393 nm, emission 395/416 nm).

However, in the proximity of $^1O_2$, SOSG emits a green fluorescence with excitation and emission peaks around 500 nm and 530 nm, respectively.[50]

Before effective evaluation of the photosensitizer influence on singlet oxygen generation could begin, the SOSG fluorescent signal was optimized. An SOSG stock solution of $1.4 \times 10^{-4}$ M was prepared in accordance to the manufacturer recommendations in a 2% methanol (by volume) aqueous solution. The analyte solvent was intended to mimic the physiological environments of clinical PDT applications. However, PBS was not used because the quenching mechanisms for both free ICG and those reported for singlet oxygen in this high ionic strength solvent resulted in indiscriminate variations in recorded responses over the time scale of experimentation, particularly at higher irradiation energy densities. Therefore, $D_2O$ was selected as the aqueous solvent environment due to its demonstrated extension of singlet oxygen lifetime.[12, 18-20] The dissolved oxygen concentration in the as-received $D_2O$ solution was measured to be 8.3 mg/L. The optimal ICG:SOSG molar ratio for strongest SOSG signal at 530 nm was determined by fixing the moles of SOSG ($4.2 \times 10^{-10}$) and recording the emission response as a function of ICG quantity ($0 – 1.7 \times 10^{-9}$ moles). Various volumes of a $10^{-5}$ M stock solution of ICG in a 7:3 by volume ethanol to water ratio were combined with the 30 μL of SOSG stock in individual microwells of a 96-well plate immediately prior to evaluation. These mixtures were topped off to a total volume of 200 μL as needed with $D_2O$ to maintain the same path length. Each 200 μL analyte was individually irradiated with a low divergence 785 nm laser diode (40 mW, LDM-5; Laserex Technologies, Adelaide, Australia) for 60 seconds (4.78 J/cm$^2$) and then immediately placed into a microplate spectrofluorometer (SpectraMax Gemini Em; Molecular Devices, Sunnyvale, CA) for collection of an emission scan over the 500 - 600 nm range (fixed Ex: 480 nm –identified as peak in this binary solvent). Each ICG:SOSG ratio was measured in triplicate. A corresponding blank solution of $4.2 \times 10^{-10}$ moles of SOSG in 170 uL of $D_2O$ was irradiated and the emission scan recorded to correct for intrinsic fluorescence of the SOSG molecule.

Irradiations were conducted by placing the optical end of the laser module flush against the plate, such that the optical axis of the laser line was centered on the well area and normal to the face of the plate. The laser beam diameter for this module is 8 mm, sufficient to homogenously irradiate the entire volume of analyte. Finally, the stability of the 530 nm SOSG intensity after laser irradiation was determined by examining the signal intensity as a function of time. All fluorescent data collection and background subtractions used SoftMax Pro microplate data software (Molecular Devices, Sunnyvale, CA).

### 5.2.3 SOSG Intensity as a function of Photosensitizer Concentration

The influence on SOSG signal (thus the qualitative levels of generated $^1O_2$) produced by either the free photosensitizer or ICG-CPSNPs were evaluated by comparing the photosensitizer-SOSG intensity relationship. Solutions of ICG of varying concentrations were prepared in 7:3 EtOH:$H_2O$ from a 0.01 M free ICG stock. Suspensions of corresponding ICG-CPSNPs were prepared by appropriately diluting a sample into various 7:3 EtOH:$H_2O$ analytes such that the final ICG concentrations in each matched the absorption of a free ICG counterpart. The quantification of encapsulated ICG concentration in the original ICG-CPSNP suspension was achieved via the absorption measurement on EDTA-dissolved CPSNPs, as described in detail in Chapter 2. A 3 x $10^{-6}$ M SOSG solution was prepared from the SOSG stock, allowing a minimal volume fraction of 2% methanol in the final analyte volume. To maintain a constant temperature, all solutions, the 96-well plate, and the laser module, were housed in a warming oven set to 37$^o$C. A fraction of ICG solution was pipetted into a well, followed by an appropriate amount of SOSG solution such that the overall IGC to SOSG molar ratio in the volume, identified from above, was constant. The analyte volume was then padded to 200 μL with $D_2O$. A corresponding background solution for each analyte comprising of the equivalent SOSG content (no ICG) was prepared.

Laser irradiation was achieved by pressing the optical end of a 785 nm laser diode module (72 mW , LDM-EIA-60; Laserex Technologies, Adelaide, Australia) onto the particular analyte well for a precise duration of 67 seconds such that the total energy density across the 7 mm beam diameter of this laser module amounted to 12.5 J/cm$^2$. As described above, this irradiation was conducted within the warming oven with an ambient temperature of 37$^o$C. Immediately after the irradiation, the plate was transferred to the plate reader for the 530 nm emission scan (480 nm excitation). The plate reader was also set to maintain a 37$^o$C temperature. This process continued for a range of photosensitizer concentrations ($10^{-7}$ – 5 x $10^{-6}$ M). Background spectra were subtracted from each corresponding sample spectra, and the corrected emission intensity at 530 nm was plotted as function of ICG concentration. All points were measured in triplicate with fresh solutions. The experiment was repeated in triplicate for both free and encapsulated ICG at a 785 nm irradiation energy density of 50 J/cm$^2$ by increasing the irradiation time to 4 minutes and 27 seconds.

### 5.2.4 ICG-CPSNP - Induced SOSG Intensity as function of Irradiation Fluence

The SOSG fluorescence emission scans (Ex. 480 nm, Em. 530 nm) were conducted at constant encapsulated ICG concentrations of 5 x $10^{-6}$ and 5 x $10^{-7}$ M as a function of irradiation intensity (0 – 300 J/cm$^2$). The ICG:SOSG molar ratio was kept at 0.42 and the total analyte volume was 200 μL in $D_2O$. A blank solution of SOSG in $D_2O$ was used to background correct the collected emission spectra. The target energy density was adjusted by adjusting the irradiation time for which the analyte was exposed. Immediately after each laser irradiation, the plate was transferred from the warming oven to the fluorescence plate reader and the emission intensity at 530 nm (Ex 480 nm) was recorded. Each data point was repeated in triplicate.

## 5.3 Results and Discussion

### 5.3.1 Singlet Oxygen Sensor Green (SOSG) Singlet Oxygen Detection

The qualitative scale of singlet oxygen generated from the photosensitizers was determined by the chemiluminescent emission of SOSG. First, to maximize the SOSG signal, the optimal ratio of $^1O_2$-probe and photosensitizer was determined to be 0.42, corresponding to a 2.38 molar excess of SOSG to ICG. Succeeding experiments were designed such that the influence of the solvent-susceptible lifetime of any generated singlet oxygen was constant between all runs. Thus, the time-dependent stability of the generated SOSG signal was examined to identify the window of time that allowed appreciable reproducibility between runs. Figure 5-4 reveals a 5% decrease in SOSG signal occurs within 2 minutes post-irradiation.

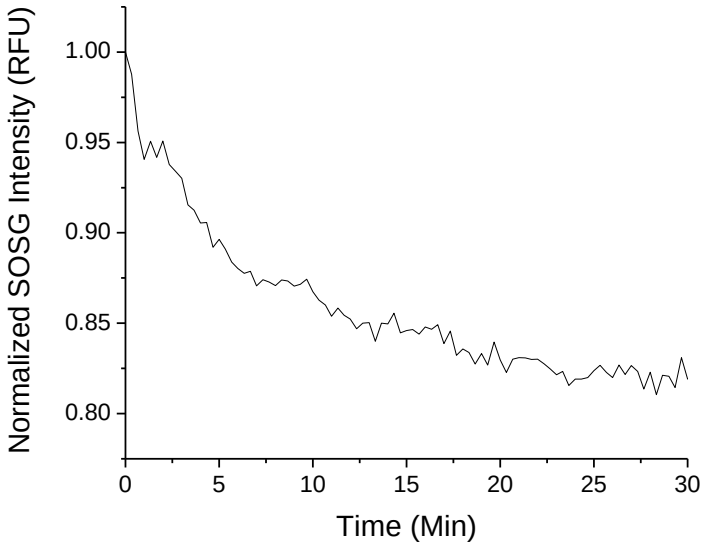


**Figure 5-4.** The 530 nm SOSG emission intensity quenches over time, corresponding to both the excited lifetime of singlet oxygen as well as associated excited state quenching of the fluorescence probe itself. A 5% decrease in the emission is observed within 2 minutes after irradiation.

### 5.3.2 Encapsulation Effect on ICG $^1O_2$ Generation

The main avenue for evaluating potential variations of PDT efficacy is in examining the level of singlet oxygen generated from these ICG-encapsulating nanoparticles compared to the unencapsulated sensitizer, under the pretense that, *ceteris paribus*, the higher the output of generated singlet oxygen, the higher the therapeutic capacity. In turn, increases in therapeutic capacity are associated with an overall enhancement in PDT efficacy, in that lower intrinsic [$O_2$] and/or reduced irradiation dosages could yield equivalent therapeutic outcomes. Although a quantification of the generated $^1O_2$ was not attempted, the relative SOSG intensity at 530 nm is assumed to be proportional to the level of singlet oxygen present, offering a qualitative appraisal of the $^1O_2$ production.

To appreciate the $^1O_2$ generation in the clinical PDT use environment, the *ex situ* examination was conducted in a comparable environment to that of an *in vivo* tumor microenvironment. Care was taken to ensure steady physiological temperature (37$^o$C). Likewise, the hypoxic environment of solid tumors was imitated by the dissolved oxygen content in the aqueous solvent. Brahimi-Horn and Pouyssegur report [$O_2$] for solid tumors in the range of 0.8 – 8 mg/L.[37] The *ex situ* environment fell within this range (~8 mg/L), and serves to best illustrate the potential performance of these photosensitizers in clinical conditions.

Figure 5-5 illustrates the SOSG intensity as a function of photosensitizer concentration for both free and encapsulated ICG, normalized per unit energy (J/cm$^2$). Comparing the slope of the fitted lines reveals that there is 1.6 times the SOSG signal from encapsulated photosensitizers. Returning to the postulation that SOSG intensity correlates to the level of singlet oxygen present in the analyte, this result is taken to convey a 60% escalation in the photosensitized $^1O_2$ generation upon encapsulation of the ICG within the CPSNPs. Much like the previously reported improvements in optical performance, this can, in part, be attributed to the matrix shielding

effect; shelter from undesirable excited state relaxations provides the internalized ICG molecule a longer excited lifetime, which in turn amplifies the incidence of the intrinsic internal conversions to the triplet state ($S_1 \rightarrow T_1$).

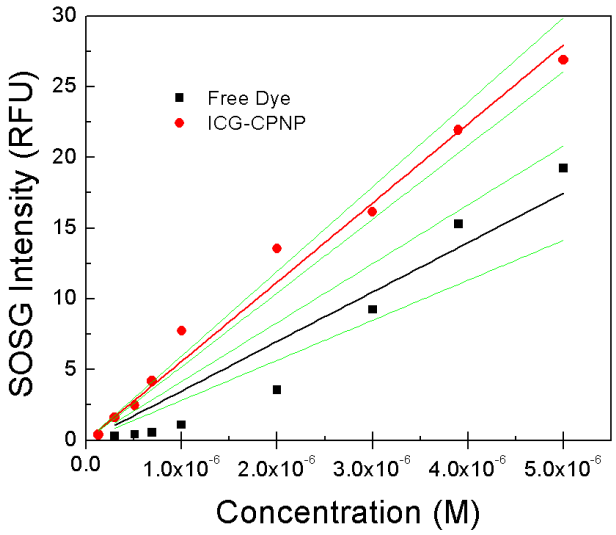


**Figure 5-5**. A comparison of the SOSG intensity as a function of photosensitizer concentration reveals a 60% greater response from ICG molecules encapsulated within CPSNPs compared to the free fluorophore. The SOSG intensity correlates to the level of photoactivated singlet oxygen. Experiments were conducted in a hypoxic (8.3 mg/L dissolved $O_2$) aqueous solution in $D_2O$ at 37°C. Each data point is the mean of five separate runs normalized to energy density (J/cm$^2$). The green lines correspond to the 95% confidence interval of the linear fits.

### 5.3.3. Therapeutic Capacity of ICG-CPSNPs Photosensitizers

Now that the heightened photoexcitation of singlet oxygen from ICG-CPSNPs has been established, attention is turned to evaluating their clinical PDT relevance. As previously mentioned, it is accepted that PDT is most effective when the irradiation fluence is reduced.[30] A map of therapeutic output as a function of encapsulated ICG concentration at various irradiation energies would aid in guiding the most efficacious PDT dosing. Such a map is referred to as a

dosimetry plot and provides visualization of the minimal fluence -photosensitizer concentration combination that yields a certain response, such as a specific level of cell death.

The first step in developing such a dosing map is to recognize the relationship between activating fluence and the performance outcome, termed the sensitizer therapeutic capacity. The ultimate PDT response, the generation of a critical amount of $^1O_2$ to yield substantial cell death, is, thus far in the discussion, represented by the intensity of the SOSG signal. Therefore, Figure 5-6 presents the therapeutic capacity of ICG-CPSNPs in terms of the SOSG intensity versus energy density relationship for a single encapsulated ICG molecule. Examination of the figure reveals the non-linear response of SOSG intensity, particularly in the range of 100 J/cm$^2$. This behavior is attributed to the finite therapeutic capacity of a single photosensitizer molecule. The $^1O_2$ yield (SOSG signal) for encapsulated ICG is saturated at energy densities above 65 J/cm$^2$, which can be

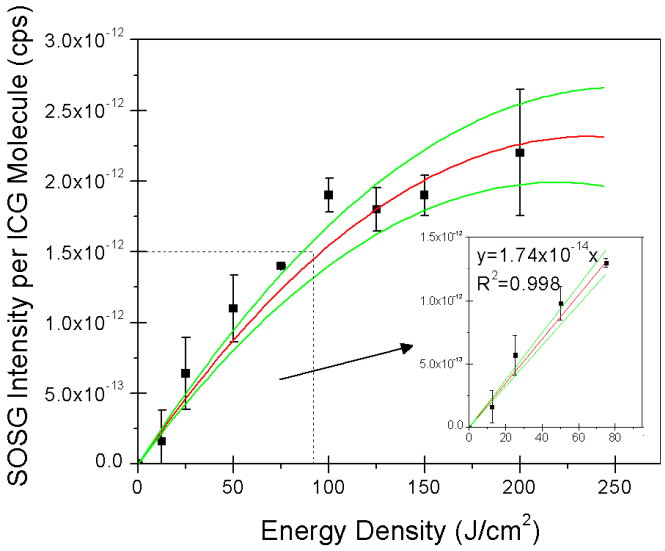


**Figure 5-6.** The SOSG signal intensity as a function of laser fluence reveals a non-linear response indicative of the finite therapeutic capacity of a single encapsulated ICG photosensitizer molecule. The linear region of the fitted red curve will be used to model dosing response. The green curves correspond to the 95% confidence bands of the polynomial fit. SOSG intensity qualitatively represents the level of generated singlet oxygen for therapeutic function.

described as the critical fluence magnitude that prompts the intrinsic maximum incidence of triplet state formation and energy transfer to excite singlet oxygen; additional energy serves no further photodynamic function, hence the leveling off of the SOSG response.

Given the therapeutic capacity of an internalized ICG molecule, a dosing map for SOSG intensity can be constructed as a function of ICG concentration and irradiation energy. A limit of 65 J/cm$^2$ is imposed on the map to eliminate margins associated with the critical therapeutic threshold of the photosensitizer. This maximum energy density is defined by the limit of the linear region in Figure 5-6 (inset). The dosing map for SOSG intensity is presented in Figure 5-7.

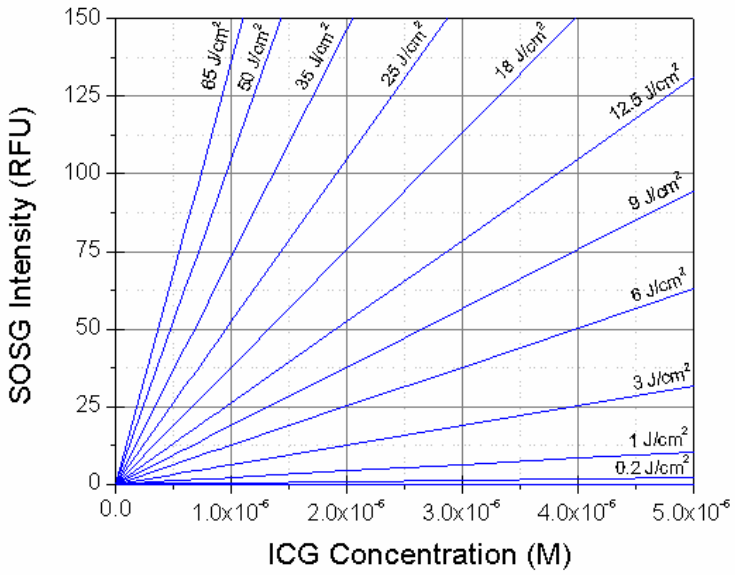


**Figure 5-7.** An encapsulated ICG and laser fluence dosing map for SOSG intensity is constructed from the linear region of the ICG therapeutic capacity relationship depicted in Figure 5-6. The map visually relates the SOSG signal intensities as a function of photosensitizer-laser energy density combinations.

Figure 5-7 is presently devoid of any relevant therapeutic information. For practical clinical implication, a dosing map must relate the dosimetry of both the photosensitizer and laser irradiation to an actual clinical performance. Thus, the SOSG signal, which qualitatively

represents the level of generated $^1O_2$ product, must now be associated to a more clinically meaningful function. The following chapter will correlate the incidental SOSG signal to cell viability.

## 5.4 Summary

The work in this chapter was designed to evaluate the performance of the ICG-CPSNP as a potential photosensitizer in a photodynamic therapeutic modality. The *ex situ* examination of photoactivation of singlet oxygen in a hypoxic aqueous environment was found to be 60% higher from the ICG molecules upon encapsulation within the CPSNP matrix. Such an increase highlights the potential improvement in photosensitization capacity of this third generation photosensitizer, suggesting a greater efficiency in photodynamic therapies. This performance enhancement is attributed to the shielding of the fluorophore from premature excited state relaxations that prevent the intrinsic fraction of triplet state intersystem crossing and subsequent energy transfer to molecular oxygen.

The therapeutic capacity of these ICG-CPSNP composites was then determined by observing the SOSG intensity of a single encapsulated ICG molecule as a function of the irradiation energy. This behavior was found to be non-linear, corresponding to the finite rate of intersystem crossing. This relationship was then employed to model the expected SOSG intensity as a function of encapsulated ICG concentration-laser irradiation combinations. Such a relationship set up the possibility to associate the photosensitizer and laser dosing to a targeted therapeutic response in a dosimetry map.

## 5.5 Acknowledgements

The indispensable efforts of Sarah Knupp, an undergraduate research assistant for the Adair research group, without which the optimization of the chemiluminescent SOSG detection and a practical experimental setup in a hypoxic environment would not have been possible, must be recognized. Her assiduous efforts in developing a workable experimental procedure to maintain a constant temperature while recovering a constant and reproducible SOSG signal, not to mention the numerous hours spent irradiating and collecting fluorescence spectra, one analyte at a time, is greatly appreciated.

## 5.6 References

1. Delaey, E.; van Laar, F.; De Vos, D.; Kamuhabwa, A.; Jacobs, P.; de Witte, P. A. M. A Comparative Study of the Photosensitizinf Characteristics of Some Cyanine Dyes. *Journal of Photochemistry and Photobiology B: Biology* **2000,** *55*, 27-36.
2. Kawaoka, K.; Khan, A. U.; Kearns, D. R. Role of Singlet Excited States of Molecular Oxygen in the Quenching of Organic Triplet States. *Journal of Chemical Physics* **1967,** *46*, 1842-1853.
3. Parmenter, C. S.; Rau, J. D. Fluorescence Quenching in Aromatic Hydrocarbond by Oxygen. *Journal of Chemical Physics* **1969,** *51*, 2242-2246.
4. Gorman, A. A.; Rodgers, M. A. J. Current Perspectives of Singlet Oxygen Detection in Biological Environments. *Journal of Photochemistry and Photobiology B: Biology* **1992,** *14*, 159-176.
5. Lakowicz, J. R., *Principles of Fluorescence Spectroscopy*. 3rd ed.; Springer: Baltimore, MD, 2006.
6. De Boni, L.; Rezende, D. C. J.; Mendonça, C. R. Reverse Saturable Absorption Dynamics in Indocyanine Green. *Journal of Photochemistry and Photobiology A: Chemistry* **2007,** *190*, 41-44.
7. Niedre, M. J.; Patterson, M. S.; Giles, A.; Wilson, B. C. Imaging of Photodynamically Generated Singlet Oxygen Luminescence in Vivo. *Photochemistry and Photobiology* **2005,** *81*, 941-943.
8. Salet, C.; Moreno, G.; Ricchelli, F.; Bernardi, P. Singlet Oxygen Produced by Photodynamic Action Causes Inactivation of the Mitochondrial Permeability Transition Pore. *Journal of Biological Chemistry* **1997,** *272*, 21938-21943.
9. DeRosa, M. C.; Crutchley, R. J. Photosensitized Singlet Oxygen and Its Applications. *Coordination Chemistry Reviews* **2002,** *233-234*, 351-371.

10. Kim, S. Y.; Kim, E. J.; Park, J.-W. Control of Singlet Oxygen-Induced Oxidative Damage in Escherichia Coli. *Journal of Biochemistry and Molecular Biology* **2002,** *35*, 353-357.
11. Maisch, T.; Baier, J.; Franz, B.; Maier, M.; Landthaler, M.; Szeimies, R.-M.; Bäumler, W. The Role of Singlet Oxygen and Oxygen Concentration in Photodynamic Inactivation of Bacteria. *Proceedings of the National Academy of Sciences of the United States of America* **2007,** *104*, 7223-7228.
12. Wefers, H. Singlet Oxygen in Biological Systems. *Bioelectrochemistry and Bioenergetics* **1987,** *18*, 91-104.
13. Kilger, R.; Maier, M.; Szeimies, R.-M.; Bäumler, W. Bidirectional Energy Transfer between the Triplet T1 State of Photofrin and Singlet Oxygen in Deuterium Oxide. *Chemical Physics Letters* **2001,** *343*, 543-548.
14. Jones, L. R.; Grosswiner, L. I. Singlet Oxygen Generation by Photofrin(R) in Homogeneous and Light-Scattering Media. *Journal of Photochemistry and Photobiology B-Biology* **1994,** *26*, 249-256.
15. Snyder, J. W.; Skovsen, E.; Lambert, J. D. C.; Poulsen, L.; Ogilby, P. R. Optical Detection of Singlet Oxygen from Single Cells. *Physical Chemistry Chemical Physics* **2006,** *8*, 4280-4293.
16. Krinsky, N. I. Singlet Oxygen in Biological Systems. *Trends in Biochemical Sciences* **1977,** *2*, 35-38.
17. Schweitzer, C.; Schmidt, R. Physical Mechanisms of Generation and Deactivation of Singlet Oxygen. *Chemical Reviews* **2003,** *103*, 1685-1757.
18. Lindig, B. A.; Rodgers, M. A. J.; Schaap, A. P. Determination of the Lifetime of Singlet Oxygen in D2o Using 9,10-Anthracenedipropionic Acid, a Water-Soluble Probe. *Journal of the American Chemical Society* **1980,** *102*, 5590=5593.
19. Merkel, P. B.; Kearns, D. R. Remarkable Solvent Effects on Lifetime of Delta-1-G Oxygen. *Journal of the American Chemical Society* **1972,** *94*, 1029-&.
20. Rodgers, M. A. J.; Snowden, P. T. Lifetime of O-2(1delta-G) in Liquid Water as Determined by Time-Resolved Infrared Luminescence Measurements. *Journal of the American Chemical Society* **1982,** *104*, 5541-5543.
21. Baier, J.; Maisch, T.; Regensburger, J.; Loibl, M.; Vasold, R.; Bäumler, W. Time Dependence of Singlet Oxygen Luminescence Provides an Indication of Oxygen Concentration During Oxygen Consumption. *Journal of Biomedical Optics* **2007,** *12*, 064008-1-7.
22. Bäumler, W.; Abels, C.; Karrer, S.; Weiß, T.; Messmann, H.; Landthaler, M.; Szeimies, R.-M. Photo-Oxidative Killing of Human Colonic Cancer Cells Using Indocyanine Green and Infrared Light. *British Journal of Cancer* **1999,** *80*, 360-363.
23. Halliwell, B.; Gutteridge, J. M. C. Lipid-Peroxidation, Oxygen Radicals, Cell-Damage, and Antioxidant Therapy. *Lancet* **1984,** *1*, 1396-1397.
24. Cecic, I.; Korbelik, M. Mediators of Peripheral Blood Neutrophilia Induced by Photodynamic Therapy of Solid Tumors. *Cancer Letters* **2002,** *183*, 43-51.
25. Granville, D. J.; McManus, B. M.; Hunt, D. W. C. Photodynamic Therapy: Shedding Light on the Biochemical Pathways Regulating Porphyrin-Mediated Cell Death. *Histology and Histopathology* **2001,** *16*, 309-317.
26. Valencia, A.; Moran, J. Reactive Oxygen Species Induce Different Cell Death Mechanisms in Cultured Neurons. *Free Radical Biology and Medicine* **2004,** *36*, 1112-1125.
27. Moreno, G.; Poussin, K.; Ricchelli, F.; Salet, C. The Effect of Singlet Oxygen Produced by the Photodynamic Action on the Mitochondrial Permeability Transition Differ in

Accordance with the Localization on the Sensitizer. *Archives of Biochemistry and Biophysics* **2001,** *386*, 243-250.

28. Agostinis, P.; Vantieghem, A.; Merlevede, W.; de Witte, P. A. M. Hypericin in Cancer Treatment: More Light on the Way. *The International Journal of Biochemistry & Cell Biology* **2001,** *34*, 221-241.
29. Cavalcante, R. S.; Imasato, H.; Bagnato, V. S.; Perussi, J. R. A Combination of Techniques to Evaluate Photodynamic Efficiency of Photosensitizers. *Laser Physics Letters* **2009,** *6*, (1), 64-70.
30. Dysart, J. S.; Singh, G.; Patterson, M. S. Calculation of Singlet Oxygen Dose from Photosensitizer Fluorescence and Photobleaching During Mthpc Photodynamic Therapy of Mll Cells. *Photochemistry and Photobiology* **2005,** *81*, 196-205.
31. Jarvi, M. T.; Niedre, M. J.; Patterson, M. S.; Wilson, B. C. Singlet Oxygen Luminescence Dosimetry (Sold) for Photodynamic Therapy: Current Status, Challenges and Future Prospects. *Photochemistry and Photobiology* **2006,** *82*, 1198-1210.
32. Vakrat-Haglili, Y.; Weiner, L.; Brumfeld, V.; Brandis, A.; Salomon, Y.; Mcllroy, B.; Wilson, B. C.; Pawlak, A.; Rozanowska, M.; Sarna, T.; Scherz, A. The Microenvironment Effect on the Generation of Reactive Oxygen Species by Pb-Bacteriopheophoribe. *Journal of the American Chemical Society* **2005,** *127*, 6487-6497.
33. Baier, J.; Maisch, T.; Maier, M.; Engel, E.; Landthaler, M.; Bäumler, W. Singlet Oxygen Generation by Uva Light Exposure of Endogenous Photosensitizers. *Biophysical Journal* **2006,** *91*, 1452-1459.
34. Tanielian, C.; Schweitzer, C.; Merchin, R.; Wolff, C. Quantum Yield of Singlet Oxygen Production by Monomeric and Aggregated Forms of Hematoporphyrin Derivate. *Free Radical Biology and Medicine* **2001,** *30*, 208-212.
35. Henderson, B. W.; Dougherty, T. J. How Does Photodynamic Therapy Work? *Photochemistry and Photobiology* **1992,** *55*, 145-157.
36. Chapman, J. D.; Stobbe, C. C.; Arnfield, M. R.; Santus, R.; Lee, J.; McPhee, M. S. Oxygen Dependency of Tumor-Cell Killing in Vitro by Light-Activated Photofrin-Ii. *Radiation Research* **1991,** *126*, 73-79.
37. Brahimi-Horn, M. C.; Pouyssegur, J. Oxygen, a Source of Life and Stress. *FEBS Letters* **2007,** *581*, 3582-3591.
38. Coutier, S.; Bezdetnaya, L. N.; Foster, T. H.; Parache, R. M.; Guillemin, F. Effect of Irradiation Fluence Rate on the Efficacy of Photodynamic Therapy and Tumor Oxygenation in Meta-Tetra (Hydroxyphenyl) Chlorin (Mthpc)-Sensitized Ht29 Xenografts in Nude Mice. *Radiation Research* **2002,** *158*, 339-345.
39. Henderson, B. W.; Busch, T. M.; Vaughan, L. A.; Frawley, N. P.; Badich, D.; Sosa, T. A.; Zollo, J. D.; Dee, A. S.; Cooper, M. T.; Bellnier, D. A.; Greco, W. R.; Oseroff, A. R. Photofrin Photodynamic Therapy Can Significantly Deplete or Preserve Oxygenation in Human Basal Cell Carcinomas During Treatment, Depending on Fluence Rate. *Cancer Research* **2000,** *60*, 525-529.
40. Sitnik, T. M.; Hampton, J. A.; Henderson, B. W. Reduction of Tumour Oxygenation During and after Photodynamic Therapy in Vivo: Effects of Fluence Rate. *British Journal of Cancer* **1998,** *77*, 1386-1394.
41. Piette, J.; Volanti, C.; Vantieghem, A.; Matroule, J.-Y.; Habraken, Y.; Agostinis, P. Cell Death and Growth Arrest in Response to Photodynamic Therapy with Membrane-Bound Photosensitizers. *Biochemical Pharmacology* **2003,** *66*, 1651-1659.
42. Ross, H. M.; Smelstoys, J. A.; Davis, G. J.; Kapatkin, A. S.; Del Piero, F.; Reineke, E.; Wang, H.; Zhu, T. C.; Busch, T. M.; Yodh, A. G.; Hahn, S. M. Photodynamic Therapy

with Motexafin Lutetium for Rectal Cancer: A Preclinical Model in the Dog. *Journal of Surgical Research* **2006,** *135*, 323-330.

43. Wilson, B. C.; Patterson, M. S. The Physics, Biophysics and Technology of Photodynamic Therapy. *Physics in Medicine and Biology* **2008,** *53*, R61-R109.
44. Bechet, D.; Couleaud, P.; Frochot, C.; Viriot, M.-L.; Guillemin, F.; Barberi-Heyob, M. Nanoparticles as Vehicles for Delivery of Photodynamic Therapy Agents. *Trends in Biotechnology* **2008,** *26*, 612-621.
45. Kochubey, V. I.; Kulyabina, T. V.; Tuchin, V. V.; Altshuler, G. B. Spectral Characteristics of Indocyanine Green Upon Its Interaction with Biological Tissues. *Optics and Spectroscopy* **2005,** *99*, 560-566.
46. Abels, C.; Fickweiler, S.; Weiderer, P.; Bäumler, W.; Hofstädter, F.; Landthaler, M.; Szeimies, R.-M. Indocyanine Green (Icg) and Laser Irradiation Induced Photooxidation. *Archives of Dermatological Research* **2000,** *292*, 404-411.
47. Reindl, S.; Penzkofer, A.; Gong, S.-H.; Landthaler, M.; Szeimies, R.-M.; Abels, C.; Bäumler, W. Quantum Yield of Triplet Formation for Indocyanine Green. *Journal of Photochemistry and Photobiology A: Chemistry* **1997,** *105*, 65-68.
48. Kassab, K. Photophysical and Photosensitizing Properties of Selected Cyanines. *Journal of Photochemistry and Photobiology B: Biology* **2002,** *68*, 15-22.
49. Ragas, X.; Jimenez-Banzo, A.; Sanchez-Garcia, D.; Batllori, X.; Nonell, S. Singlet Oxygen Photosensitisation by the Fluorescent Probe Singlet Oxygen Sensor Green®. *Chemical Communication* **2009**, 2920-2922.
50. Hideg, E. A Comparative Study of Fluorescent Singlet Oxygen Probes in Plant Leaves. *Central European Journal of Biology* **2008,** *3*, 273-284.

# Chapter 6

## Photodynamic Therapy Using ICG-CPSNPs as the Photosensitizing Agent

Now that ICG-CPSNPs have demonstrated improved singlet oxygen photosensitization in a hypoxic *ex situ* environment, evaluation is extended to the therapeutic faculty through *in vivo* photodynamic experiments. A number of previous efforts have demonstrated that ICG possesses a powerful *in vitro* photocytotoxic activity in a variety of cell lines,[1-6] though to date there has been no reported ICG *in vivo* photodynamic therapy (PDT) experimentation. A demonstration of heightened photodynamic cell lethality with ICG-CPSNPs relative to the unencapsulated photosensitizer *in vivo* will serve as the conclusive substantiation of the bifunctionality of these vectors, and highlight the capacity of this composite nanoplatform as an effective theranostic agent.

### 6.1 Control of the Cell Death Pathway and Ultimate Physiological Response to PDT

One of the functional advantages of PDT is that the overall dose can be tailored by adjusting the combination of photosensitizer concentration and light fluence rate, for a truly case-specific response that accounts for variations in disease presentation depth and tissue location, as well as the disease type itself.[7] This therapeutic adaptability is a valuable advantage in treatment approaches, particularly for early state disease, since a designed degree of cell death can be generated with minimal deleterious side effects for a wide range of disease presentations.

The flexibility in the degree of local physiological influence induced by the confined photoactivation of singlet oxygen ($^1O_2$) is granted by regulating the pathway of cell death triggered by PDT. Cell lethality initiated by $^1O_2$ occurs through two major channels: (i) a direct pathway leading either to apoptosis and/or necrosis;[8] and (ii) an indirect pathway that causes the

recruitment of inflammatory cells (neutrophils, macrophages, etc.)[9] and the nonspecific activation of the immune system.[10] As alluded to in Chapter 5, the balance between these two pathways can be directed by numerous PDT parameters, such as the fluence rate, the local oxygen concentration, photosensitizer dose and therapeutic capacity, as well as the cell type and the physicochemical properties of the photosensitizer – which controls the intracellular localization of the molecule (and thus the location of the activated $^1O_2$).[8] Understanding the relationship between the photosensitizer and fluence level on initiating one pathway or the other is the objective of dosimetry, for which preliminary work will be started in this chapter.

## 6.2 Low Dose PDT for Indirect Immuno-Initiation of Cell Death

It has been demonstrated that the direct pathway towards cell lethality is dominant when $^1O_2$ is generated under 'high dose' conditions – light fluence or photosensitizer dosage is elevated and oxygen concentrations within a tumor are non-limiting. However, high dose PDT is also shown to cause vascular occlusions of tumors with a subsequent ischemia-induced cell death.[11] Such blood supply restriction is a non-ideal mode of cell death, as it precludes future treatment efficacy in the instance that an initial treatment course resulted in a deficient eradication of the disease; the blood vessels that serve as the photosensitizer delivery route have now been destroyed, impeding further localizations to the site.

Alternatively, when one or all of these components (light, photosensitizer or oxygen) is limiting (low dose PDT), apoptosis and/or necrosis is hardly detected, though an effective inflammatory response is often observed with ultimate cell death.[11] As this scheme is biologically more intricate, it is the more appealing methodology to evaluate for a potential PDT agent; if a notable therapeutic response can be spurred with low dose PDT, it would not be implausible to presume a viable extension to the high dose, more austere method of a direct cell death pathway.

Therefore, the work presented in this chapter centers around parameters of low dose PDT, in an effort to highlight the potential of these ICG-CPSNP agents to succeed in more temperate treatment schemes appropriate for early stage presentation.

Preliminary *in vitro* work will be employed to correlate a definite biological outcome with the SOSG responses developed in the preceding chapter. This association will provide the integration of the preliminary dose map presented in Chapter 5 with cell viability influences. Such combination will allow first round predictions of therapeutic performance. Finally, using this initial therapeutic model, a preliminary *in vivo* low dose PDT treatment of human breast adenocarcinoma is used to evaluate the theoretical function, with the intention of substantiating the potential of these composite ICG-CPSNPs for therapeutic application.

## 6.3 Materials and Methods

### 6.3.1 Materials

All chemicals used in this work were purchased as described: indocyanine green from TCI America (Portland, OR); Dulbecco's Modified Eagle's Medium, Roswell Park Memorial Institute RPMI-1640 Media, and McCoy's 5a Medium Modified from Sigma Aldrich (St Louis, MO); fetal bovine serum (35-010-CV, Regular) from Mediatech, Inc. (Manassas, VA); Antimycotic solution from Invitrogen (Carlsbad, CA); CellTiter 96® Aqueous Non Radioactive Cell Proliferation Assay Kit purchased from Promega (Madison, WI).

### 6.3.2 Cell Culture Work

Human MDA-MB-231 breast cancer cells were cultured in DMEM. Human BxPC-3 pancreatic cancer cells were cultured in RPMI-1640. Both human HT-29 colorectal adenocarcinoma and HCT116 colorectal carcinoma cells were cultured in McCoy's 5a Medium Modified. Each media was supplemented with 10% fetal bovine serum (FBS) and 1% antibiotic/antimycotic solution and maintained at 37°C and 5% $CO_2$. All cell culture experimentation was conducted in collaboration with and within the facilities of the Pennsylvania State University College of Medicine, Department of Pharmacology.

### 6.3.3 Cell Viability Assay

Cell viability was assessed using a colorimetric MTS assay, which measures the activity of enzymes that reduce the tetrazolium salt MTS ((3-(4,5-dimethylthiazol-2-yl)-5-(3-carboxymethoxyphenyl)-2-(4-sulfophenyl)-2H-tetrazolium)) in the presence of phenazine methosulfate (PMS) into a water-soluble formazan that has an absorbance maximum at 490 nm. This reduction takes place only when reductase enzymes are active, and therefore conversion is an indicator of viability; increased cell toxicity decreases performance in the assay.

Cells were cultured at a density of 5000 cells per well in flat bottomed 96-well plates and incubated with the particular sample for two hours. Samples were diluted from the same stock suspension into PBS, with dilution ratios ranging from 1:800 to 1:25 ($4.5 \times 10^{10}$ – $1.4 \times 10^{12}$ particles and 2.75 nM – 88 nM encapsulated ICG, respectively). After the arranged laser irradiation dosage (if applicable), the cells were incubated for 24 hours before the MTS reagents (CellTiter 96® Aqueous One ) were added to each well according to the manufacturer's instructions and incubated for an additional 4 hours. Cell viability was then determined by

measuring the absorbance at 490 nm using a UV-visible microplate reader relative to a PBS-dosed control well.

### 6.3.4 *In Vivo* Animal Studies

All animal procedures were approved by the Pennsylvania State University Institutional Animal Care and Use Committee. A breast adenocarcinoma model in athymic mice was prepared as previously described in Chapter 4. Briefly, $10^7$ MDA-MB-231 cells prepared in 100 μL of growth media were subcutaneous injected into the flank of the four to six week old female nude mice (Harlan, Indianapolis, IN), and allowed to establish for one week until the tumors measured approximately 5 mm in diameter. For this preliminary experiment, there was one animal per group, two subcutaneous tumors per animal, and four subject groups for a total of eight tumors.

Each animal was administered an analyte via a tail vein injection. The analyte for each group was either a dose of ICG-CPSNP-PEG, or an associated control to match the various characteristics of this sample: a 100 μL dose of PBS, a 44 nM solution of free ICG, or a dose of $3.6 \times 10^{10}$ particles of Ghost-CPSNP-PEG. After 24 hours, each subcutaneous tumor was irradiated with a 785 nm laser (12.5 J/cm$^2$), and set as day zero. The results of the PDT protocol were assessed by examining changes in tumor volumes over time. Each subcutaneous tumor was measures across three different axes with microcalipers. The volumes for each tumor were normalized to the volume of the same tumor on the first day after the laser irradiation (day 1) and repeated over the course of 36 days.

## 6.4 Results and Discussion

### 6.4.1 ICG-CPSNP Dark Toxicity

Before an accurate evaluation of the PDT effectiveness of the composite photosensitizer vectors can be addressed, any inherent acute toxicity of the CPSNPs exclusive of photodynamic effects is investigated. This is referred to as the dark toxicity of the photosensitizer and is frequently attributed to intracellular concentration effects. Figure 6-1 presents cell viability as a function of encapsulated ICG concentration in four distinct cell lines. Despite the anticipated variability among the lines associated with cell specific disparities (sturdiness, metabolic rates, intake kinetics, etc), there is an overall inverse relationship with viability and photosensitizer concentration. For the colorectal cancer lines, the median lethal dose ($LD_{50}$) is not reached until an encapsulated ICG concentration between 50 and 60 nM; neither the breast cancer or pancreatic cancer lines exhibited significant acute dark toxicity within the concentration ranges examined.

This $LD_{50}$ is significantly lower than the reported ICG concentrations employed in similar *in vitro* PDT work (10 – 50 μM).[5] Therefore, the effect on viability is attributed to the CPSNP particle number, as opposed to the concentration of the comprised encapsulate, which is three orders of magnitude below the safe range used in the literature. Based on the encapsulation yield discussed in Chapter 3, a 60 nM ICG content amounts to approximately $9.8 \times 10^{11}$ particles. To substantiate this assertion, Figure 6-2 presents the acute cytotoxicity of PEG-Ghost-CPSNP as a function of particle number. A CPSNP sample is termed a ghost sample when it carries no encapsulated molecules. The average $LD_{50}$ for the blank nanovectors in the same colorectal cancer lines is approximately $1 \times 10^{12}$ particles, corresponding to approximately $2 \times 10^{8}$ CPSNPs per cell. This particle concentration corresponds with the associated particle number data

presented in Figure 6-1, and as such, will define the limit of CPSNP dosing in the following experiments to be cautious of intracellular concentration influences.

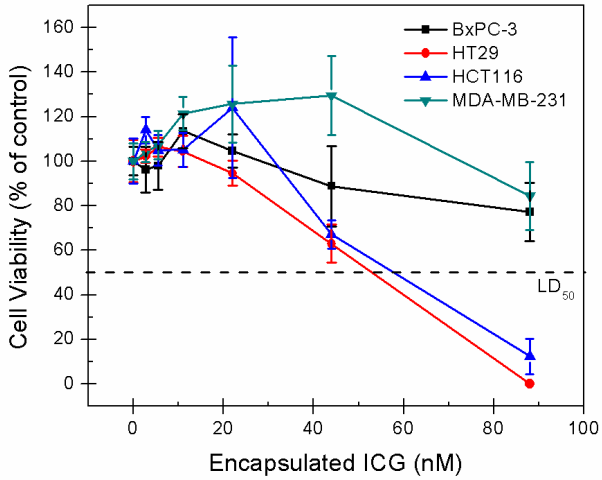


**Figure 6-1.** The dark toxicity of ICG-CPSNPs is determined by examining the cell viability in multiple cell lines as a function of encapsulated fluorophores. For the colorectal cancer lines HT29 and HTC116, the median lethal dose ($LD_{50}$) is not reached until an encapsulated ICG concentration between 50 and 60 nM. The MDA-MB-231 and BxPC-3 lines did not exhibited significant acute dark toxicity within the concentration ranges examined.

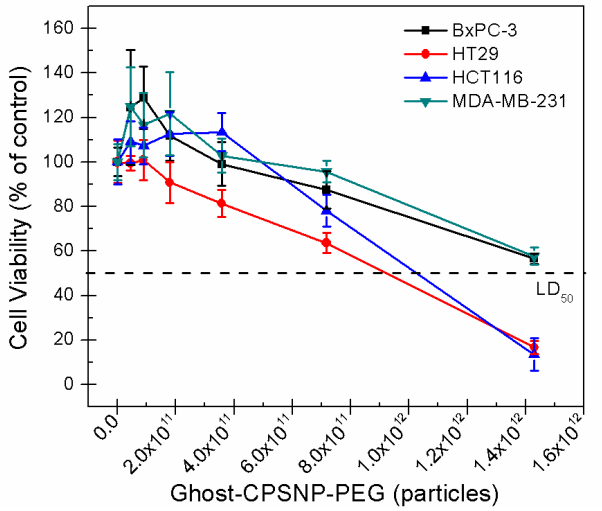


**Figure 6-2.** The acute toxicity of CPSNPs is determined by examining the cell viability in multiple cell lines as a function of Ghost-CPSNP-PEG particle concentration. For the colorectal cancer lines HT29 and HTC116, the median lethal dose ($LD_{50}$) is found to be 1 x $10^{12}$ particles. This amounts to approximately 2 x $10^{8}$ CPSNPs per cell. The MDA-MB-231 and BxPC-3 lines exhibited an approximate $LD_{50}$ towards the limit of the examined particle concentration range around 1.5 x $10^{12}$.

### 6.4.2 *In Vitro* PDT Performance of ICG-CPSNPs

This initial analysis of dark toxicity identifies the particulate photosensitizer concentration limit. Now attention is turned to the PDT effect. The assessment of ICG-CPSNPs as a potential photosensitizer in PDT was carried out in multiple cell lines in an attempt to recognize any commonality in ICG-CPSNP therapeutic performance independent of specific cell line variability. The cells were dosed with $2 \times 10^{11}$ to $7 \times 10^{11}$ ICG-CPSNP-PEG particles (11 - 44 nM of encapsulated photosensitizer), a dosage range that falls below the $LD_{50}$ for all the cell lines examined. Also, the energy density applied totaled 1 J/cm$^2$, an irradiation dosage well below the therapeutic threshold of the ICG encapsulated molecules, as described in Chapter 5. This combination (low photosensitizer concentration, low fluence) characterizes low dose PDT.

Comparison of the dark toxicities and the cell viability response to ICG-CPSNP-PEG mediated PDT for the four cell lines is presented in Figure 6-3. Save for the HT29, the colorectal adenocarcinoma cell line, cell viability was reduced toward 50% with the combination of 44 nM of encapsulated ICG in ICG-CPSNP-PEG and 1 J/cm$^2$ of 785 nm light. The cell specific response noted in Figure 6-3 is expected at such low PDT doses, which is intended to stimulate an immune response to indirectly initiate cell death - an element that is appreciably deficient in *in vitro* experimentation. As such, the low dose PDT response is subject to the intricate differences of heartiness and biological kinetics among each cell type. Nevertheless, though variable, these are promising results. This is the first report of photocytotoxic activity at such low PDT parameters ($10^3$x lower photosensitizer concentration, 12x lower fluence). The unmistakable drop in cell viability relative to the control at such a significantly low applied fluence suggests conceivably greater therapeutic efficiency at more customary laser powers.

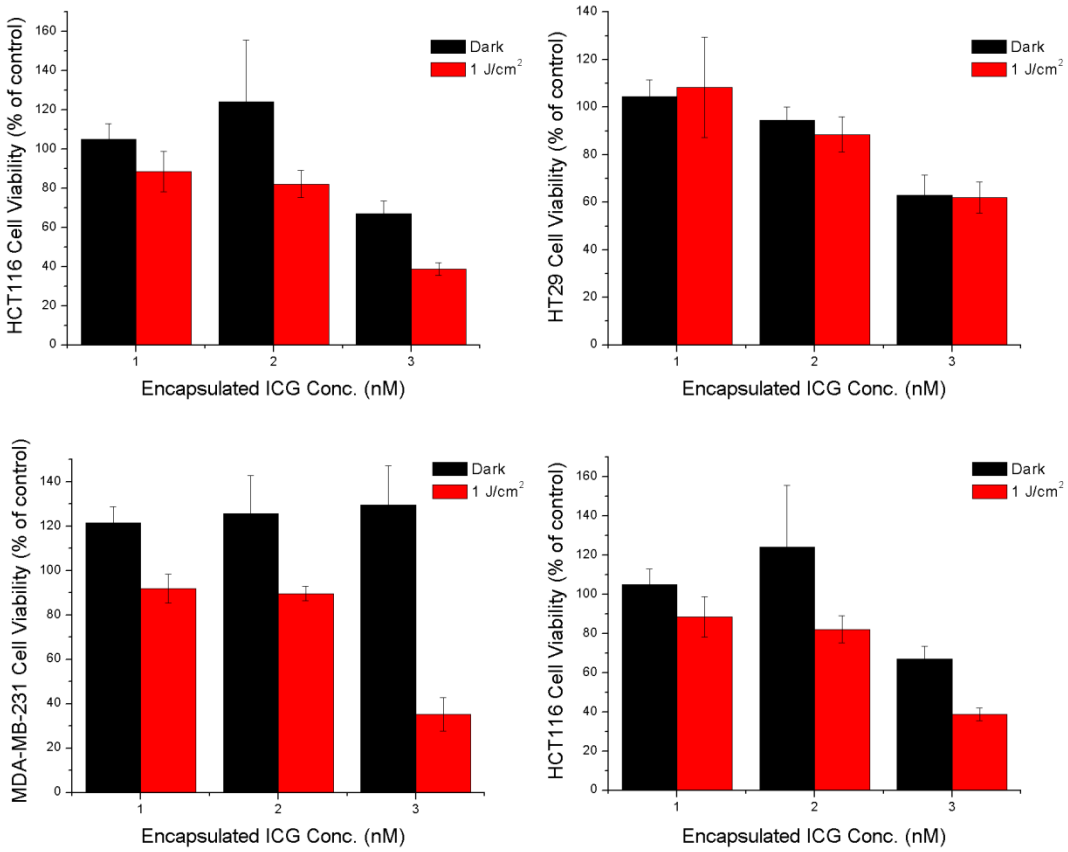


**Figure 6-3**. Cell viability in response to PDT from ICG-CPSNP-PEG relative to a control (dark) group are presented. The photosensitizer concentration ranged from 11 – 44 nM, three orders of magnitude lower than concentrations reported in the literature. The fluence rate was also significantly reduced (1 J/cm$^2$) compared to conventional irradiation energy densities. A marked decrease in cell viability is observed even under this low dose PDT regime for three of the four cell lines examined, suggesting remarkable therapeutic promise under clinical conditions.

An examination of this implication was conducted on the MDA-MB-231 cell line; cell viability for a set photosensitizer concentration (22 nM) was evaluated as a function of laser fluence rate. Figure 6-4 reveals that cell lethality did in fact increase (decreased viability) as the incident laser energy density increased. Though the fluence range was tight, the fluence-viability relationship was linear within the range examined.

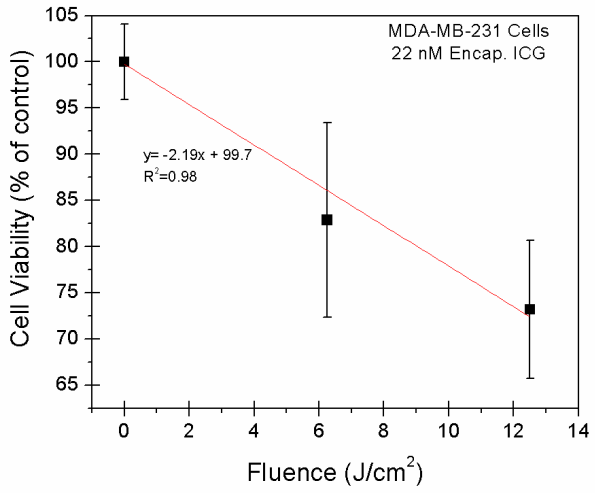


**Figure 6-4.** The cell viability of MDA-MB-231 human breast carcinoma cells is seen to decrease with an increase in laser fluence for a set photosensitizer concentration (22 nM). This behavior serves to highlight the remarkable potential of ICG-CPSNP mediated PDT in clinical settings, which presently exhibits notable photocytotoxicity under significantly low PDT parameters.

Returning to the preliminary dose map presented in Chapter 5, the cell viability data from above can be incorporated to convert probe response (SOSG intensity) to the therapeutic response (number of cells killed). Using the MDA-MB-231cell data, the map is modified and presented in Figure 6-5. This figure visually charts the *in vitro* cell death count of these human breast adenocarcinoma cells as a function of the combination of photosensitizer dosage and fluence rates. It must be acknowledged that the projected cell death values are based on the linear relationship identified above (Figure 6-4). However, there is yet no indication of the PDT-viability relationship beyond the limits explored. Therefore, the preliminary PDT dosing map in Figure 6-5 is presented to merely illustrate the potential link between *in vitro* parameters and theoretical dosing models. At this point, application to *in vivo* performance is restricted and should be attempted with reservation, understanding that the model is based on *in vitro* conditions, and that the projected fluence effects (indicated by the dashed contours) are generated from an unsubstantiated assumption of fluence-cell death linearity.

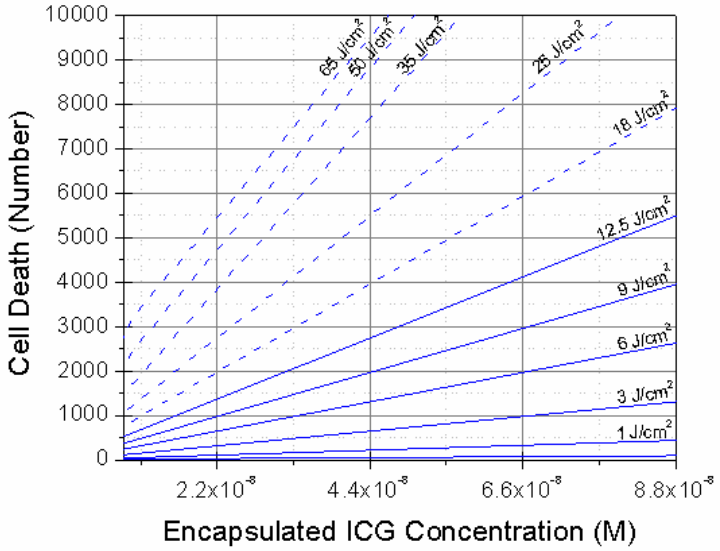


**Figure 6-5.** A first-generation dosing map charts the *in vitro* cell death count of MDA-MB-231 human breast adenocarcinoma cells as a function of the combination of ICG-CPSNP photosensitizer dosage and 785 nm fluence rate.

### 6.4.3 *In Vivo* PDT Improvements from ICG-CPSNPs

To validate the potential for therapeutic application proposed by the *in vitro* experimentation above, the *in vivo* PDT efficacy of ICG-CPSNP-PEG in human breast adenocarcinoma xenografts was assessed by charting tumor growth after administration of therapy. Each subject group was administered a single dose of sample via a tail vein injection; the groups comprised of ICG-CPSNP-PEG, a matching free ICG concentration of 44 nM, a matching particle number of $3.6 \times 10^{10}$ Ghost-CPSNP-PEG, and a negative control of 100 μL PBS. After a 24 hour period, providing time for the passive localization in the tumors as identified in Chapter 4, each tumor was irradiated with a single dose of 785 nm light (12.5 J/cm$^2$). Tumor volumes were then measured at each time interval (roughly every 4 days) and normalized to the initial state (one day post light irradiation – day 1). Figure 6-6 plots the relative tumor volume as a

function of time for the various trial groups. It is clear that the ICG-CPSNP-PEGs arrest tumor growth over 36 days, while all other controls grew up to 10-fold the initial size.

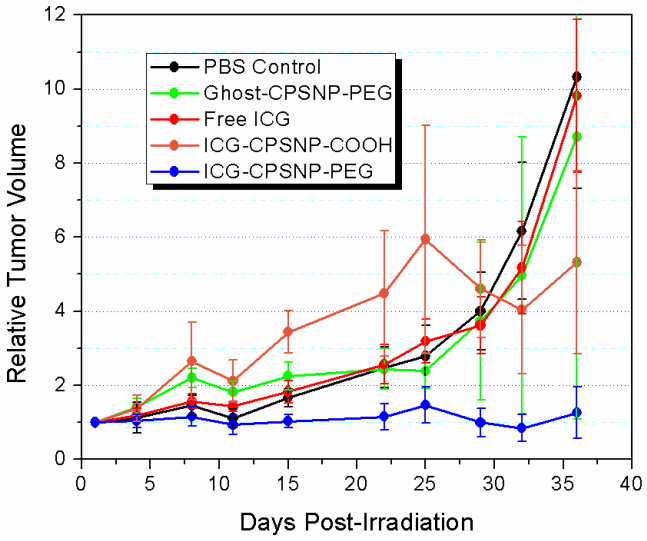


**Figure 6-6.** A relative tumor volume as a function of time post therapy plot for an *in vivo* PDT trial on MDA-MB-231 human breast cancer xenografts in nude mice. Each animal received a single systemic injection of sample or control and one irradiation dose (12.5 J/cm$^2$) per tumor. The ICG-CPSNP-PEG clearly arrest tumor growth over the 36 day period, while all other control groups grew to 10-fold their initial size.

This preliminary study highlights the tremendous potential of the ICG-CPSNPs for low dose PDT, even under non-optimal conditions. Additional improvements are anticipated upon optimizing the overall PDT dose for a given disease presentation, such as initial tumor volume and depth within tissue. For example, directly targeting the diseased tissue would improve the localized photosensitizer concentration. Additionally, composing the dosimetry map to encompass a larger spectrum of fluence-viability effects and larger scale cell deaths would allow dependable dosing predictions to design to ultimate *in vivo* therapeutic performance. In any case, this is the first successful report of ICG-based PDT *in vivo*, and serves as persuasive evidence of the therapeutic capacity of these composite ICG-CPSNP platforms.

## 6.5 Summary

This chapter built on the demonstrated improvements in photoactivation of reactive $^1O_2$ (Chapter 5) by extending the analysis to the *in vitro* and *in vivo* capacity of ICG-CPSNPs as a photosensitizer agent in a PDT modality. Initial toxicity trials were conducted *in vitro* across four distinct cell lines to identify an ICG-CPSNP-PEG dosing limit. It was revealed that acute toxicity is subject to the particle number concentration ($LD_{50}$ of 2 $x10^8$ CPSNP/cell) and not the dose of encapsulated ICG. Next, cell viability was examined as a function of PDT dose. The PDT dosage was controlled by the various combinations of encapsulated ICG concentration and laser fluence rate, both of which were restricted to decreased levels to relate to a low dose PDT scheme. An unmistakable drop in *in vitro* cell viability relative to the control was observed for all cell lines. The significance of these results rests in the drastically low applied fluence, which suggests a plausibly greater efficacy in cell lethality at more customary laser powers.

Finally, the potential for therapeutic application was evaluated by the *in vivo* PDT effect of ICG-CPSNP-PEG on tumor growth. These composite photosensitizers were shown to arrest tumor growth over 36 days after only a single, low dose systemic administration and laser activation. Such heightened photodynamic cell lethality with ICG-CPSNPs emphasizes the tremendous potential this composite nanovector has for low dose PDT applications, particularly considering the non-optimized nature of the preliminary experimentation. Therefore, coupled with the improved bioimaging capabilities, the efficient *in vivo* performance of ICG-CPSNPs serves as the irrefutable validation of the apposite bifunctionality of these vectors for successful theranostic employment.

## 6.6 Acknowledgements

Once again, the principal contributions of the Dr Mark Kester research group of the Penn State Hershey College of Medicine's Department of Pharmacology must be acknowledged. In particular, the invaluable efforts of Dr Brian Barth are recognized for his collaboration in designing and implementing both the *in vitro* and *in vivo* PDT experimentation. Also, the patience and persistence of Sriram Shanmugavelandy in dosing and irradiating each animal and tumor involved in the *in vivo* study is greatly appreciated.

## 6.7 References

1. Bäumler, W.; Abels, C.; Karrer, S.; Weiß, T.; Messmann, H.; Landthaler, M.; Szeimies, R.-M. Photo-Oxidative Killing of Human Colonic Cancer Cells Using Indocyanine Green and Infrared Light. *British Journal of Cancer* **1999,** *80*, 360-363.
2. Gratz, H.; Penzkofer, A.; Abels, C.; Szeimies, R.-M.; Landthaler, M.; Bäumler, W. Photo-Isomerisation, Triplet Formation, and Photo-Degradation Dynamics of Indocyanine Green Solutions. *Journal of Photochemistry and Photobiology A: Chemistry* **1999,** *128*, 101-109.
3. Reindl, S.; Penzkofer, A.; Gong, S.-H.; Landthaler, M.; Szeimies, R.-M.; Abels, C.; Bäumler, W. Quantum Yield of Triplet Formation for Indocyanine Green. *Journal of Photochemistry and Photobiology A: Chemistry* **1997,** *105*, 65-68.
4. Crescenzi, E.; Varriale, L.; Iovino, M.; Chiaviello, A.; Veneziani, B. M.; Palumbo, G. Photodynamic Therapy with Indocyaine Green Complements and Enhances Low-Dose Cisplatin Cytotoxicity in Mcf-7 Breast Cancer Cells. *Molecular Cancer Therapeutics* **2004**, 537-544.
5. Fickweiler, S.; Szeimies, R.-M.; Bäumler, W.; Steinbach, P.; Karrer, S.; Goetz, A. E.; Abels, C.; Hofstädter, F.; Landthaler, M. Indocyanine Green: Intracellular Uptake and Phototherapeutic Effects in Vitro. *Journal of Photochemistry and Photobiology B: Biology* **1997,** *38*, 178-183.
6. Urbanska, K.; Romanowska-Dixon, B.; Matuszak, Z.; Oszajca, J.; Nowak-Sliwinska, P.; Stochel, G. Indocyanine Green as a Prospective Sensitizer for Photodynamic Therpay of Melanomas. *Acta Biochimica Polonica* **2002,** *49*, (2), 387-391.
7. Wilson, B. C.; Patterson, M. S. The Physics, Biophysics and Technology of Photodynamic Therapy. *Physics in Medicine and Biology* **2008,** *53*, R61-R109.
8. Oleinick, N. L.; Morris, R. L.; Belichenko, T. The Rolse of Apoptosis in Response to Photodynamic Therapy: What, Where, Why and How. *Photochemical & Photobiological Sciences* **2002,** *1*, 1-21.
9. Cecic, I.; Korbelik, M. Mediators of Peripheral Blood Neutrophilia Induced by Photodynamic Therapy of Solid Tumors. *Cancer Letters* **2002,** *183*, 43-51.

10. Granville, D. J.; McManus, B. M.; Hunt, D. W. C. Photodynamic Therapy: Shedding Light on the Biochemical Pathways Regulating Porphyrin-Mediated Cell Death. *Histology and Histopathology* **2001,** *16*, 309-317.
11. Piette, J.; Volanti, C.; Vantieghem, A.; Matroule, J.-Y.; Habraken, Y.; Agostinis, P. Cell Death and Growth Arrest in Response to Photodynamic Therapy with Membrane-Bound Photosensitizers. *Biochemical Pharmacology* **2003,** *66*, 1651-1659.

# Chapter 7

# Summary and Suggestions for Future Work

A calcium phosphate-based nanoparticulate vector was developed to serve as a model theranostic agent for the simultaneous diagnosis and treatment of early stage disease. For successful bifunctional performance, the theranostic agent must effectively perform as both a sensitive imaging agent for deep tissue detection, and execute a highly effective yet moderate therapeutic response adequate to manage the early state of disease. The work presented has confirmed the utility of ICG-CPSNPs in both of these performance criteria, emphasizing the potential capacity of this nanocomposite particle for theranostics.

## 7.1 Summary of Work

The established biocompatibility of calcium phosphate was exploited in the design of the platform for the theranostic agent. A template synthesis in the self-assembled reverse microemulsion of a water-in-oil cyclohexane/ polyoxyethylene(5) nonylphenyl ether/water ternary system was used to precipitate calcium phosphosilicate nanoparticles (CPSNPs). These nanoparticles were designed to encapsulate the NIR active fluorophore indocyanine green (ICG), which was added to the micelles prior to precipitation. ICG is reported to induce phototoxicity in addition to fluorescent emission, and thus serves as the functional element of the proposed imaging and therapeutic modality. Functionalization of the CPSNPs was achieved with the reaction of sodium citrate, yielding a carboxylate-terminated surface. The sample suspension was then laundered via a van der Waals-HPLC (vdW-HPLC) protocol that utilizes surface charging to

separate and concentrate the CPSNPs from the synthesis precursors and unencapsulated fluorophore molecules.

### 7.1.1 Colloidal Properties

Imaging with TEM revealed the well dispersed state of particles, the spherical morphology, and the log normal mean particle diameter of 16 nm. EELS mapping identified a Ca:P:Si ratio of 1:1.72:0.41 and a homogenous composition without evidence of an element rich or deficient region. Zeta potential of the as-synthesized, citrate-functionalized CPSNPs is -29 ±3 mV. A theoretical solids loading of $1.9 \times 10^{13}$ CPSNP/mL was calculated for a standard suspension. The mean ICG content per suspension is $2 \times 10^{-6}$ M, which equates to approximately 63 fluorophore molecules encapsulated per CPSNP.

### 7.1.2 Optical Properties

The optical properties of these ICG-CPSNPs were demonstrated to be well suited for early stage *in vivo* tumor imaging in that encapsulation provided an enhanced and stable optical signal compared to the free fluorophore. This improvement was realized through the elimination of specific non-radiative relaxation pathways pestilent to ICG in solution (fluorescence quenching, photoisomerization, and photodegradation) that detrimentally shorten the excited state lifetime and, consequently, reduce the fluorescence quantum yield.

The rigid installation of the embedded molecules within the particles inhibited structural translations, thereby eliminating the translational non-radiative relaxation pathway of photoisomerization. By removing this competing decay route, the internalized molecules afforded a higher contribution to fluorescence, accounting partly for the significantly brighter emission

intensity compared to a matching concentration of the free fluorophore. Additionally, fixing the internal molecules with the CPSNPs mitigated intermolecular associations that typically inflict aggregation. This resulted in a lower contribution of self-quenching effects, allowing a greater concentration of the fluorophore to be used when encapsulated to generate higher emissive signals.

The physical boundary encasing the ICG molecules was also demonstrated to serve as a shield from the surrounding solvent environment, protecting against dynamic collisional interactions that deactivate the excited state at the expense of radiative emission; the fluorescent CPSNPs were solvent resilient, imparting a consistent optical performance irrespective of solvent influences and environmental effects. Furthermore, this matrix protection yielded heightened fluorescence lifetimes, afforded by the deferred onset of degradation mechanisms of the internalized molecules. Specifically, the dye-doped CPSNPs exhibited a 4.7-fold longer fluorescent half-life at clinical imaging excitation power ranges.

The inclusive effect of these individual alterations was established by the comprehensive fluorescence performance in the recognized ICG- depressing environment of PBS. Specifically, the ICG-CPNPs demonstrated a 2-fold increase in quantum efficiency ($0.053 \pm 0.003$) in physiological solution, a favorable outcome for the sensitive diagnostic imaging aspect of a theranostic modality.

### 7.1.3 *In vivo* Imaging Performance

The *in vivo* emission signal stability from ICG-CPSNPs was compared to the free fluorophore by whole animal NIR imaging. The duration of fluorescent signal from the ICG-CPSPNPs was clearly extended, as emission was still resolvable up to four days post-injection while the fluorescence signal from the unencapsulated dye was lost within 12 hours. This result

highlights the potential for long-term imaging and sensitive tracking applications using ICG when encapsulated within the protective matrix of CPSNPs.

The hepatobiliary clearance of ICG was visually confirmed by a marked signal intensity localized to the gastrointestinal region of the animals immediately after administration, as well as the dissection of associated organs of the biliary clearance route. However, examination of the corresponding images for animals dosed with ICG-CPSNPs revealed a reduced single from this same region, implying that only a minor concentration of fluorophore was sequestered into this clearance pathway, amounting in a greater portion of the administered agent lingering in circulation. Such evasion of untimely clearance provides a prolonged functionality, and in turn, can enable higher precision diagnostics; increased localized agent concentrations yield brighter fluorescence, resulting in stronger signal intensities from even smaller regions of interest.

Once improved physiological function was established, attention was turned to targeting the emission signal to specific sites of interest in accordance with the proposed diagnostic element of the imaging protocol. The surfaces of the ICG-CPSNPs were covalently bound with polyethylene glycol (PEG), as verified by a masked surface charge and a net neutral zeta potential distribution shift. Comparing the pharmacokinetic behavior of the PEGylated ICG-CPSNPs to the original negatively charged carboxylate-terminated CPSNPs revealed that ICG-CPSNP-PEG passively localize within solid tumor xenografts within 24 hours of systemic administration. This passive localization is the consequence of an enhanced permeation and retention (EPR) effect related to the prolonger circulation lifetimes afforded by the PEG-coated particles.

To impart tissue specificity, the ICG-CPSNP-PEGs were bioconjugated with gastrin-10 with the intention of targeting BxPC-3 cells by specifically binding the over expressed receptors for this hormone. An initial *in vitro* assessment acknowledged the faculty of this functionalization to preferentially target the cells of interest; fluorescence microscopy visually revealed this targeting capacity, while flow cell cytometry explicitly characterized the preferential cellular

uptake of the ICG-CPSNP-PEG-Gastrin-10 by BxPC-3 cancer cells. A NIR whole animal imaging study further verified that gastrin functionalization provides a direct means for targeting orthotopic pancreatic tumors *in vivo*, with emission signal intensities from excised tumors measuring higher relative to the controls. This result highlights the ability of targeted ICG-CPSNPs to provide the high *in vivo* selectivity needed for the most effective diagnostics imaging.

### 7.1.4 Therapeutic Capacity

The performance of ICG-CPSNPs as potential photosensitizers in a photodynamic therapeutic modality was evaluated. The *ex situ* examination of photoactivation of singlet oxygen in a hypoxic aqueous environment was found to be 60% higher from the ICG molecules upon encapsulation within the CPSNP matrix. Such an increase underlines the potential improvement in photosensitization capacity of this third generation photosensitizer, suggesting a greater efficiency in photodynamic therapies.

The therapeutic capacity of ICG-CPSNP composites was determined by observing the SOSG intensity of a single encapsulated ICG molecule as a function of the irradiation energy. This behavior was found to be non-linear, corresponding to the finite rate of intersystem crossing. This relationship was then employed to model the expected SOSG intensity as a function of encapsulated ICG concentration-laser irradiation combinations. Such a relationship sets up the possibility to associate the photosensitizer and laser dosing to a targeted therapeutic response in a dosimetry map.

Initial *in vitro* toxicity trials were conducted in four distinct cell lines to identify an ICG-CPSNP-PEG dosing limit. It was revealed that acute toxicity is subject to the particle number concentration ($LD_{50}$ of 2 $x10^{8}$ CPSNP/cell) and not the dose of encapsulated ICG. Next, cell viability was examined as a function of PDT dose. The PDT dosage was controlled by the various

combinations of encapsulated ICG concentration and laser fluence rate, both of which were restricted to decreased levels to relate to a clinical low dose PDT scheme. An unmistakable drop in cell viability *in vitro* relative to the control was observed for all cell lines. The significance of these results rests in the drastically low applied fluence (1 J/cm$^2$), which suggests a plausibly greater efficacy in cell lethality at more customary laser powers.

Finally, the potential for therapeutic application was evaluated by the *in vivo* PDT effect of ICG-CPSNP-PEG on tumor growth. These composite photosensitizers arrested tumor growth over 36 days after only a single, low dose systemic administration (44 nM) and laser activation (12.5 J/cm$^2$). Such heightened photodynamic cell lethality with ICG-CPSNPs emphasizes the tremendous potential this composite nanovector has for low dose PDT applications, particularly considering the non-optimized nature of the preliminary experimentation.

Together with the demonstrated improvements in bioimaging performance, the efficient *in vivo* therapeutic execution of ICG-CPSNPs serves as confirmation of the apposite bifunctionality of these vectors. Coupled with the established biocompatibility and favorable pharmacokinetics of calcium phosphates, these composite nanoparticles possess the potential to serve as a model theranostic agent in the early stage diagnosis and treatment of disease.

## 7.2 Suggested Future Work

The primary objective of the current work was to establish the promise of ICG-CPSNPs for effective employment in a simultaneous imaging and therapy modalities. Attention can now be turned to optimizing this combined performance.

### 7.2.1 Colloidal Properties

The inclusion of silicate into the calcium phosphate matrix was intended to aid in the stability of the particles at physiological pH by reducing the material solubility. However, the operative effect on the solubility product ($k_{sp}$), dissolution kinetics, and long-term phase stability has yet to be evaluated. Discerning the impact on the solubility product, as well as the rate of dissolution in physiological and intracellular environments, as a function of silicate content, will aid in pinpointing the optimal material composition for the most effective colloidal stability-physiological performance relationship. Also, such understanding provides the means to tailor the material composition for application specific requirements, such as sustained release for drug delivery schemes, or complete insolubility for tracking purposes.

The solubility product and rate of dissolution as a function of silicate content can be identified through a series of titration experiments employing a $Ca^{2+}$ specific ion probe. By maintaining the solution pH and phosphate content in an undersaturated calcium and phosphate solution (with the use of a phosphate buffer), the free $Ca^{2+}$ from CPSNP dissolution can be recorded and quantified. The plateau would indicate the point of solution equilibrium, from which a $k_{sp}$ value can be back-calculated, while the slope of the $Ca^{2+}$-probe response curve indicates the rate of dissolution, from which dissolution kinetics can be mined. Long-term phase stability as a function of silicate content can be assessed through X-ray diffraction of bulk samples over a period of time post-synthesis. Preclusion of crystallinity would indicate effective amorphous phase stability.

Likewise, appraising the influence on both optical performance and singlet oxygen sensitization as a function of the fluorophore loading is critical in designing a CPSNP of optimal performance. To date, all evaluations were conducted on constant fluorophore content. A series of ICG-CPSNPs of varying dye content can be prepared by either systematically decreasing the

initial ICG concentration in microemulsion B during synthesis by one to up to four orders of magnitude (to reduce the final fluorophore loading), or by altering synthesis parameters such as increasing the micelle water to surfactant molar ratio (thus increasing the template size and forming larger particles for higher potential dye sequestering). Furthermore, to effectively evaluate the concentration influence, the true number of dye molecules per CPSNP must be determined. The present assumption based on the theoretical particle number was initially sufficient, but future evaluation on the concentration effect is ineffectual without knowledge of the actual values. Fluorescent correlation spectroscopy (FCS) set up in the NIR wavelengths of interest (Ex 785 nm, Em > 820 nm), would directly quantify both the number of composite fluorescing units (CPSNPs), and identify the number of fluorophore molecules associated with each NP.

Correspondingly, the physical determination of the particle number concentration in a given suspension is the core element in elucidating concentration specific influences on performance. The theoretical calculation presented assumes two general assumptions: 100% yield and total recovery during laundering. FCS can be used to quantify the number of fluorescing CPSNPs, which is all that is needed for *ex situ* optical or oxygen sensitizing performance assessment. However, for *in vitro* and *in vivo* particle concentration influences on viability and toxicity, for which all particles, even the non-fluorescent, play a role, scattering based particle number characterization techniques such as Nanoparticle Tracking Analysis (NTA) should be used. The integrated software in such characterization techniques converts the detected scattered light into a particle number concentration. However, in the very least, a qualitative assessment of wash recovery would better approximate the range of particle numbers used in the various characterizations and experiments. This could be accomplished by comparing the total mass post-synthesis (pre-laundering) to the mass recovered after a washing cycle. Using thermal gravimetric analysis (TGA), samples can be heated to 1000$^{o}$C and weight loss charted to follow the

evaporation of solvent and burn out of surfactant and organics. The final mass at 1000$^{o}$C would correspond to the remaining inorganic, a sintered mass of CPSNPs. The difference in this final mass between the post-synthesized samples and those run through the vdw-HPLC protocol would reveal the washing yield. Applying this mass lost during the laundering process to the theoretical calculations will provide a better approximation of particle concentrations used in various experiments.

### 7.2.2 *In vivo* Therapeutic Performance

The optimistic results demonstrated in the preliminary PDT experimentation emphasize the extraordinary promise of these nanocomposities for therapeutic application. The logical next step would be to optimize the performance to yield the most efficient therapy - highest localized cell death in the shortest amount of time; this requires the optimization of both photosensitizer concentration and applied laser fluence, which can be identified through a series of PDT studies.

The photosensitizer concentration optimization is two sided. Concentration can be increased by both escalating the localization of ICG-CPSNPs at the targeted site, and by raising the photosensitizer loading per CPSNP. Knowledge of the optimal ICG loading, alluded to above in terms of the CPSNP photosensitizer capacity, will in turn define the optimal particle number concentration to accumulate at the target tissue. The latter can be manipulated by improving direct targeting schemes to localize the highest fraction of dosed agent in the shortest amount of time. For example, present work employed the hormone decagastrin to target gastrin receptors overexpressed by pancreatic cancer lesions. However, it was revealed through *in vivo* imaging that gastrin receptors on additional tissues, such as the brain, resulted in considerable unsolicited accumulations. Selection of a more specific hormone or bioconjugate exclusive to the target disease may aid in increasing accumulation levels by eliminating such competing localizations.

Also, understanding the dissolution kinetics, as described above, would set a time frame for the initiation of the laser dosing once particle accumulation commences, to ensure the photosensitizer is still internalized before the CPSNPs begin to dissolve and the afforded enhancement in triplet state formation and singlet oxygen generation is lost.

### 7.2.3 Scale Up

Finally, all of these suggested optimizations and future work would be less arduous if the amount of available CPSNP to work with were higher. To date, the synthesis yields are too low for feasible use in many characterization techniques. Furthermore, at this point, a new sample must be synthesized and laundered for each experiment. Increasing yields by scaling up the process would significantly expedite optimization of these materials by shifting efforts away from constant syntheses, to efforts for development. Yields of synthesized material can be increased by both using precursor solutions of higher concentration (towards the solubility limits), as well as increasing the overall volumes of solutions used (a one liter microemulsion is roughly 300 times the present synthesis volume).

However, the restrictive element that currently inhibits efficient scale up is the laundering process. Therefore, before large scale quantities of material can be synthesized, a modified laundering system must be assembled. Such a system would still employ the functional elements of the presented vdW-HPLC, but eliminate the superfluous limitations imposed by conventional HPLC systems, such as flow volumes, pump rates, and pressures. By upgrading to independent, higher powered pumps, larger diameter tubing (0.375 inch inner diameter compared to the current 0.016 inches), and larger capacity packed columns (from 6 mL to 14 mL), the same surface charge-mediated washing can be applied at volumes orders of magnitude larger than presently used.

# VITA

## Erhan İbrahim Altınoğlu

Erhan İ. Altınoğlu was born in Ankara, Turkey on November 23, 1981. He emigrated with his family to Sydney, Australia by way of Melbourne the following year at the age of 6 months. After 13 years, the family once again relocated to Phoenix, Arizona in the summer of 1996. After graduating high school from Desert Mountain High in 2000, he attended Northwestern University in Evanston, Illinois, where he obtained a B.S. degree in Materials Science and Engineering in 2004. He entered the Pennsylvania State University in August of 2004, where he began his PhD studies in the Department of Materials Science and Engineering.